Università degli Studi di Padova

DIPARTIMENTO DI INGEGNERIA INDUSTRIALE DII
Corso di Laurea Magistrale in Ingegneria dell'Energia Elettrica

Tesi di laurea

AC DISCHARGE CHARACTERISTICS OF ENVIRONMENTALLY-FRIENDLY INSULATION GASES

Relatori:
Prof. A. Haddad
School of Engineering, Cardiff University
Prof. R. Turri
Dipartimento di Ingegneria Industriale

Candidato:
Andrea Tognon
Matricola 1147570

Anno Accademico 2018-2019

In memory of the great professor Enzo Giovanni Fontana,
who made me discover the love for electrical engineering.

May he rest in peace.

Abstract

This thesis proposes an investigation of trifluoroiodomethane (CF_3I) gas mixture as an alternative insulation medium to sulphur hexafluoride (SF_6) in GIL applications. In particular, the project is focused to prove the insulation performance of CF_3I with a reduced scale GIL under high alternating voltage. Since the new gas presents eco-friendly characteristics, understand its feasibility in gas insulated systems has a large importance because it could reduce the environmental impact due to the wide use of SF_6. The summary of the research work done so far in order to characterize the physical, the chemical and the electrical properties of CF3I and its mixture is presented in a literature review.

The model of the reduced scale GIL was simulated with a finite element method (FEM) solver (COMSOL Multiphysics 5.3a) to determine the electric field distribution along the geometry. In addition, tests have been carried out to validate the model and the results given by it. Finally, a comparison between theoretical formula, tests and simulation results show the reliability of the model.

The reduced scale coaxial prototype was placed inside a cylindrical pressure vessel to perform high-voltage experiments with CF_3I/CO_2 (30%/70%) mixture at 0,1 MPa (abs). The breakdown voltage and partial discharge inception voltage of the coaxial geometry have been investigated under high alternating voltage to prove the feasibility of a future GIL insulated with CF_3I/CO_2 mixture. Furthermore, metal protrusions were built in order to represent common defects in gas insulated systems and thus, to understand how the new gas mixture performs with the presence of disturbances of different dimensions.

Finally, the results of breakdown voltage test show a higher insulation capability of the mixture than that of air. In particular, since no breakdown occurred with CF_3I/CO_2 mixture up to the voltage limits of the test setup, it is important to note that even with the big disturbance the mixture has shown an insulation capability greater than two times than that of air.

In conclusion, partial discharge inception voltage tests have been performed with CF_3I/CO_2 mixture under different conditions. The results show that most likely there is a problem due to an external PD source in the test setup and for this reason, further investigations have to be carried out.

Acknowledgements

I would first like to thank my supervisor Professor Roberto Turri of the University of Padua. He made possible this unforgettable experience and was always available whenever I had doubts.

My sincere thanks to the supervisor Professor Abderrahmane Haddad of Cardiff University, who gave me the opportunity to work on a very important and stimulating topic. He steered me in the right direction during my research work with his invaluable knowledge.

I am profoundly grateful to all the members of the Advanced High Voltage Engineering Research Centre, in particular to Michail Michelarakis, Houssem Nechmi, Meirion Hills and Jonathan Colin James for all the precious discussions, their extensive knowledge and friendship.

Finally, I would like to thank my family and my girlfriend. I would have never achieved this master degree without their aid and constant support.

Contents

Abstract **i**

Acknowledgement **iii**

Contents **v**

List of Figures **ix**

List of Tables **xv**

List of Abbreviations **xviii**

1 Introduction **1**

1.1 Gas Insulated Lines (GIL) introduction 1

1.2 GIL technology 2

1.3 Benefits 7

2 CF_3I as an SF_6 alternative insulating gas **11**

2.1 Introduction 11

2.2 Sulphur hexafluoride (SF_6) review 12

2.2.1 Properties 12

2.2.2 SF_6 climate impact 14

2.2.3 SF_6 mixture 18

2.3 Trifluoroiodomethane (CF_3I) review 19

2.3.1 Physical and chemical properties 19

2.3.2 CF_3I and SF_6 climate impact comparison 21

2.3.3 By-products 22

2.4 CF_3I mixture review 26

2.5 CF_3I electrical properties 31

2.5.1 Electron interaction properties 31
2.5.2 Breakdown voltage 33
2.5.3 Partial discharge inception voltage 35

3 Test equipment and geometries used 37
3.1 Introduction 37
3.2 Test equipment 37
3.2.1 Pressure vessel 37
3.2.2 Bushing 39
3.2.3 Transformer 39
3.2.4 Divider 40
3.2.5 Gas extractor unit 42
3.3 Coaxial geometry 43
3.3.1 Inner conductor choice 43
3.3.2 Geometry dimensions 46
3.4 Plane-plane geometry 48
3.4.1 Dimensions 48

4 Electrostatic model 49
4.1 Introduction 49
4.2 Coaxial geometry model 50
4.2.1 Geometry 50
4.2.2 Materials 52
4.2.3 Boundary conditions 52
4.2.4 Mesh 53
4.2.5 Electrostatic analysis results 57

5 Capacitance evaluation 63
5.1 Introduction 63
5.2 Theoretical evaluation 64
5.3 COMSOL evaluation 65
5.4 Experimental evaluation 66
5.4.1 Test setup 66
5.4.2 Test results 68
5.5 Conclusion 70

6 Breakdown tests **71**
6.1 Introduction . . . 71
6.2 Test setup . . . 72
6.3 Metal protrusions . . . 73
6.4 Test procedure . . . 74
6.5 Atmospheric corrections . . . 75
6.5.1 Air density correction factor k_1 . . . 76
6.5.2 Humidity correction factor k_2 . . . 76
6.5.3 Exponents m and w . . . 77
6.6 Results . . . 78

7 PDIV tests **81**
7.1 Introduction . . . 81
7.2 Preliminary tests . . . 83
7.2.1 Test setup . . . 83
7.2.2 Test procedure . . . 85
7.2.3 Results . . . 86
7.3 Definitive PDIV test . . . 89
7.3.1 Test setup . . . 91
7.3.2 Test procedure . . . 93
7.3.3 Results . . . 94
7.4 Plane-plane test . . . 108
7.4.1 Test setup . . . 109
7.4.2 Results . . . 110

8 Conclusions **111**
8.1 Breakdown voltage tests conclusions . . . 111
8.1.1 BV future works . . . 112
8.2 PDIV tests conclusions . . . 113
8.2.1 Future works . . . 115

Bibliography **117**

List of Figures

1.1 GIL main components [3]. 2
1.2 GIL and OHL comparison [3]. 3
1.3 Tipical istallations techniques of GIL [3]. 4
1.4 Ground level magnetic flux comparison between OHL, cable and GIL (last two 2 m deep) [33]. 8
1.5 Power losses comparison between OHL, cable and GIL [36]. . 9

2.1 CF_3I molecular structure [14]. 19
2.2 Boiling temperature vs absolute saturation vapour pressure with CF_3I and SF_6 [40]. 20
2.3 Gaseous by-products as a function of cumulative charge q_c at 18 kV_{rms} (80% of V_b) [21]. 22
2.4 Fluorine density comparison between pure SF_6, CF_3I and CF_3I-CO_2 30/70% [27, 9]. 23
2.5 Iodine density comparison between pure CF_3I and CF_3I-CO_2 (30/70%) [27, 9]. 24
2.6 Iodine and fluoride density using adsorbent (C_2X) with CF_3I [25]. 25
2.7 Boiling temperature at different saturation vapour pressure with CF_3I, CF_3I-mixtures and SF_6 [10]. 27
2.8 AC Breakdown voltage of CF_3I and SF_6 mixed with N_2 and CO_2 under quasi-uniform electric field [45]. 28
2.9 AC Breakdown voltage of CF_3I and SF_6 mixed with N_2 and CO_2 under non-uniform electric field [45]. 28
2.10 SLF interruption capability with CF_3I/CO_2 and CF_3I/N_2 mixtures [26]. 30

2.11 BTF interruption capability with CF_3I/CO_2 and CF_3I/N_2 mixtures [26]. 30
2.12 Electron drift velocity in CF_3I as a function of E/N [43], ■ [12], × [18], ▲ [28], ○ [43]. 32
2.13 Electron drift velocity in SF_6 and CF_3I/CO_2 as a function of E/N at different CF_3I gas mixture ratio k [43]. 32
2.14 Effective ionization coefficients in CO_2, SF_6, CF_3I, Air and CF_3I/CO_2 at different ratios [41]. 33
2.15 Breakdown voltage characteristics of CF_3I/CO_2 mixtures (Positive polarity) [27]. 34
2.16 Breakdown voltage characteristics of CF_3I/CO_2 mixtures (Negative polarity) [27]. 34
2.17 PD inception voltage comparison between CF_3I and SF_6 at different pressures [22]. 35
2.18 PD inception voltage comparison between CF_3I/CO_2 and SF_6/CO_2 both with (30%/70%) ratio at different pressures [46]. 36

3.1 Pressure vessel dimensions [23]. 38
3.2 Pressure vessel in the HV laboratory. 38
3.3 Internal view of the pressure vessel. 39
3.4 38 kV bushing [9]. 40
3.5 Data sheet AC transformer. 40
3.6 Haefely RCR divider data sheet 41
3.7 Haefely RCR divider. 41
3.8 Gas extractor unit [23]. 42
3.9 Relation between normalized (V_b/E_b) and ratio R_{in}/R_{ext}. . . 44
3.10 30 mm HV-electrode 45
3.11 Coaxial geometry 45
3.12 Coaxial geometry dimensions 46
3.13 External enclosure. 47
3.14 Central enclosure. 47
3.15 Plane-plane dimensions [9]. 48

4.1 Half section of coaxial geometry model. 51
4.2 Half section of the complete model. 51
4.3 Ground boundaries set in the COMSOL model. 53
4.4 Mesh result of the whole COMSOL model. 55

4.5 Mesh zoomed in the HV electrode region. 56
4.6 Mesh zoomed in the bottom insulator region. 56
4.7 Electric potential at 1 kV. 57
4.8 Electric field lines with equal magnitudes (kV/cm). 58
4.9 Electric field distribution (kV/cm). 58
4.10 Zoom on the maximum of the electric field (kV/cm). 59
4.11 Electric field norm along the conductor surface. 60
4.12 Electric field lines in the coaxial geometry. 61

5.1 Capacitance C in the model. 63
5.2 Capacitance geometry views. 64
5.3 Equivalent circuit of the capacitance test. 66
5.4 Capacitive test setup in the laboratory. 66
5.5 Oscilloscope initial conditions. 67
5.6 Oscilloscope filtered output. 67
5.7 Measurements results. 68
5.8 Capacitance test results. 69
5.9 Capacitance results comparison. 70

6.1 Equivalent circuit of breakdown voltage test. 72
6.2 Current transformer characteristics. 73
6.3 Heights of the particles. 73
6.4 Diameters of the particles. 74
6.5 Particles applied to the HV electrode. 74
6.6 Example of a breakdown voltage measure obtained with the big asperity attached on the HV electrode in the coaxial geometry. 75
6.7 Exponent m for air density correction function of g [19]. . . 78
6.8 Exponent w for air density correction function of g [19]. . . . 78

7.1 Example of the most common internal defects [44]. 81
7.2 Equivalent circuit of first PDIV test. 83
7.3 Low-inductance resistor box. 84
7.4 Metal protrusions used in the preliminary PDIV test. 85
7.5 PDIV test result with HV electrode in clean condition. 87
7.6 PDIV test with small protrusion in the middle of HV electrode. 87
7.7 PDIV test with a big protrusion in the middle of HV electrode. 87

7.8 Worst damage point in the HV electrode. 90
7.9 Roughness profile in correspondence of the worst damage. . . 90
7.10 HV electrode surface after polishing treatment. 90
7.11 Roughness profile after polishing treatment. 90
7.12 Equivalent circuit of the test setup for persistence method. . 92
7.13 Equivalent circuit of the test setup for oscilloscope auxiliary output method. 93
7.14 Persistence result after 2 minutes at V_{RMS}= 23 kV. 95
7.15 Persistence result after 2 minutes at V_{RMS}= 24 kV. 95
7.16 Current pulse detected at V_{RMS}= 23 kV. 96
7.17 Current pulse detected at V_{RMS}= 24 kV. 96
7.18 Example of a PDIV measure with the oscilloscope output pulse. 96
7.19 Persistence result after 2 minutes at V_{RMS}= 22 kV. 97
7.20 Persistence result after 2 minutes at V_{RMS}= 22,5 kV. 97
7.21 Current pulse detected at V_{RMS}= 22,5 kV. 98
7.22 Example of a PDIV measure with the oscilloscope output pulse. 98
7.23 Persistence result after 2 minutes at V_{RMS}= 11,5 kV. 99
7.24 Persistence result after 2 minutes at V_{RMS}= 12 kV. 99
7.25 Current pulse detected at V_{RMS}= 12 kV. 100
7.26 Example of a PDIV measure with the oscilloscope output pulse.100
7.27 Persistence result after 2 minutes at V_{RMS}= 20 kV. 101
7.28 Persistence result after 2 minutes at V_{RMS}= 21 kV. 101
7.29 Current pulse detected at V_{RMS}= 21 kV. 102
7.30 Example of a PDIV measure with the oscilloscope output pulse.102
7.31 Persistence result after 2 minutes at V_{RMS}= 15 kV. 103
7.32 Persistence result after 2 minutes at V_{RMS}= 15,5 kV. 103
7.33 Current pulse detected at V_{RMS}= 15,5 kV. 104
7.34 Example of a PDIV measure with the oscilloscope output pulse.104
7.35 Persistence result after 2 minutes at V_{RMS}= 22 kV. 105
7.36 Persistence result after 2 minutes at V_{RMS}= 23 kV. 105
7.37 Current pulse detected at V_{RMS}= 23 kV. 106
7.38 Example of a PDIV measure with the oscilloscope output pulse.106
7.39 Plane-plane geometry inside the pressure vessel. 109

8.1 Q_{max} comparison of the pulse detected in the tests. 113
8.2 Spectrum analysis of the small metal protrusion. 114

8.3 Spectrum analysis of the big metal protrusion. 114

List of Tables

2.1 GWP of sulphur hexafluoride [7, 8] 16
2.2 CF_3I properties [9]. 19
2.3 Climate impact (GWP) comparison between SF_6 and CF_3I [7, 8, 9] 21
2.4 ODP comparison between SF_6 and CF_3I [40, 9] 21

3.1 R_{in}/R_{ext} comparison between the existing inner conductor diameters 45

4.1 Material properties assigned in the COMSOL model. 52

6.1 Values of exponents, m for air density correction and m for humidity correction, as a function of the parameter g [19]. . . 77
6.2 Breakdown voltage comparison between air and CF_3I/CO_2 mixture in different conditions. 79

7.1 PDIV comparison between air and CF_3I/CO_2 mixture in different conditions. 88
7.2 PDIV definitive results with air or CF_3I/CO_2 mixture in different conditions. 107
7.3 PDIV results with CF_3I/CO_2 mixture in a plane-plane geometry under different conditions. 110

List of Abbreviations

CF_3I Trifluoroiodomethane. i, ix, x, xv, 11, 19–36, 42, 43, 71, 75, 78–80, 82, 84, 86, 88, 89, 94, 101, 103, 105, 107, 108, 110–116

CT Current transformer. 72

DSO Digital storage oscilloscope. 73

E Electric field. 57, 59

E_b Breakdown field strength. x, 43, 44

FEM Finite element method. i, 49, 53, 111

GIL Gas insulated lines. i, 1–13, 18, 20, 21, 37, 43, 44, 48, 50, 59–61, 71, 78, 81, 82, 86, 91, 94, 109, 111, 112, 115

GIS Gas insulated substation. 13, 20

GWP Global warming potential. 15, 16, 18, 21

HV High voltage. xii, 7, 13, 39, 46, 50, 53, 54, 57, 59–61, 71–73, 89–91, 94, 99, 107–109, 111, 112, 115

IPCC Intergovernmental panel on climate change. 15

MV Medium voltage. 12

ODP Ozone depletion potential. 15, 17, 21

ODS Ozone depleting substances. 17

OHL Overhead line. 3, 6, 7, 10

PD Partial discharge. 22, 23, 81, 100, 108, 113, 115, 116

PDIV Partial discharge inception voltage. xii, xv, 35, 36, 43, 83, 86, 88, 89, 96–98, 100, 102, 104, 106–108, 110, 113, 115

SF_6 Sulphur hexafluoride. i, ix, x, xv, 1, 11–21, 23, 24, 27–29, 31–36, 81

V Voltage. 57

V_{b0} Breakdown voltage referred to standard atmospheric conditions. 76

V_b Breakdown voltage. x, 43, 44, 75, 76, 79, 80, 112

V_s Sparkover voltage. 35

Chapter 1

Introduction

1.1 Gas Insulated Lines (GIL) introduction

The power generation and transmission systems are constantly changing and developing. In these years, the percentage of renewable energy sources is increased significantly and in the future this part is expected to grow further. According to this scenario, using photovoltaic, biomass, hydropower, solar thermal, geothermal, onshore and offshore wind power plants, there will be a need to transfer large amount of electrical power from the production site (that is related to the availability of the renewable source) to the power consumption centre. This required restructuring of the electric power transmission network will need new reliable high-power transmission lines. The solution could be found combining overhead and gas insulated lines to have the best trade-off between costs and benefits. GIL would be perfect when is impossible to build a large overhead line, as an example in the case where the easiest technical solution is an underground transmission line or when, inside a densely populated area, the limits for the magnetic field and the disfiguring of the landscape are very important.
The first worldwide GIL was installed in Germany in 1974 at the voltage level of 400 kV [29]. This was the 1^{st} generation of GIL, it was characterised by using pure SF_6 as insulating gas and by not having an elastic bending.
The first gas insulated line of 2^{nd} generation was built in Geneva (Switzerland) in 2001 and the mainly innovations were the use of a gas mixture (for example 80% N_2 and 20% SF_6), an elastic bending and a deep reduction of the cost [29].

1.2 GIL technology

The basic structure of a GIL is composed of a cylindrical high-voltage conductor which is centrally held by the insulators within a grounded enclosure. Furthermore, the electrical insulation is provided by the pressurized gas that fills the empty space usually at 0,7-1,0 MPa [30].

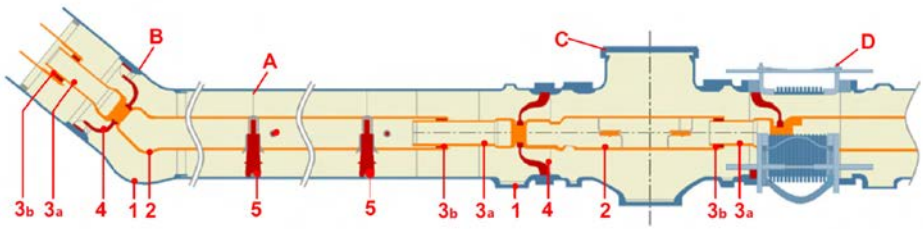

Figure 1.1: GIL main components [3].

It can be seen from the GIL scheme above (figure 1.1) that there are four different units [29]:

A STRAIGHT UNIT, that generally has a length up to 120 m, it is composed of many small units of 12-18 m and it can be bended up to a minimum radius of 400 m;

B ANGLE UNIT, which can handle angles from 4 to 90° and it is used when the elastic bending radius of the straight unit is not enough;

C DISCONNECTING UNIT, that is used to create independent gas compartments when it is necessary, and usually, these components are installed every 1000 or 1500 m;

D COMPENSATOR UNIT, which is used to compensate the movement of the GIL because of the thermal expansion, and it can manage around 400 m of enclosure pipe;

and the main components of the structure are [29]:

1. Enclosure, which is usually made from an alluminium alloy with a high accurancy to the roundness and diameter [30];

2. Inner conductor, that is made of electrical aluminium with high conductivity in order to minimize the electric transmission losses. Particular attention is given to the roughness of the surface that can be at most 10-20 µm;

3. Male (a) and female (b) sliding contacts, which are fundamental to compensate the thermal expansion of the conductor. They consist in a sort of plug where a multi-contact system can slide on, guaranteeing high system reliability;

4. Conical insulator, that is usually made of cast resin. Its functions are to centrally align the inner conductor (even during short-circuit) and to create a gas compartment up to 1,0 MPa overpressure;

5. Support insulator. There are three different types (one-leg, two-leg and three leg) and all of them are used to hold the conductor in the centre.

The visual impact of gas insulated transmission line is negligible if it is compared to an overhead transmission line (OHL), and it tends to zero if the GIL is under the ground. Figure 1.2 shows clearly this big difference between them.

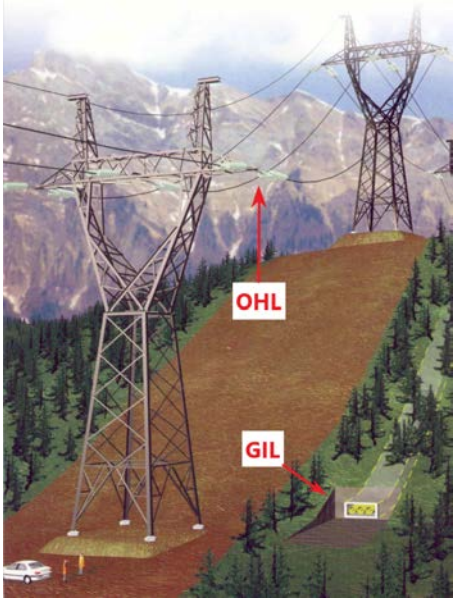

Figure 1.2: GIL and OHL comparison [3].

The installation methods for GIL are different and the choice depends on the type of application. Usually, the most common installations are:

(a) above ground;

(b) in a trench-laid;

(c) in a tunnel-laid;

(d) directly buried;

(e) in a shared structure.

(a) Above ground.

(b) Trench-laid.

(c) Tunnel-laid.

(d) Directly buried.

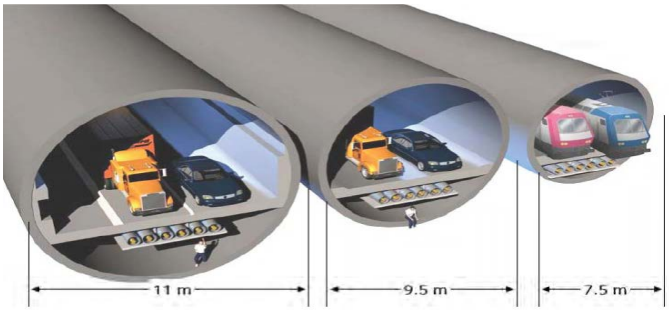

(e) Shared structure.

Figure 1.3: Tipical istallations techniques of GIL [3].

A substantial percentage of world-wide installed GIL are above ground. This solution is widely used in substations or in power plants because it is possible to avoid a lot of crossed overhead lines and all their consequent problems.
Typically, above ground means that GIL are over structural supports with a height of 5-8 m. This allows to have some useful space below but requires a lot of steel for the structures. Using this laying option, corrosion problem is also averted because, when the aluminium pipe is under atmospheric conditions, a thin oxide layer (few nanometers) is created. Thanks to this, the GIL will not be affected by corrosion agents thus, it can last for many years [29].

Trench-laid solution is often used in power plants or substations when it is preferable going under the ground for practical reasons. The trench is made of concrete and, once the GIL is installed, it is covered with a block of the same material. Usually, this laying option is a trade-off between a less expansive above ground and a more expansive tunnel solution (because the second one has to be accessible by the technical staff).
The corrosion protection is unnecessary either in this solution because the alluminium pipe creates, as in the previus case, an oxyde film. However, with the trench, particular attention is required to keep the GIL dry for most of the time (otherwise the oxyde layer could be damaged), thus drainage systems must be implemented [29].

Tunnel installation is a very compact solution to transfer power transmission without creating any visual impact on the environment and, in addition, it makes possible the complete agriculture of the soil above. Generally, they are used in hydroelectric power stations or dams, and they are accessible in order to control and repair, hopefully not very often, the GIL.
This type of laying method uses usually natural ventilation to remove the heat produced by the current but, if more power transmission capability is required, it is possible to install a forced one. As in the previous cases, no corrosion protection is needed thanks to the oxide film, but it is only important to ensure that GIL is not in permanent contact with water.
There are two different types of tunnel:

- the open trench-laid tunnel, which consists of a trench dug in the ground with tunnel segments made of concrete placed inside it. After GIL installation, the tunnel is covered with 1-2 m of soil [29];

- the bored tunnel, that normally is digged with a minimum depth equal to three times the diameter of the tunnel (under cities they can be also 20-30 m deep). The GIL are fixed to the tunnel wall, allowing enough space for inspections [29].

Directly buried laying option can be a concrete alternative in substations or between different countries thanks to its simple and consolidate laying techniques. This method is very close to the pipeline laying used for oil or gas therefore, it is a worldwide proven and reliable technology for long distance transmission. GIL installed in this way are an economical and quick solution for high-voltage transmission lines. Practically, they are continuously laid into a trench with the welding performed inside a welding tent and this means an extremely simple installation procedure. After the laid, 1 m of soil is the minimum of coverage, so the whole area above can be used again for agriculture. In addition, the soil around it has the double function of holding the pipe still and compensating the thermal expansion. This direct contact with the ground requires that the enclosure is protected against corrosion because otherwise water and minerals will corrode it. Usually, there are two methods to preserve the aluminium enclosure: the first (and widely used) is the passive corrosion protection and it consists in a layer of polyethylene (or polypropylene) and in an anti-corrosion layer that ensures no contact with oxygen for the aluminium. The second method is an active anticorrosive protection which, using a sacrifical electrode, provides a way for the current that can be used and thus corroded withuot any problem [29].

The installation of GIL in shared structures, such as tunnels and bridges, is certainly an option which must be taken into account. In this way, it is possible to obtain a reduction of the overall costs, higher efficiency of the structure and less disfigurement of the territory. It is a perfect trade-off between what the technological society needs and respect for nature. This idea can be realistic thanks mainly to the GIL shielding effect, which ensures a really high electromagnetic compatibility compared to overhead lines (OHL) and cables. In conclusion, gas insulated lines have shown a perfect behaviour in order to share a structure because they present no risks in case of failure, they have high reliability, the insulating gas does not age and in all the GIL history there is not been any failure so far [39],[4].

1.3 Benefits

Nowadays, overhead lines and cables are widely used in power transmission and they have been deep developed and optimised to achieve the best quality in these technologies. However, OHL public resistance is rising every year and being allowed to erect a new one is very problematic. The commissioning process can be very long and, sometimes, it may also never end with a line construction. On the other hand, HV-cables are not the perfect solution for long-distance power transmission and, in addiction, if a puncture occurs trough the cable insulating medium, it does not self-recover.
Considering all the previous aspects, GIL technology is a excellent candidate for the HV power transmission of the future. Its benefits are [29], [9]:

1. LOW EXTERNAL ELECTROMAGNETIC FIELDS

   Gas insulated lines generate lower magnetic field than overhead voltage or cables and, for the future power transmission choices, this will be very important (figure 1.4). The reason for this has to be sought into the way of how the enclosure is grounded: solid bound, which means that both the beginning and end of the external conductor are connected to the earth system. This grounding technique, in addition to the large cross-section of the return conductor, creates an intrinsic shield for the external magnetic field and thus provides the GIL with the best magnetic behaviour. Looking the Lenz's law it is possible to notice that, since the enclosure has a very low impedance, in the external conductor there will be an inverse induced voltage that drives a current which is 99% of the inner conductor current. The overlap of both currents produces a very low magnetic field compared with the huge amount of amps that the inner conductor is carrying.

2. HIGH RELIABILITY

   GIL is completely dedicated to power transmission without any request for active operations thus, it is very arduous that some problems happen in such a static situation. Moreover, the dielectric stress in the insulator is not very high and normally no special joints are present, so there are not critical parts. The proof is that, so far, no arc faults are registered with more than 300 km of installed gas insulated lines.

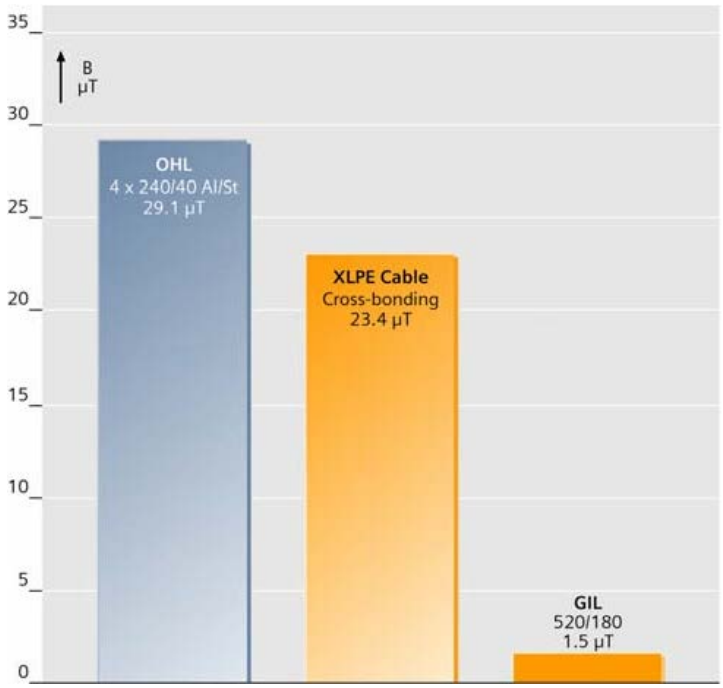

Figure 1.4: Ground level magnetic flux comparison between OHL, cable and GIL (last two 2 m deep) [33].

3. NO AGEING

The design of a gas insulated line is performed in order to reach, under normal condition, a maximum temperature of 60/70°C if it is installed in a tunnel, otherwise, around 40/50°C if it is directly buried. The maximum temperature for the GIL inner conductor is around 100/120°C, which is imposed by the cast resin insulators.
The dielectric design is based on the gas insulator and it tolerates a maximum electric field around 10 kV/mm (depending on the type of gas). Since it is well known that a stable gas medium does not degrade, possible electrical ageing could occur only on solid insulators. In a GIL this does not happen because usually for solid materials the electrical ageing starts around 30/50 kV/mm and in gas insulated lines the dielectric design is based on a value 3-4 times lower.
In conclusion, under normal operating conditions, the electric and thermal working points are perfect to make this power transmission technology unaffected by thermal or electrical ageing.

4. LOW TRANSMISSION LOSSES

The inner conductor and the enclosure are characterised by a large cross-section, so the resistance of these is very low. Usually, GIL have a resistance around 6-8 mΩ/km considering enclosures with an external diameter of 500-600 mm and an inner conductor diameter of about 6-15 mm. Transmission losses are proportional to the resistance of the conductor and to the square of the current. Obviously, having a low resistance of the system means also that the voltage drop is very limited. In power transmission lines, the current is very high thus, just a little difference of resistance can mean a big difference in term of losses. Figure 1.5 shows a comparison between the most widely used power transmission systems, and it is very clear the big difference that GIL provides than the others.

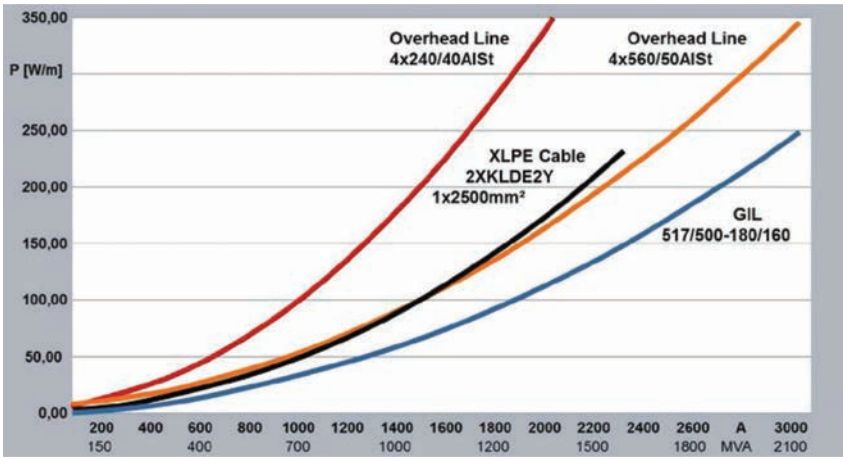

Figure 1.5: Power losses comparison between OHL, cable and GIL [36].

5. LOW CAPACITANCE

The capacitance of the GIL is usually very low and this brings many advantages for the easy management of the transmission line. Normally, it is known that kilometric capacitance of a GIL is ≈ 4 times greater than overhead lines and $\approx 4 \div 7$ times lower than cables. The benefit is that no compensation coils are required for distances up to 100 km (50 km for double GIL), which fits with almost the whole power transmission network. This is a great advantage because generally a single cable line needs reactive compensation every 24 km.

6. HIGH SAFETY

   GIL is a very safe way to transfer electric energy because it ensures that high-voltage parts cannot be directly touched, thanks to the enclosure. Furthermore, in case of failure the short-circuit current does not create an explosion and does not damage adjacent installation or people. This confirms, once again, that installation in a shared structure might be possible, such as in public infrastructures.

7. HIGH POWER TRANSMISSION CAPABILITY

   The gas insulated lines have a high power transmission capability, for example, at 550 kV it can carry up to 3000 MVA. Thanks to this, it can be said that GIL is the natural OHL substitute because they can transmit the same amount of power.

8. NO/OR VERY LOW VISUAL IMPACT

   Nowadays it is almost impossible to build an OHL because it is no more accepted by the population. GIL offers, again, the perfect solution because using a tunnel, trench or directly buried solution it may not be visible to the public and moreover, the land above can be used for agriculture.

9. NOT SENSIBLE TO ATMOSPHERIC CONDITIONS

   OHL are insulated using air thus if the area where the transmission line is installed is hostile, there can be some complications. For example, in a very polluted ambient or in a zone with a lot of sand, the isolators may have some troubles.
   With GIL all of these complications do not exist because the insulating gas is confined inside the enclosure and thus, it is not affected by other external problems.

Chapter 2

CF_3I as an SF_6 alternative insulating gas

2.1 Introduction

In Chapter 2, there will be presented a review of the insulating gas that is currently used for gas insulated lines and a new gas (or gas mixture) which could be an effective environmentally-friendly alternative. Sulphur hexafluoride (SF_6) is used as an insulating medium for high-voltage electrical equipment since 1937 [42] but nowadays, GIL systems are using principally a SF_6-N_2 mixture with different ratios, taking advantage of the synergetic effect. It is well known that sulphur hexafluoride is a strong non-eco-friendly gas and it was defined as one of the most harmful greenhouse gases in the 3rd Conference of the Parties to the United Nations Framework Convention on Climate Change (COP3) in 1992. Furthermore, looking at the Kyoto Protocol, it is necessary to find in a short time other solutions that can fit in the field of high-voltage insulation.
In order to replace GIL insulating gas, recent advancements in the research field have been carried out to develop some alternatives, such as SF_6-mixtures, new gases and new gas-mixtures. CF_3I gas and its mixtures are one of the most promising solutions for the use in gas insulated lines. Although many tests on this new gas have been performed, more research work has to be done in order to start to replace the SF_6 in high-voltage equipments. Finally, the properties of SF_6, the emerging synthetic gas CF_3I and a climate effects comparison between them will be presented below.

2.2 Sulphur hexafluoride (SF_6) review

In the 1930-40s the study of many potential insulating gases began and in 1950 was discovered the property of halogenated molecules, which is the ability to attach free electrons. Considering all the halogenated substances, the best insulating gas resulted to be sulphur hexafluoride SF_6. This conclusion was obtained comparing the most important properties such as stability, electric strength, liquefaction temperature and toxicity.
In the middle of the 20th century, in the USA the firsts SF_6 industries started to develop and to build sulphur hexafluoride circuit breakers, which quickly becoming widely used [34]. After 70 years of large use in medium and high voltage fields, there is an urgent need to change SF_6 with another gas because of its high global warming potential. In fact, in the EU Regulation No.517/2014 is written that SF_6 must be replaced with new insulation mediums at the end of 2020 (for MV-switchgears) or at the end of 2022 (for the remaining applications).

2.2.1 Properties

SF_6 is widely used in gas-insulated switchgears or GIL because comparing all of its properties with the other known gases, it offers outstanding performance as gas insulation medium. Its main properties are [29]:

1. high insulating capability;
2. high arc-extinction capability;
3. colourless and odourless;
4. non-flammable;
5. high chemical and thermal stability;
6. non-toxic;
7. five times heavier than air;
8. not soluble in water;
9. low boiling point;
10. high thermal conductivity.

The high dielectric strength of SF_6 is due principally to its strong electronegativity, which indicates that it has a high electron attachment, thus a large number of free electrons can be captured by its molecules. This property of SF_6 make it able to achieve a breakdown voltage almost three times higher than that of air at atmospheric pressure ($\approx$ 89 kV/cm) [17].
Nevertheless, the different behaviour that sulphur hexafluoride shows under uniform and non-uniform electric field has to be noticed. Normally, its dielectric strength under non-uniform electric field is not as good as under uniform field [13]. This can be considered an issue because sometimes in GIL conductors there may be a certain roughness or, in worse conditions, even the presence of conducting particles. Therefore, in order to prevent a total breakdown between the electrodes or just a partial discharge around them, in GIL it is necessary an extremely high accuracy during the design, production and installation phases.
The chemical characteristics of the SF_6 make it perfect for a gas insulated line for many reasons.
First, it can ensure a long term chemical-thermal stability and no possibility of chemical reaction with the HV-electrode, enclosure or insulators. This means both reduced maintenance and long life of the structure.
Secondly, it provides an intrinsic safety for the transmission line and for the maintenance staff because no fire, explosion and toxicity risks are taken using SF_6 as insulation medium.
In addition, the high thermal conductivity of SF_6 allows an easy heat exchange between the HV-conductor and the enclosure, thus the external environment. Thanks to this, it is possible for this type of transmission line to have a great power capability without high restrictions on the thermal aspect.
In conclusion, it is well known that SF_6 has a very low boiling temperature (-63,9°C at atmospheric pressure) [41]. This property is fundamental for the practical applications in order to ensure the gaseous state, which provides higher dielectric strength, for a wide range of pressures. The critical point, which delimits the boundary between a gaseous state and a liquid state, is characterised by a precise product temperature-pressure. Since a gaseous state is required to ensure good insulation, an ideal GIL insulating medium needs to have a very low boiling temperature at atmospheric pressure. The reason for this is because normally GIL and GIS work with an internal pres-

sure that is higher than the atmospheric one for two main reasons. The first one is because increasing the gas pressure is possible to achieve better dielectric strength of the gas. The second one is in order to ensure that in case of leak, no insulator gas comes out but the air goes inside it.
SF_6 has a greater density than air (6,07 kg/m^3 and 1,20 kg/m^3 respectively [32],[9]), thus the sulphur hexafluoride tends to stay at a lower quote than air and the consequence of that is a possible risk of suffocation.
In case of electrical discharge through the SF_6, toxic decomposition products are produced. Usually, the main by-products are:

- sulfuryl fluoride SO_2F_2;
- thionyl fluoride SOF_2;
- hydrogen sulfide H_2S;
- disulfur decafluoride S_2F_{10}.

These by-products are very harmful for the health because most of them can irritate nose, eyes and throat. Particular attention has to be given to S_2F_{10} because its toxicity is higher than phosgene (used in the World War I as chemical weapon) and some studies have shown that rats die within 8 hours exposure to 1 ppm of it [47].

2.2.2 SF_6 climate impact

Sulphur hexafluoride is a widely used gas in many sectors such as in the metallurgy, aeronautics and, obviously, electrical. In metallurgy, SF_6 is used in correspondence of aluminium and magnesium melting process in order to clean the casting forms since it is an inert gas. However, this sector does not release huge quantities of sulphur hexafluoride because after the process it usually decomposes for most of it and only 1,5% is released.
In aeronautics, SF_6 is used as insulation medium for the conductor of the antenna. When the plane goes up, SF_6 is liberated in the atmosphere to balance the pressure. On the other side, when the plane descends, sulphur hexafluoride is filled in the antenna system from an on board tank. Estimations of SF_6 released for each plane talk about $\approx$ 750 kg per year, and considering the huge amount of planes that every day fly everywhere, the SF_6 released by this sector is in the order of hundreds of tons per year [35].

The electrical industry is, without any doubts, the principal user of the sulphur hexafluoride since its great insulating performance has been discovered. The world total amount of SF_6 stored right now in electrical equipment is in the order of 10^5 tons and it is still increasing. Due to this wide use, the electrical sector is the main responsible of the large quantity of SF_6 emissions and, for this reason, research must to develop other reliable solutions for the sake of our world. Normally, the insulator gas remains inside the electrical equipments up to its end-of-life (≈40 years) and just a negligible part is emitted during this period. The leakages for new electrical equipments are under 0,5% but, unfortunately, after around 30 years there is a considerable increase which outstrips 2%.
Although it is necessary to decrease the leaks during the working life, most of the SF_6 is released during the production, testing, installation and disassembly of the electrical equipments. Thus, in the immediate future, more attention is required during all the above mentioned phases and, furthermore, the adoption of gas-collection infrastructures must be necessarily implemented in the worldwide [35].
If no action is taken, the anthropogenic emission of strong greenhouse gases will change in a permanent way the world climate. As an example, the air samples collected from Antarctic show that in the pre-industrial period the sulphur hexafluoride present in the atmosphere was less than 6,4 parts per quadrillion (10^{24}). Nowadays, the current SF_6 abundance in the air is three orders of magnitude higher and it is destined to increase if no action will be taken [35].

In order to understand in total the climate impact of the SF_6, it is necessary to define properly the meaning of the three most important parameters:

- global warming potential (GWP);
- ozone depletion potential (ODP);
- atmospheric lifetime.

The global warming potential (GWP) was introduced for the first time in the First IPCC Assessment in the 1990 [7]. This purely physical index is very useful in order to easily compare the global warming impacts of different gases.

Global warming potential index definition given in the IPCC assesment (2007) [8] is:

GWP index is based on the time-integrated global mean RF of a pulse emission of 1 kg of some compound (i) relative to that of 1 kg of the reference gas CO_2.

$$GWP_i = \frac{\int_0^{TH} RF_i\,(t)\,dt}{\int_0^{TH} RF_r\,(t)\,dt} = \frac{\int_0^{TH} a_i\,[C_i(t)]\,dt}{\int_0^{TH} a_r\,[C_i(t)]\,dt} \tag{2.1}$$

where:

- TH is the time horizon;
- RF_i is the global mean radiative forcing (RF) of component gas i;
- a_i is the RF per unit mass increase in atmospheric abundance of component i (radiative efficiency);
- $[C_i(t)]$ is the time-dependent abundance of gas i;
- a_r is the RF per unit mass increase in atmospheric abundance of reference gas CO_2 (radiative efficiency);
- $[C_r(t)]$ is the time-dependent abundance of the reference gas CO_2;

The numerator and denominator are called the absolute global warning potential (AGWP) of component gas (i) and the reference gas (CO_2) respectively. It is important to note that RF is referred to the energy per unit area, per unit time, absorbed by the greenhouse gas.

[1] SAR=Second Assessment Report (1995)

GLOBAL WARMING POTENTIAL					
Gas	**Radiative Efficiency (W m^{-2} ppb^{-1})**	**SAR[1] (100-years)**	**20 years**	**100 years**	**500 years**
Sulphur Hexafluoride (SF_6)	0,52	23900	16300	22800	32600

Table 2.1: GWP of sulphur hexafluoride [7, 8]

Ozone is a gas which is normally present in the stratospheric layer of the earth. This gas is very useful in order to do not let pass the ultraviolet radiation produced by the sun, which can heavily damage the skin tissue. Since the 1970s, it has been noted that ozone concentration in the stratospheric layer was decreased, especially near the Earth's polar regions (ozone hole). The source of the problem was found into the continuous increasing of the ozone-depleting substances (ODS), such as halogen gas, solvents and propellants principally due to anthropogenic activity. These substances can decrease the amount of ozone in the stratosphere thus, their use or production must be drastically reduced or banned.
The ozone depletion potential (ODP) is a simple relative index used for quantifying the different effects of various compounds in the ozone layer. ODP indicates the attitude of the i-compound to damage the ozone layer relative to the effects of a reference molecule (CFC-11 or $CFCl_3$) [37].

$$ODP_i = \frac{Global\ \Delta O_3(z,\Theta,t)\ due\ to\ substance\ i}{Global\ \Delta O_3(z,\Theta,t)\ due\ to\ CFC-11} \tag{2.2}$$

where:

- z is the altitude;
- Θ is the latitude;
- t is the time;

The ODP for sulphur hexafluoride is negligible because it does not react with the other gases in the stratosphere. This behaviour is due to the fact that SF_6 is chemically inert thus, it does not deplete a relevant quantity of the amount of ozone present.

The atmospheric lifetime is another important parameter to quantify the climate impact of a greenhouse gas. In 1999 Jacob [20], using the concept of a one-box model, defined the atmospheric lifetime as the average time τ that a molecule of species X remains inside the box.
The mathematical formula used is:

$$\tau = \frac{m}{F_{out} + L + D} \tag{2.3}$$

where:

- m is the mass of the substance X inside the box (kg);
- F_{out} is the flow of X outside the box (kg/yr);
- L is the chemical loss of X (kg/yr);
- D is the deposition of the substance X (kg/yr);

Studies have reported that SF_6 has an extremely long atmospheric lifetime (τ = 3200 years [7, 8]) and this is due to its high resistance to degradation. In conclusion, the long atmospheric lifetime and the huge GWP of sulphur hexafluoride make it the strongest greenhouse gas in the world.

2.2.3 SF_6 mixture

In gas insulated lines, the use of SF_6 mixed with other gases is widespread, and the reasons for this choice are mainly two. Firstly, the cost of sulphur hexafluoride is very high regarding the huge amount of gas that a GIL requires. Secondly, the insulator gas used in GIL need just a high insulation capability and not arc-quenching properties. Thus, a mixture can be used in gas insulated lines thanks to the fact that the insulation capability is still high even if only a small percentage of SF_6 is used in the mixture (synergistic effect). Since 1970s, nitrogen gas (N_2) is widely used in high voltage mixtures with SF_6 due to its good synergism with sulphur hexafluoride. N_2 is an inert gas because its molecules do not react with others molecules of different materials. N_2 is not an electronegative gas and therefore, it can not attach free electrons to its molecules. N_2 can be easily produced from normal air and, for this reason, it is widely available. The most used SF_6-N_2 ratio in GIL is 20%/80% and its insulation capability is around 70-80% of pure SF_6[29].
Despite using a mixture the amount of SF_6 used is significantly reduced, it is necessary to find another reliable insulating gas/mixture in order to make the GIL technology more eco-friendly. In conclusion, as soon as competitive alternatives will be mature and present in the market of insulating gases, stricter policies against the use of SF_6 must be implemented by national and international governments.

2.3 Trifluoroiodomethane (CF_3I) review

Trifluoroiodomethane (CF_3I) is an emerging synthetic gas which is being studied as an eco-friendly alternative to SF_6. The attention was given to this particular alternative of Halon 1301 (a fire extinguishing gas) thanks to its fantastic physical, chemical, thermodynamic and electrical properties. Trifluoroiodomethane molecule is formed by three fluorine atoms, one iodine atom and one central carbon atom as shows the figure 2.1. Iodine and carbon atoms have a quite high electronegativity but CF_3I is also composed by one fluorine atom, that is the highest electronegative atom in nature. This means that the CF_3I molecule cannot lose electrons easily but rather, it can absorb free electrons in order to delay the discharge initiation.

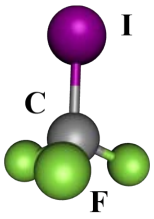

Figure 2.1: CF_3I molecular structure [14].

2.3.1 Physical and chemical properties

CF_3I physical and chemical characteristics are quite similar to SF_6. Trifluoroiodomethane main properties are:

Molar mass [g/mole]	196
Appearance	Colourless
Solubility in water	Slight
Odour threshold	Odourless
Boiling point at 1 atm [°C]	-22,5
Critical temperature [°C]	122
Critical pressure [MPa]	4,04
Density [kg/m^3]	8,14

Table 2.2: CF_3I properties [9].

Among these properties, particular attention has to be given to the boiling point at atmospheric pressure (0,1 MPa (abs)). Basically, the boiling point is the temperature value at which a liquid boils and turns to vapour. When an insulating gas is used, is strictly not recommended going below the boiling point because the gas starts to liquefy and therefore the insulation is compromised.
Normally, the pressure of the insulating gas inside a GIL is greater than atmospheric pressure for the reasons explained in the previous chapter.
It can seen from table 2.2 that CF_3I has a high boiling point at atmospheric pressure (-22,5 °C) instead for SF_6 is much lower (-63,9 °C).
Figure 2.2 shows the behaviour of the boiling temperature when the saturation vapour pressure changes. It is worth noting that with a small increment of the pressure the CF_3I boiling point goes to higher temperatures, and this represent a little issue for the practical use of it. For example, considering a widely used pressure value for GIL or GIS of 0,5 MPa (abs), the boiling point of pure CF_3I is around 25 °C.
This means that is impossible to use trifluoroiodomethane in electrical equipments without have a liquefaction of the gas. A solution to this important problem will be explained in the next section (CF_3I-mixture).

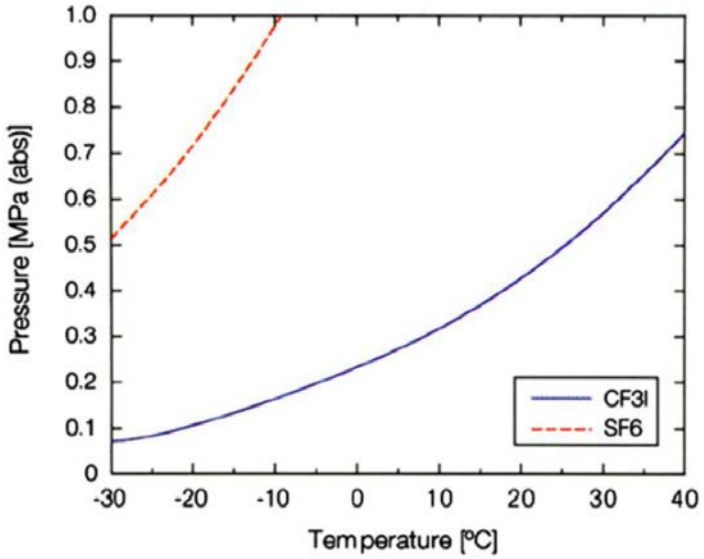

Figure 2.2: Boiling temperature vs absolute saturation vapour pressure with CF_3I and SF_6 [40].

2.3.2 CF_3I and SF_6 climate impact comparison

SF_6, as previous explained, has a very long atmospheric lifetime and a huge global warming potential. All of these issues makes sulphur hexafluoride a really harmful gas for the earth climate.
On the other hand, table 2.3 shows that the environmentally friendly alternative CF_3I has a very low GWP and an atmospheric lifetime around few days.

		GLOBAL WARMING POTENTIAL				
Gas	**Atmospheric lifetime (years)**	**Radiative Efficiency (W m^{-2} ppb^{-1})**	**SAR[1] (100-years)**	**20 years**	**100 years**	**500 years**
SF_6	3200	0,52	23900	16300	22800	32600
CF_3I	0,005	0,23	-	1	1	<1

Table 2.3: Climate impact (GWP) comparison between SF_6 and CF_3I [7, 8, 9]

[1] SAR=Second Assessment Report (1995)

The low GWP is due to the weak bond between carbon atom and the iodine atom, because it decompose easily and quickly in the atmosphere thanks to the solar light [26]. At this point the iodine goes up to the troposphere and it is finally removed with the rain.
Regarding the ozone depletion potential, it was antecedently reported that SF_6 does not have any impact. On the contrary, CF_3I has a quantified impact, even if is very low. This little bad influence that CF_3I has to the ODP is due to the fact that a small percentage of dissociated iodine reaches the stratosphere and reacts with the ozone layer.
In conclusion, assuming that if the CF_3I will be used as gas insulation medium for GIL, the amount of leakages should not create problems to the ozone layer and, considering its low global warming potential and its really short atmospheric lifetime, CF_3I is indubitably a better solution than SF_6 for what concern the climate impact.

Gas	**ODP**
SF_6	-
CF_3I	0,006÷0,012

Table 2.4: ODP comparison between SF_6 and CF_3I [40, 9]

2.3.3 By-products

Researchers [21] presented the decomposition by-products of CF_3I under the occurrence of partial discharges (PD). PD activity was measured from the cumulative charge (q_c) and the by-products were analysed using a mass spectroscopy detector (GC-MS) and a gas chromatography.

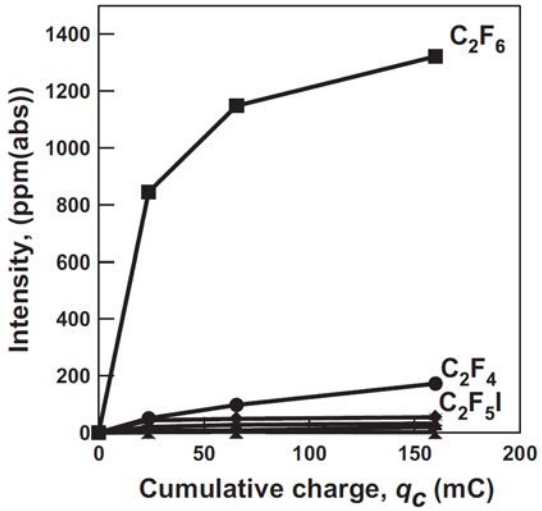

(a) By-products intensity up to 1400 ppm.

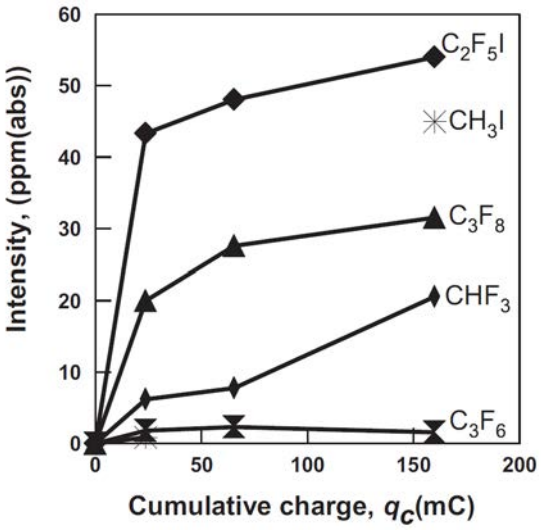

(b) By-products intensity up to 60 ppm.

Figure 2.3: Gaseous by-products as a function of cumulative charge q_c at 18 kV_{rms} (80% of V_b) [21].

The relation between gaseous by-products and cumulative charge q_c produced by PD is shown by figure 2.3.
In particular, figure 2.3a shows that the prevailing by-products are hexafluoroethane (C_2F_6), tetrafluoroethane (C_2F_4) and pentafluoroethyliodide (C_2F_5I) with 1300, 200 and 55 ppm respectively. C_2F_6 is the predominant by-product and this suggests that a similar reaction as photolysis reaction of CF_3I (equation (2.4)) occurs when PD activity is present in the gas.

$$2\,CF_3I \xrightarrow{h\upsilon} 2\,CF_3^{\cdot} + 2\,I^{\cdot} \longrightarrow C_2F_6 + I_2 \tag{2.4}$$

On figure 2.3b, other gas by-products detected with an intensity below 50 ppm are shown. The analysis revealed the presence of octafluoropropane (C_3F_8), trifluoromethane (CHF_3), hexafluoropropene (C_3F_6) and methyliodide (CH_3I). In addition, it is interesting to note, from both figures, that the by-products have an abruptly increase when the cumulative charge q_c is between 0 and 30 mC. Then, when q_c is above 30 mC, the by-products quantity increases gradually.
Finally, the study [21] was interested on the stability of the by-products produced. The test was performed applying a continuous PD stress condition on CF_3I for 20 hours and the results show that all the amount of by-products remain stable except methyliodide (CH_3I) .

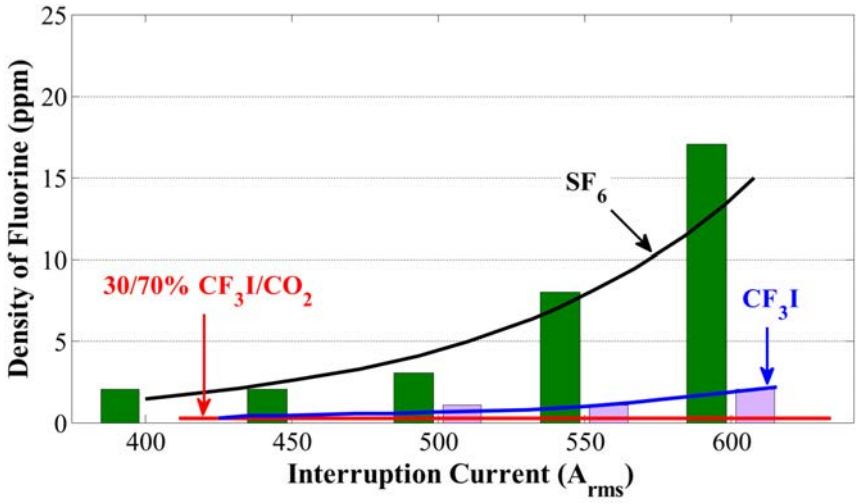

Figure 2.4: Fluorine density comparison between pure SF_6, CF_3I and CF_3I-CO_2 30/70% [27, 9].

Researchers [27] investigate also on the density of iodine and fluorine by-products with CF_3I gas and CF_3I-mixtures.
Basically, three fluorine atoms compose trifluoroiodomethane molecule, therefore it is expected from fluorinated gases that after current interruption some fluorine is formed. This by-product is especially important because is toxic and, moreover, is harmful for insulating material.
Figure 2.4 presents a comparison between SF_6 and CF_3I based on the amount of fluorine by-product produced. It is important to note that the test procedure was to interrupt the current once only for every value and then measure the amount of fluorine produced. It can be seen from these results that with SF_6 the fluorine increases exponentially with the amount of current interrupted. On the other hand, the fluorine produced with CF_3I is way lower and one reason for this is obviously the lower presence of fluorine in the molecule compared to sulphur hexafluoride. Finally, it is worth noting that with CF_3I-CO_2 mixture there is almost no fluorine detected after current interruption.

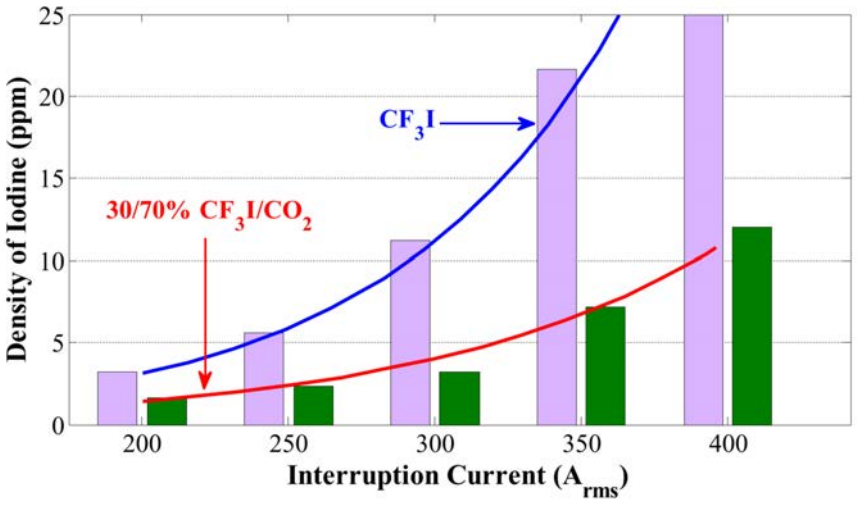

Figure 2.5: Iodine density comparison between pure CF_3I and CF_3I-CO_2 (30/70%) [27, 9].

Trifluoroiodomethane has, as discussed previously, a weak bond between carbon and iodine atoms. For to this reason, when a discharge occurs in CF_3I, iodine by-product is produced. Figure 2.5 shows the iodine density comparison between pure CF_3I and CF_3I-CO_2 (30/70%) mixture. The test

procedure, as in the previous case, intends to measure the amount of iodine produced after just one current interruption per each value. In the graph is clear that the iodine density has an exponential relation with the magnitude of the current interrupted and that the behaviour is the same either for pure CF_3I or for CF_3I-CO_2 (30/70%) mixture.
In addition, it is important to note that the ratio between the amount of iodine produced with CF_3I-CO_2 (30/70%) mixture and the pure CF_3I is around 1/3. This means that the volume of iodine produced is proportional to the trifluoroiodomethane present in the mixture.
The production of iodine happens when a discharge occurs and the result is that I_2 molecules will be deposited in a solid state on the nearby surfaces. This represents a risk for the systems which use CF_3I because:

- insulating capability decreases because iodine particles are metallic;
- iodine can corrode materials used in the gas system;

In particular, the insulation performance is seriously affected by iodine by-product because creates an easier condition for sparkover. Researchers [38] have analysed V-t characteristics in three different conditions regarding the purity of the electrode surfaces and the purity of CF_3I. After 1300 sparkovers under uniform electric field per each condition the results showed that the insulation performances of CF_3I were affected by 10% from all the by-products produced and the 5% of this quantity can be referable just to iodine.
In order to reduce the iodine by-product in an arc extinguisher chamber, [25] have studied a way to adsorb it. The adsorbent that was used is an

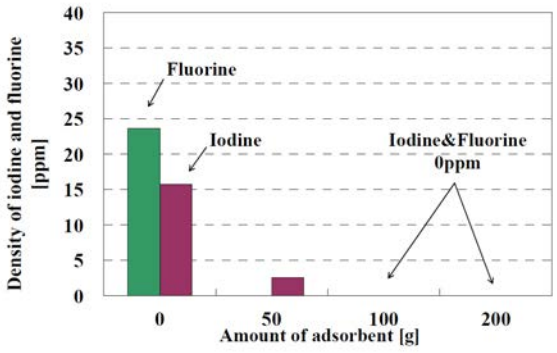

Figure 2.6: Iodine and fluoride density using adsorbent (C_2X) with CF_3I [25].

activated carbon C_2X. Figure 2.6 presents the result of [25] research. It can be seen that using an adsorbent, is possible to remove all the iodine. Nevertheless, it cannot adsorb iodine forever and thus, its effect gradually weakens with an increasing number of interruption.
In conclusion, C_2X is a reliable method to adsorb iodine by-product and greater is the quantity of the activated carbon, higher is the number of current interruptions granted.

2.4 CF_3I mixture review

CF_3I-mixtures are developed mainly to solve the high boiling point problem that pure CF_3I has. As previously explained, at 0,1 MPa CF_3I has a boiling point around -22,5°C (figure 2.7) but if it has to be used in electrical systems the pressure needs to increase. Thus, the gas starts to liquefy at higher temperatures losing all the benefits that a gas insulating medium has.
In order to decrease the boiling temperature, other gases such as nitrogen (N_2) and carbon dioxide (CO_2) were tried in mixture with CF_3I.
For a better understanding of how the boiling point is decreased using a mixture, it is necessary the Dalton's law [16]:

> *" The pressure in a mixture of different gases is equal to the sum of the pressures of the different gases as existing each by itself at the same temperature and with the same value of its potential. "*

$$p_t = p_1 + p_2 + ... + p_n = \sum_{i=1}^{n} p_i \tag{2.5}$$

Where:

- p_1,p_2,...,p_n are the partial pressures of each gas in the mixture;
- p_t is the total pressure of the mixture.

In this way, it is easy to understand that the boiling point of the CF_3I in a mixture is related only to its partial pressure. In other words, the partial pressure percentage of trifluoroiodomethane in the mixture corresponds with its percentage of the mixture ratio.
Figure 2.7 shows the boiling point behaviour when CF_3I is used in a mixture. Considering the 30%-CF_3I curve, it can be seen that at 0,5 MPa the boiling

point achieved is -12,5°C (instead with pure CF_3I was 25°C). In addition, from the 20%-CF_3I curve can be seen that it has an even better behaviour regarding the liquefaction temperature therefore, as was expectable, decreasing the CF_3I percentage in the mixture decreases its partial pressure and thus, its boiling point.
Finally, this result allows the CF_3I-mixtures to be used on electrical power systems with a pressure higher than atmospheric.

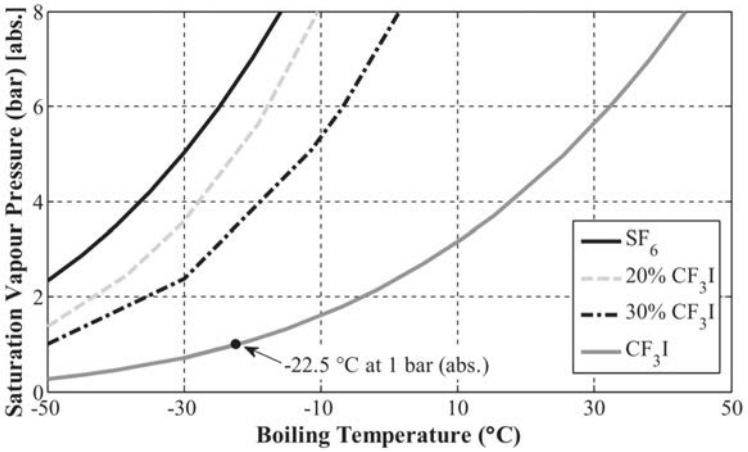

Figure 2.7: Boiling temperature at different saturation vapour pressure with CF_3I, CF_3I-mixtures and SF_6 [10].

Once determined the benefits of using CF_3I-mixture is important to define:

1. which molecule between nitrogen (N_2) and carbon dioxide (CO_2) is better for the insulating mixture;

2. which ratio of the mixture is the best.

Regarding the choice between CF_3I/N_2 mixture or CF_3I/CO_2 mixture is interesting to analyse the result of [45] study. This research has compared the AC breakdown voltage with SF_6/N_2, SF_6/CO_2, CF_3I/N_2 and CF_3I/CO_2 under quasi-uniform electric field and non-uniform electric field.
Figure 2.8 presents the breakdown voltage results with a sphere-sphere geometry that has a field utilization factor equal to 0,93 (quasi-uniform condition). Regarding the comparison between SF_6-mixtures and CF_3I-mixtures, it is worth noting that the sulphur hexafluoride mixtures have higher BV than trifluoroiodomethane mixtures. More interesting are the results be-

tween CF_3I/CO_2 and CF_3I/N_2 mixtures, they show a slightly better insulation capability of the CF_3I mixed with CO_2 than the CF_3I mixed with N_2.

Figure 2.9 presents the breakdown voltage results with a needle-plane geometry that has a field utilization factor equal to 0,23 (non-uniform condition). The results with CF_3I mixtures show that the one with CO_2 has still a slightly higher breakdown voltage than the N_2 one.
This means that, for what concern the mixture insulation capability, under AC voltage and under either quasi-uniform or non-uniform electric field, the CF_3I/CO_2 shows higher insulator capability than CF_3I/N_2.

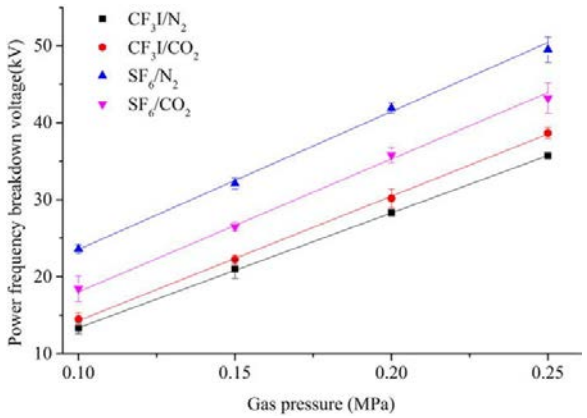

Figure 2.8: AC Breakdown voltage of CF_3I and SF_6 mixed with N_2 and CO_2 under quasi-uniform electric field [45].

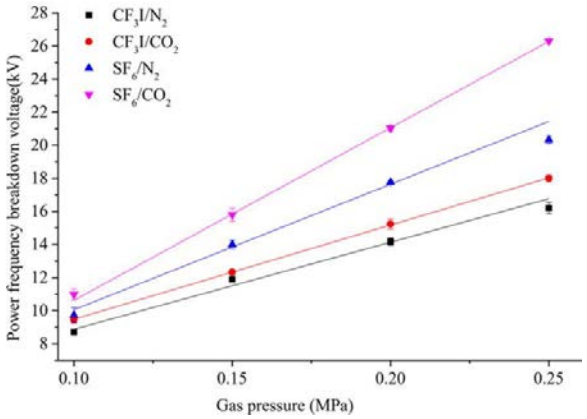

Figure 2.9: AC Breakdown voltage of CF_3I and SF_6 mixed with N_2 and CO_2 under non-uniform electric field [45].

The choice of the best ratio in a CF_3I/CO_2 mixture for gas insulated lines or gas insulated switchgears applications is a trade-off between:

- boiling point;
- insulation capability;
- quantity of iodine produced after a discharge;
- interruption capability.

As previously discussed, in order to have a low boiling point of the mixture and a slight production of iodine after a discharge, the CF_3I percentage should be as lower as possible. On the contrary, to achieve a good insulation capability the CF_3I quantity in a mixture should be as higher as possible. For what concern the interruption capability, researchers [26] analysed it in an arc-extinguishing chamber for CF_3I/CO_2 and CF_3I/N_2 mixtures at different ratios in two different conditions (SLF, BTF). It is worth to remeber, for a better understanding of the next results, that the interruption performance of pure CF_3I in SLF[1] condition are $\approx$ 0,9 times that of SF_6 and in BTF[2] condition are $\approx$ 0,67 times that of SF_6 [23, 26]. In the results, the interruption capability of SF_6 was taken as reference.

[1] SLF=Short Line Fault (1kA)

[2] BTF=Breaker Terminal Fault

Figure 2.10 shows that in SLF condition the CF_3I/N_2 mixture increases its interruption capability linearly in proportion with CF_3I content. On the other hand, with the CF_3I/CO_2 mixture the interruption capability increases non-linearly and it reaches the performance of pure CF_3I when the content is around 30%.

Figure 2.11 presents the results obtained with CF_3I/N_2 mixture where, again, it has a linearly increase of the interruption capability in proportion with the CF_3I content. CF_3I/CO_2, differently, shows an interruption capability that increase non-linearly and at 30% of CF_3I content it reaches the same performance as pure trifluoroiodomethane.

Finally, since the interruption capability with CF_3I/CO_2 reaches the saturation value when the ratio is around 30%/70%, it is no necessary to increase more the trifluoroiodomethane content.

In conclusion, looking for a trade-off between all the considerations previously made, is it possible to say that the ratio 30%/70% for the CF_3I/CO_2 mixture allows to reach good performance in all the aspects analysed.

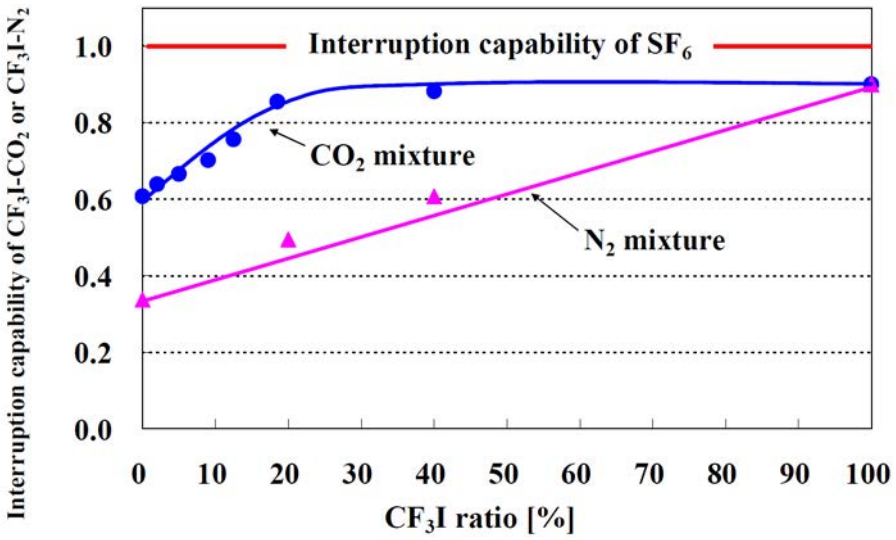

Figure 2.10: SLF interruption capability with CF_3I/CO_2 and CF_3I/N_2 mixtures [26].

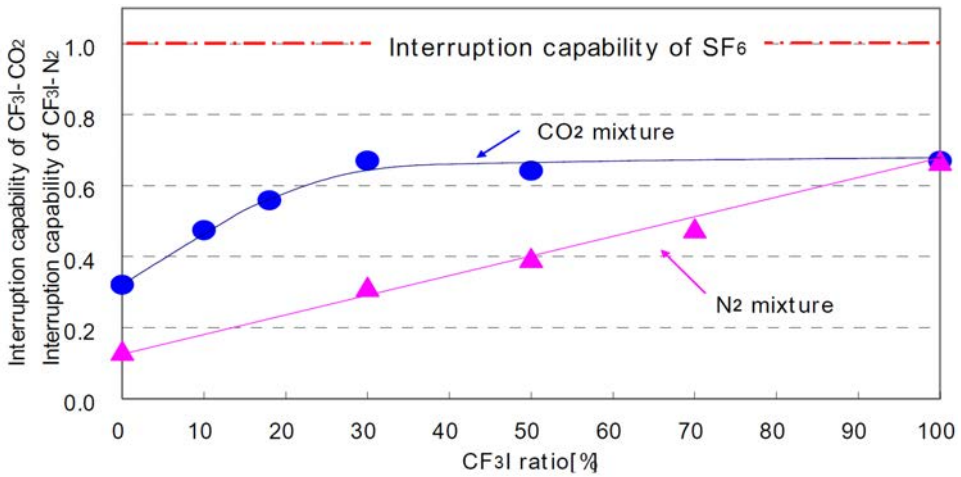

Figure 2.11: BTF interruption capability with CF_3I/CO_2 and CF_3I/N_2 mixtures [26].

2.5 CF_3I electrical properties

CF_3I is a relatively new alternative insulating gas which aims to replace SF_6 in the electrical application. In order to meet this goal, further studies have to be carried out to explore its properties and to confirm it or not as SF_6 successor. Many studies [42, 27, 41, 10] confirm that pure CF_3I dielectric strength is 1,2 times higher than of SF_6 in uniform electric field conditions, instead in non-uniform electric field is slightly lower than of SF_6.
The purpose of this section is to review the experimental tests performed so far in these recent years on CF_3I and on its mixtures.

2.5.1 Electron interaction properties

The capacity to reduce the number of free electrons is an ability that every insulating gas must have. Studies [43, 12] have found the electron interaction properties of CF_3I and CF_3I/CO_2 mixture and the results are reported briefly here.
The results that will be presented below are referred to the reduced electric field (E/N) which is the ratio between the electric field E (V/cm) and the gas density N (mols/cm^3). Its unit of measurement is Townsend (Td), that correspond to 10^{-17} V cm^2.

The electron drift velocity is a parameter that indicates the gas aptitude to slow down the electrons that are moving in the direction of the electric field. In order to be a good insulation medium, the electron drift velocity should be small so, electrons are slowed down by the gas and therefore, there is less energy to start an avalanche. Normally, it has been found out that with gas insulation mediums v_e increase linearly with reduced electric field (E/N).
Figure 2.12 and figure 2.13 show that the electron drift velocity v^e is lower with pure CF_3I than that of pure SF_6. In addition, it is clear that higher the CF_3I content in the mixture, lower is v_e. In conclusion, the results show that is possible to achieve the same v_e as pure SF_6 with the mixture CF_3I/CO_2 (70%/30%).

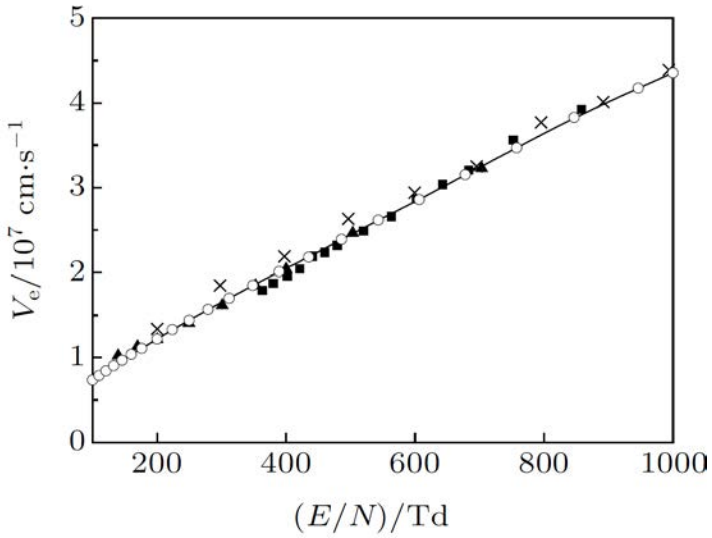

Figure 2.12: Electron drift velocity in CF_3I as a function of E/N [43], ■ [12], × [18], ▲ [28], ○ [43].

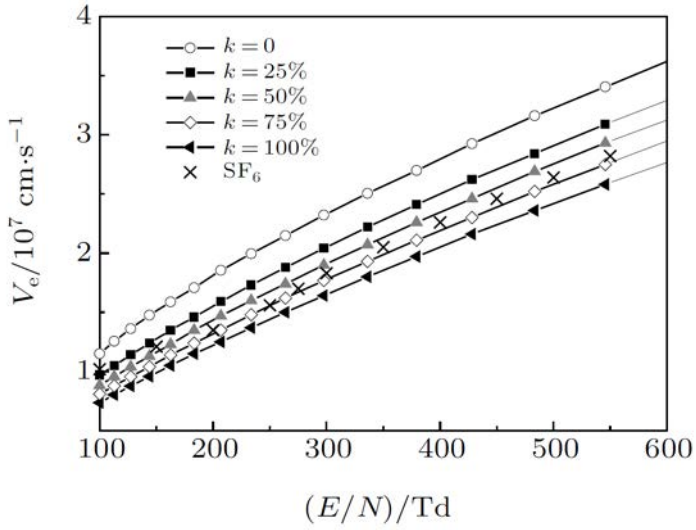

Figure 2.13: Electron drift velocity in SF_6 and CF_3I/CO_2 as a function of E/N at different CF_3I gas mixture ratio k [43].

The effective ionization coefficient of an insulation medium is the difference between the ionization rate (α) and the electron attachment rate (η). When α-$\eta > 0$ the ionization in the gas starts and the limit condition, where ionization is equal to attachment α-$\eta = 0$, is called limiting field strength or critical reduced field strength. It can be seen form figure 2.14 that effective

ionization coefficient is related to the critical reduced electric field strength (E/p). The results show that pure CF_3I has a critical reduced electric field equal to 108 kV/cm bar, instead the well known value for SF_6 is 89 kV/cm bar. This means, once again, that pure CF_3I has a dielectric strength 1,2 times that of SF_6.
For what concern the CF_3I/CO_2 mixtures, figure 2.14 shows that the critical reduced electric field strength for 10%/90%, 20%/80% and 30%/70% is 38,5 kv/cm, 47,4 kV/cm and 55,3 kV/cm respectively [40]. In addition, from this plot is worth noting that, once $(E/p)_{crit}$ is exceeded, the ionization grows quicker with pure CF_3I than CF_3I/CO_2 mixtures.
These last results confirm that CF_3I/CO_2 (30%/70%) is the main candidate mixture to replace SF_6 in high voltage equipments.

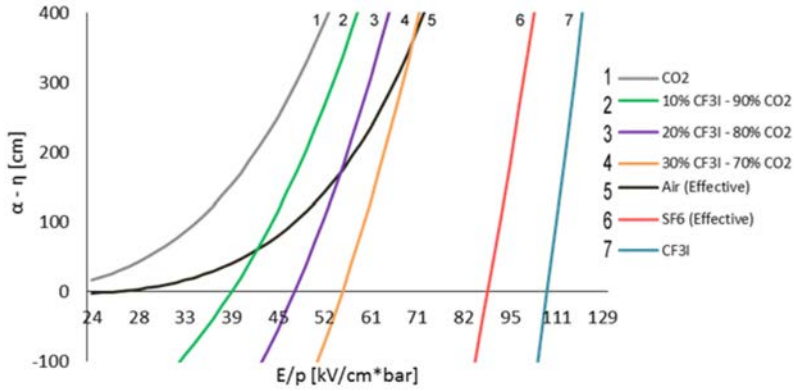

Figure 2.14: Effective ionization coefficients in CO_2, SF_6, CF_3I, Air and CF_3I/CO_2 at different ratios [41].

2.5.2 Breakdown voltage

Reaserchers [27] have compared the breakdown voltage characteristics of SF_6,CF_3I and CF_3I/CO_2 mixtures applying a standard lightning impulse voltage for fifteen times for each gas. The geometry used was a sphere-sphere (ϕ=50,8 mm and gap=10 mm) and the tests were carried out with 0,1 MPa pressure (abs). Figure 2.15 and figure 2.16 show a breakdown voltage result for both polarities. It is interesting to see, once again, that the pure CF_3I has a higher $U_{50\%}$ than SF_6, around 1,2 times. CF_3I/CO_2 insulation performance increases linearly with the CF_3I content. The same

dielectric strength of SF_6 is achieved by CF_3I/CO_2 (60%/40%) but it cannot be used due to its high boiling point thus, it should be used a mixture with 30% of CF_3I or less. For this reason, is interesting to note that for CF_3I/CO_2 (30%/70%) the insulation performance is about 0,75 to 0,80 times that of SF_6 [27]. In conclusion, this behaviour is explainable with the synergistic effect, which is when the mixture insulation performance does not change linearly with the CF_3I content [47].

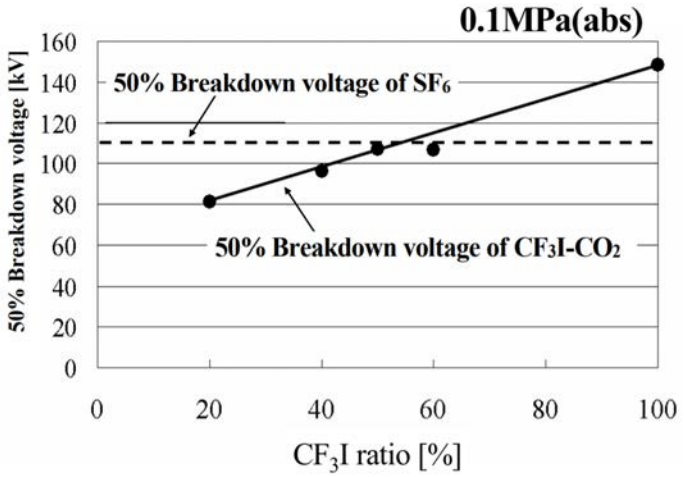

Figure 2.15: Breakdown voltage characteristics of CF_3I/CO_2 mixtures (Positive polarity) [27].

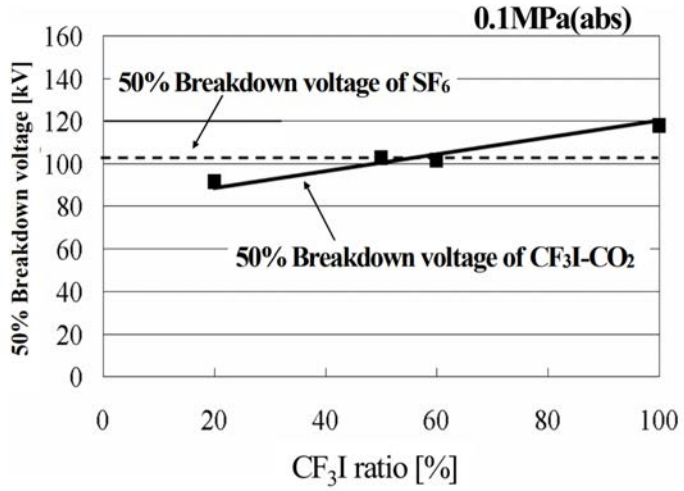

Figure 2.16: Breakdown voltage characteristics of CF_3I/CO_2 mixtures (Negative polarity) [27].

2.5.3 Partial discharge inception voltage

[22] has compared partial discharge inception voltage (PDIV) and breakdown voltage between pure CF_3I and pure SF_6 at different pressures. The geometry used was a needle-plane with 0,5 mm tip radius and a gap of 10 mm. Figure 2.17 presents the results obtained.

Firstly, it worth noting that the sparkover voltage V_s with CF_3I was just the 0,7 times that of the V_s with SF_6 at 0,1 MPa. Increasing the pressure (0,2 MPa) this difference increase because it was found a V_s for CF_3I 0,4 times that of the V_s with SF_6.

On the other hand, results shows that at 0,1 MPa it was found that $V_{PDI(-)}$ with CF_3I is almost the same with $V_{PDI(-)}$ in SF_6. For what concern the PDIV under positive half cycle, it was found that $V_{PDI(+)}$ with CF_3I was 1,7 times higher than $V_{PDI(+)}$ in SF_6 at 0,1 MPa. At 0,15 MPa, figure 2.17 shows that $V_{PDI(+)}$ with CF_3I was 1,4 times higher than $V_{PDI(+)}$ in SF_6. At 0,2 MPa $V_{PDI(+)}$ with CF_3I was not detected because it would have been too near to V_s.

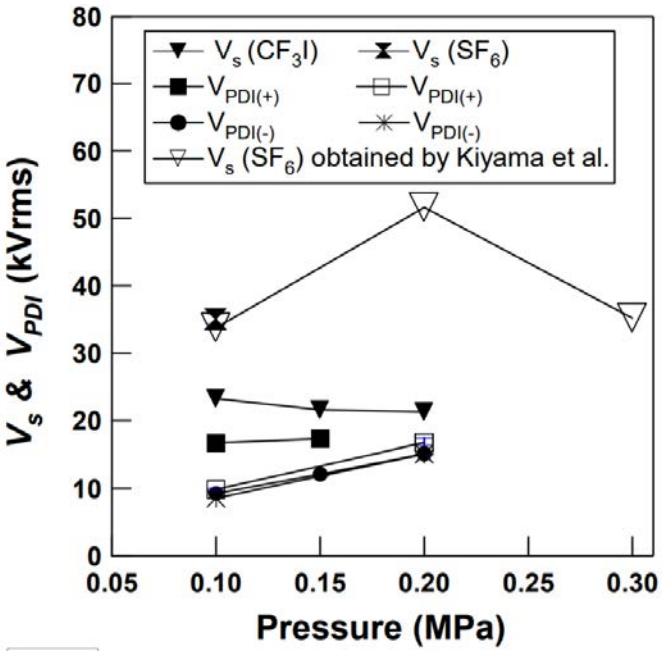

Figure 2.17: PD inception voltage comparison between CF_3I and SF_6 at different pressures [22].

Researchers [46] reported PDIV study during AC positive half cycle with CF_3I/CO_2 and SF_6/CO_2 mixtures at different ratios. The geometry used was a needle-plate with 0,3 mm tip radios and the gap could vary between 5, 10, 15 mm.

Figure 2.18 presents PDIV during positive half AC cycle with CF_3I/CO_2 and SF_6/CO_2 mixtures both at (30%/70%) ratio. These results show that $V_{PDI(+)}$ with CF_3I/CO_2 is higher than $V_{PDI(+)}$ in SF_6/CO_2 for the range of pressure 0,1÷0,3 MPa.

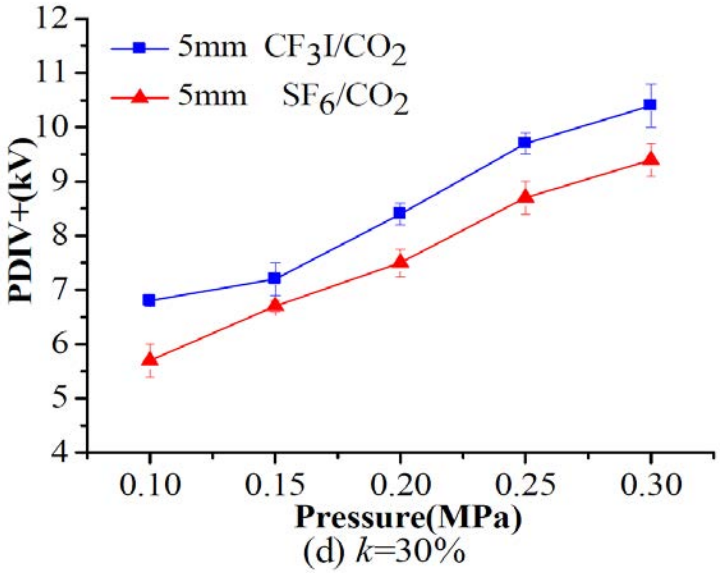

Figure 2.18: PD inception voltage comparison between CF_3I/CO_2 and SF_6/CO_2 both with (30%/70%) ratio at different pressures [46].

Chapter 3

Test equipment and geometries used

3.1 Introduction

In chapter 3 will be presented the laboratory test equipments such as pressure vessel, bushing and gas extractor unit that have been used during the development of this project. Then, a coaxial cylindrical geometry was chosen in order to represent a scaled prototype of a full-scale GIL and therefore, its dimensions and other practical choices will be presented and discussed. In the end, a plane-plane was chosen to consent a better comprehension of the results previously achieved.

3.2 Test equipment

3.2.1 Pressure vessel

The pressure vessel has been designed by a Cardiff University PhD student [23]. It is made of mild steel, with a maximum rated pressure of 10 bar (abs) and a volume of 0,0982 m^3 thus, 98,2 litres at atmospheric pressure. Figure 3.1 presents the vessel main dimensions. Two pressure gauges are installed on it, the first one is a vacuum gauge for measuring the vacuum level of the vessel before filling it with gases. The second one can measure the pressure while the vessel is filled and its range is from 0 to 7 bar (abs). In conclusion, the vessel has also a pressure release valve and it is set at 6 bar (abs) in order to evacuate the vessel, in case issues cause overpressure.

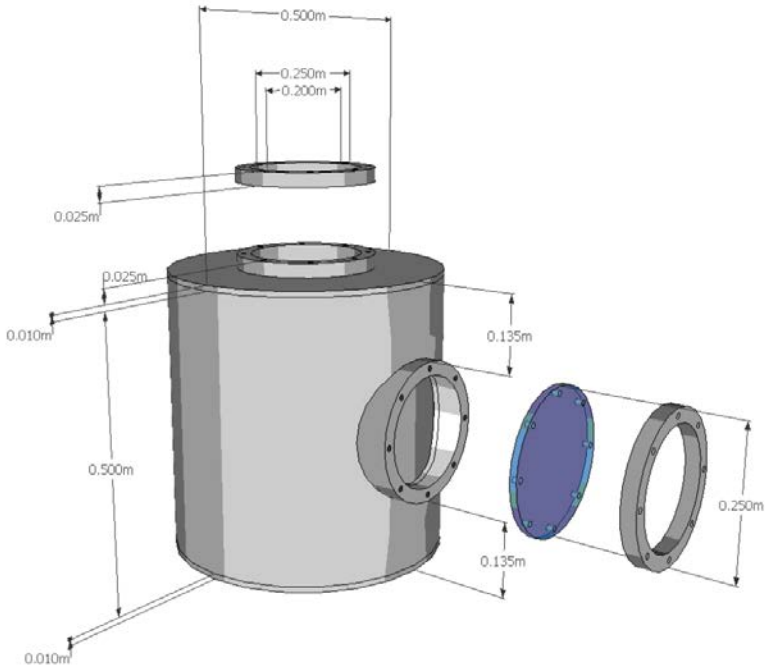

Figure 3.1: Pressure vessel dimensions [23].

Figure 3.2: Pressure vessel in the HV laboratory.

Figure 3.3 shows the internal conditions of the pressure vessel that was used during this project. Since it is made of mild steel, it produced some rust that cover all the inner surface.

Figure 3.3: Internal view of the pressure vessel.

3.2.2 Bushing

The high-voltage bushing is used to apply the AC voltage to the HV-electrode inside the vessel without touching grounded points or unwanted areas. The bushing used in this project (figure 3.4) is made of copper which is surrounded by silicone rubber. The rated AC voltage is 38 kV and its dry lighting impulse withstand voltage (BIL) is limited to 170 kV peak. It is important to note that, even if the transformer in the laboratory could achieve higher voltage, the AC limit in this project is 36 kV in order to respect a safety margin on the bushing.

3.2.3 Transformer

The transformer used in this project to increase the voltage in order to test under HV conditions is Ferranti 160804. The data sheet is shown in figure 3.5. It is a single phase transformer and its insulation medium is oil. The primary voltage is 220 V and the secondary voltage is either 50 kV or 100 kV, depending on the configuration of the HV side windings. During the tests, the HV side was connected in the way to have 50 kV thus, the apparent power of the transformer was 3,75 kVA.

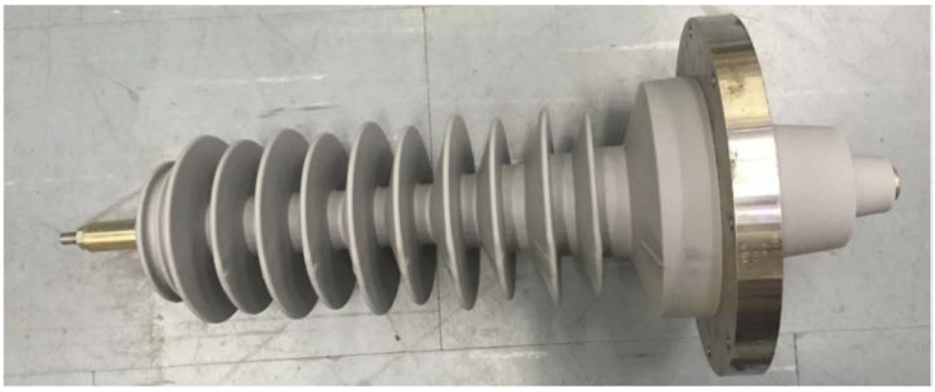

Figure 3.4: 38 kV bushing [9].

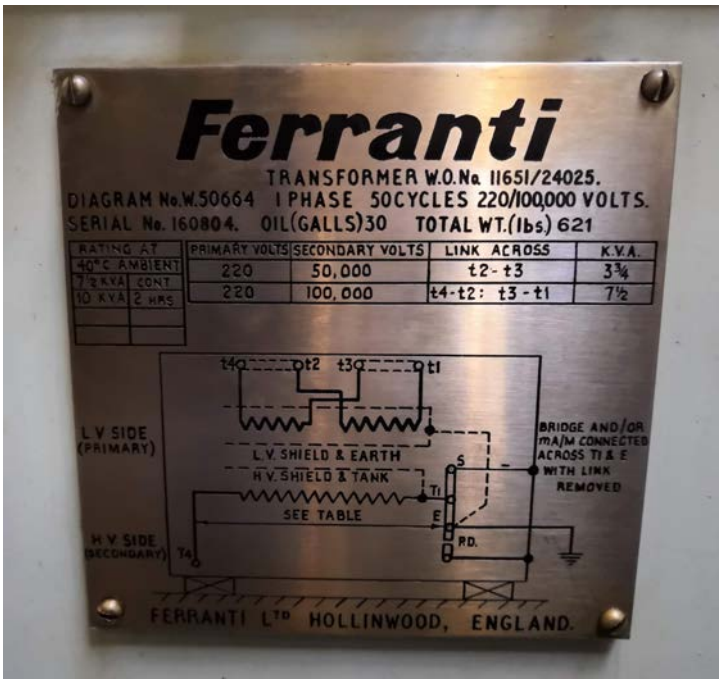

Figure 3.5: Data sheet AC transformer.

3.2.4 Divider

The divider used in order to measure the high voltage is Haefely RCR 150. It is a mixed R-C divider with a ratio of 3750:1 and its role is to scale down the applied voltage to levels safe for the recording devices (oscilloscopes, DAQ card etc.). From figure 3.6 is possible to note that the AC rated voltage is 50 kV and its other characteristics.

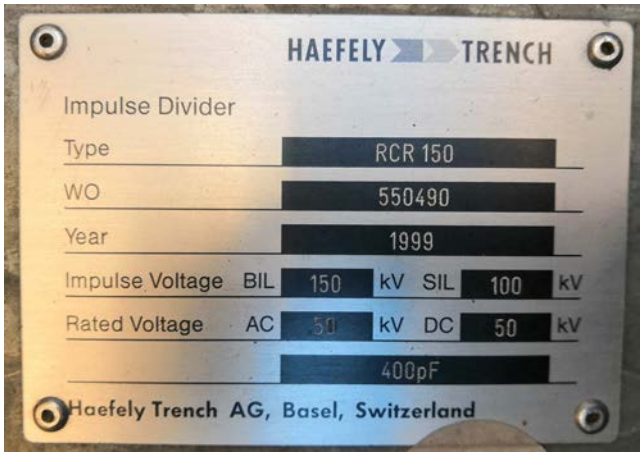

Figure 3.6: Haefely RCR divider data sheet .

Figure 3.7: Haefely RCR divider.

3.2.5 Gas extractor unit

The gas extractor unit is necessary to take out the CF_3I/CO_2 mixture from the vessel, storing it properly in a gas cylinder after each test. This system is made by DILO Company and its main components are a compressor, a vacuum compressor, a vacuum pump, a pre-filter and a storage cylinder. In the pre-filter unit, there is a dry filter cartridge that absorbs moisture and decomposition products from the gas used. Furthermore, there is also a particle filter that blocks solid particles and solid decomposition products. Therefore, after the recovery process, the gas resulted is purified, dried and ready for the next test.

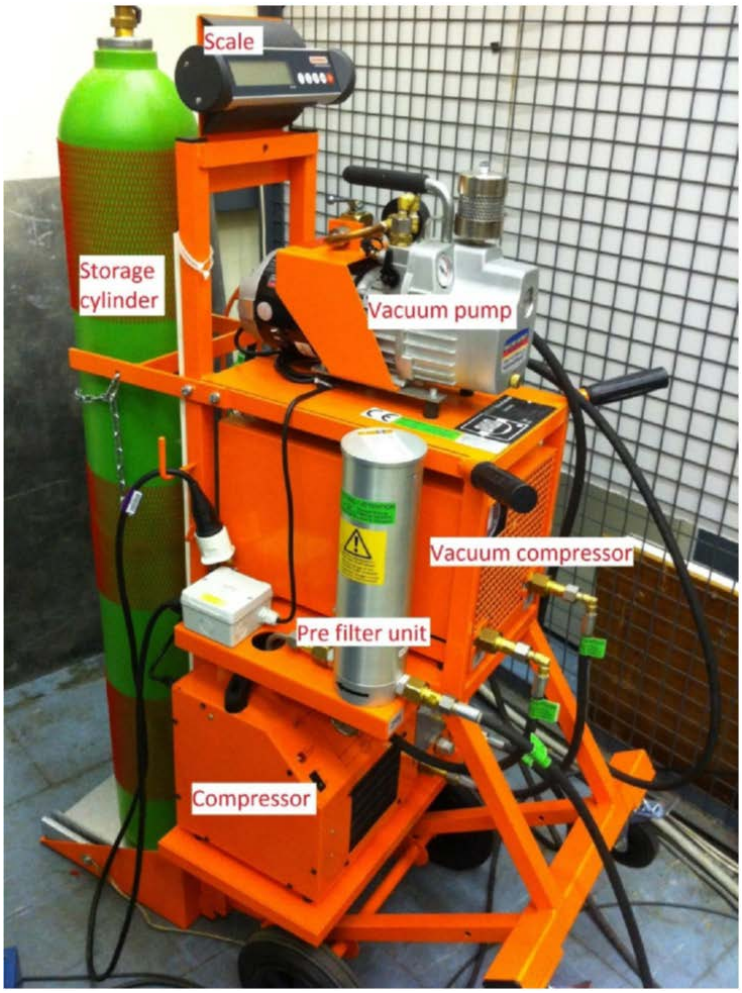

Figure 3.8: Gas extractor unit [23].

3.3 Coaxial geometry

In this project, a reduced scale coaxial system was used. The geometry was designed by a previous PhD student of Cardiff University.
The aim of this project is to investigate the AC breakdown voltage and PDIV characteristics with CF_3I/CO_2 (30%/70%) mixture in a reduced scale GIL. It is very interesting to understand how CF_3I/CO_2 mixture performs in a GIL geometry, because it can open new scenarios for a new generation of gas insulated line with CF_3I as main gas insulation medium.

3.3.1 Inner conductor choice

Initially, the coaxial geometry included one enclosure and many inner conductors of different diameter built from precedent researches. The present diameters were 8 mm, 10 mm, 15 mm, 20 mm and 30 mm. The main reason that made me choose one particular inner conductor diameter was the optimal ratio criterion. This is an important factor that is taken into consideration during the GIL design. In order to explain the optimal ratio criterion, it is worth to start from the maximum electric field formula for coaxial cylinders:

$$E_{max} = \frac{V}{R_{in} \cdot ln(\frac{R_{ext}}{R_{in}})} \tag{3.1}$$

where:

- R_{in} is the radius of the inner conductor;
- R_{ext} is the inner radius of the enclosure.

Now, considering that breakdown voltage V_b is the voltage applied when the breakdown field strength (E_b) is reached on the surface of the conductor, the equation (3.1) can be re-written as:

$$V_b = E_b \cdot R_{in} \cdot ln(\frac{R_{ext}}{R_{in}}) \tag{3.2}$$

Here, assuming E_b and R_{in} as constants, the optimal ratio between R_{ext} and R_{in} can be easily found calculating the maximum of the equation (3.2).

Its first derivative is obviously:

$$f'(x) \; = \; e(\, ln(\frac{R_{ext}}{R_{in}}) - 1 \,)$$

Thus, the optimal ratio condition is when:

$$ln(\frac{R_{ext}}{R_{in}}) \; = \; 1 \;\; \rightarrow \;\; \frac{R_{ext}}{R_{in}} \; = \; e \; \approx \; 2,72$$

In conclusion, starting from equation (3.2), considering the normalized ratio (V_b/E_b) and noting that, since in this case R_{ext}=45 mm is fixed, just R_{in} can vary, is possible to obtain figure 3.9. The graph shows clearly that in correspondence of the optimal ratio, the maximum breakdown voltage is achieved.

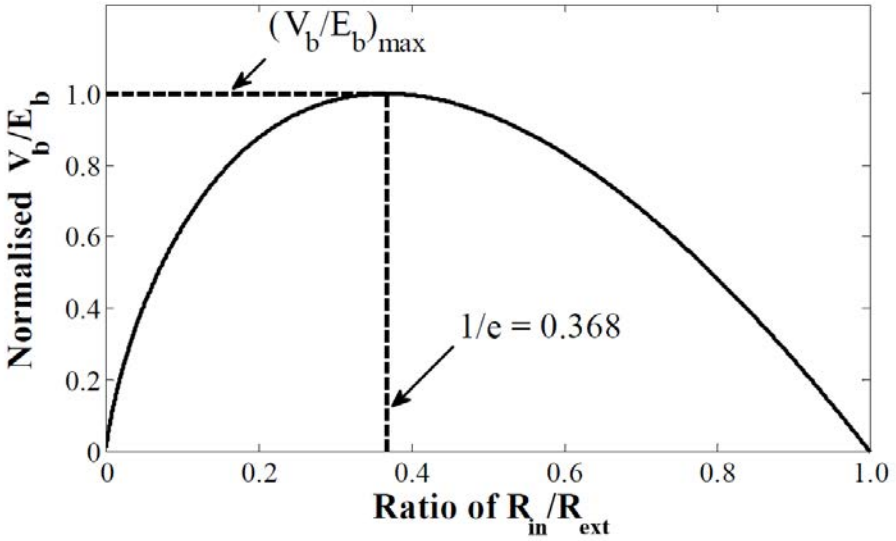

Figure 3.9: Relation between normalized (V_b/E_b) and ratio R_{in}/R_{ext}.

In order to select properly one inner conductor for this project, the choice was made based on the ratio R_{in}/R_{ext}. The main purpose is to be as close as possible to the conditions of existing GIL systems which use the optimal ratio criterion.

Table 3.1 presents the comparison between all the existing inner conductors. It is clear that 30 mm conductor is the one closest to the Nepero constant ($e \approx$2,72) thus, the optimal ratio condition. Therefore, the inner conductor diameter chosen for this project is $\phi = 30$ mm.

Inner conductor diameters [mm]	$\mathbf{R}_{in}/\mathbf{R}_{ext}$
8	11,5
10	9
15	6
20	4,5
30	3

Table 3.1: R_{in}/R_{ext} comparison between the existing inner conductor diameters

Finally, figure 3.10 and figure 3.11 show the coaxial geometry used in this project where the conductor parts are made of aluminium and the insulator parts of polypropylene.

Figure 3.10: 30 mm HV-electrode

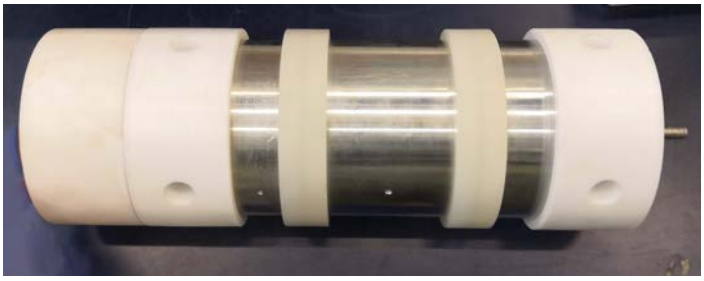

Figure 3.11: Coaxial geometry

3.3.2 Geometry dimensions

Using the same solidworks pattern as [9], in figure 3.12 are presented the coaxial geometry components with their dimensions.
The components shown are:

(a) HV-electrode;

(b) top insulator;

(c) enclosures;

(d) cross-section view of the fully assembled geometry;

(e) support insulator 1;

(f) support insulator 2;

(g) bottom insulator.

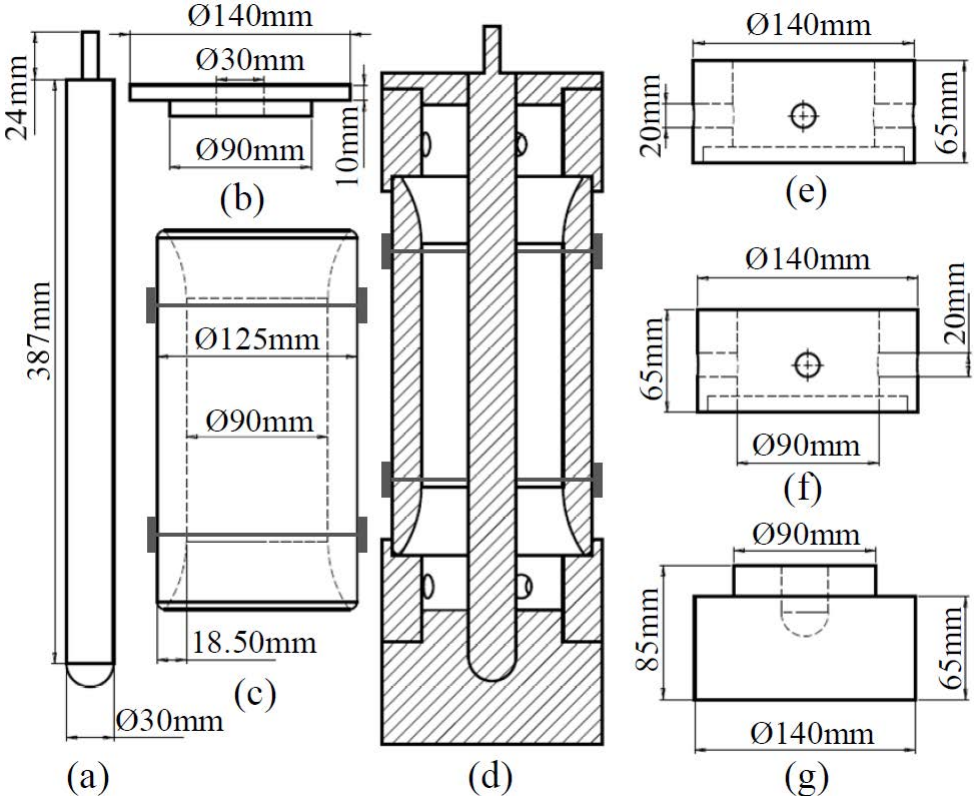

Figure 3.12: Coaxial geometry dimensions

Particular attentions has to be given to the enclosures. In this particular geometry there are three enclosures which are shown by figure 3.13 and figure 3.14.
As can be seen, the external enclosures and the central one are separated by a polypropylene layer with a thickness of 1 mm. Its aim is to insulate the middle enclosure from the other two in order to have the possibility to avoid the electric field distortion that occurs when the internal diameter increase in the external enclosures.

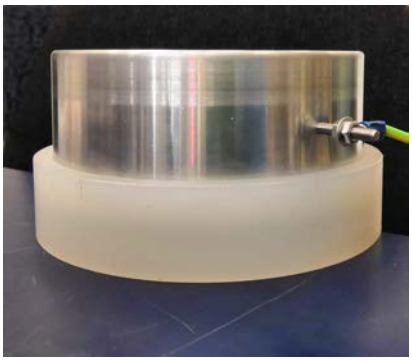

Figure 3.13: External enclosure.

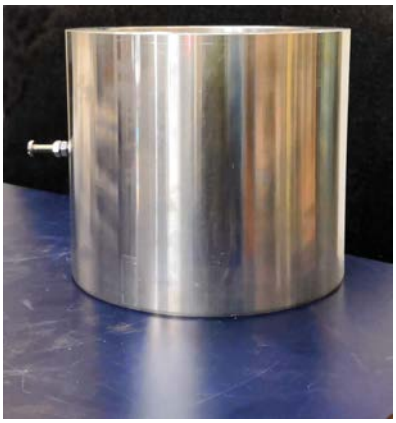

Figure 3.14: Central enclosure.

3.4 Plane-plane geometry

Plane-plane geometry was used at the end of this work to have a better comprehension of the results obtained with the coaxial geometry. The gap chosen was 3 cm in order to replicate the same condition as in the scaled GIL geometry.
The two plane electrodes are made of brass alloy and their surfaces have been polished before being used.

3.4.1 Dimensions

As figure 3.15 presents, the plane diameter is 90 mm and its thickness is 15 mm. The radius of the edge is 2,5 mm and this may create some electric field distortion in clean condition because the gap is quite big if compared with the diameter of the plane.

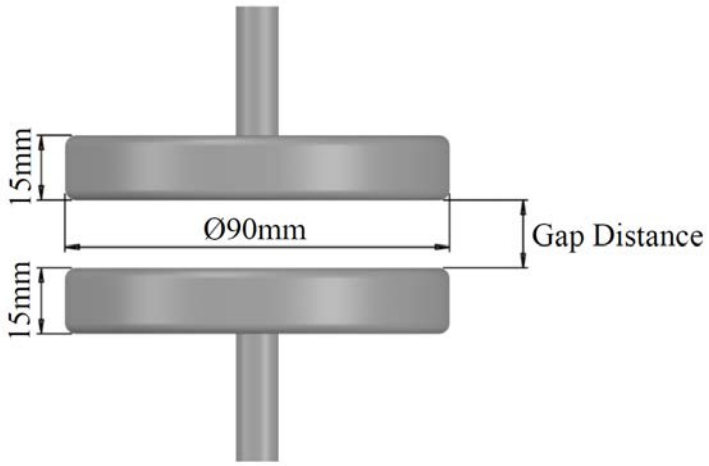

Figure 3.15: Plane-plane dimensions [9].

Chapter 4

Electrostatic model

4.1 Introduction

In chapter 4 will be presented the simulation model done with a commercial Finite Element Method (FEM) solver, COMSOL Multiphysics 5.3a. The purpose of the simulation models in this work is to perform an electrostatic study in order to know the electric field distribution along the geometry and thus, quantify the stress on the insulating medium.
The main steps during a FEM study are:

1. MODEL BUILDING;
2. MODEL MESHING;
3. MODEL STUDYING;
4. ANALYSIS OF THE RESULTS.

During the model building phase, the geometrical structure can be built with the internal model builder or can be imported from other programs, such as Solidworks or AutoCAD. Properties and materials are assigned to domains and finally, boundary conditions have to be specified in the geometry. The model meshing step is the most important one because is essential to find a good trade-off between simulation time and quality of the results. This can be achieved doing a mesh optimization. In the third step, the study type (stationary, time-dependent, etc.) has to be chosen and then, the program runs and starts to solve differential equation per each finite element. The last step of a simulation procedure is the analysis of the result, where it is

possible to generate 1D plot, 2D plot or 3D plot or to export them to others software (e.g. Matlab).

4.2 Coaxial geometry model

In this section will be presented the 3D COMSOL model of the reduced scale coaxial GIL. An electrostatic analysis will be carry out in order to characterize the electric field distribution when high voltage is applied to the inner conductor of the coaxial geometry. The purpose is to predict where is located E_{max} and to evaluate the electric field on the inner electrode surface in correspondence of the middle enclosure. In conclusion, this section will explain all the informations needed to understand and reproduce the simulation model.

4.2.1 Geometry

In the 3D model, there will be represented all the components that are under high voltage environment, such as vessel, bushing, geometry and gas volume. Using the dimensions presented in the previous chapter, the geometrical structures have been draw in COMSOL Multiphysics with the internal builder. In figure 4.1 and figure 4.2 are shown half-section views which present all the model components:

1. HV-electrode;
2. top insulator;
3. support insulators;
4. 1^{st} enclosure;
5. 2^{nd} enclosure;
6. 3^{rd} enclosure;
7. bottom insulator;
8. bushing;
9. pressure vessel;
10. gas volume.

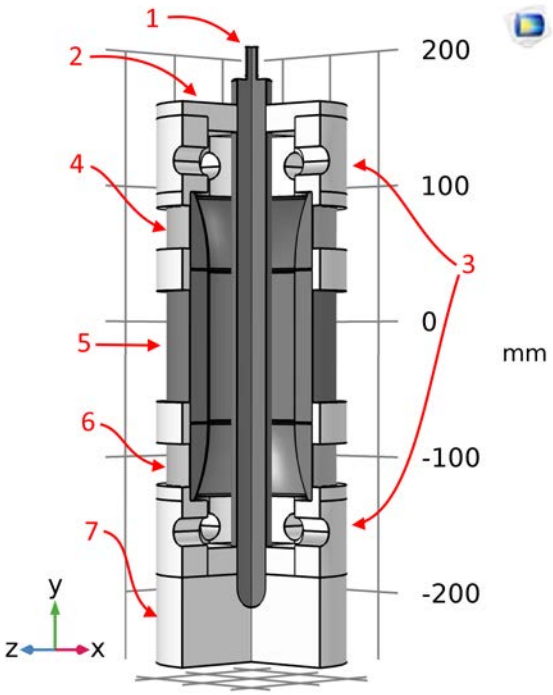

Figure 4.1: Half section of coaxial geometry model.

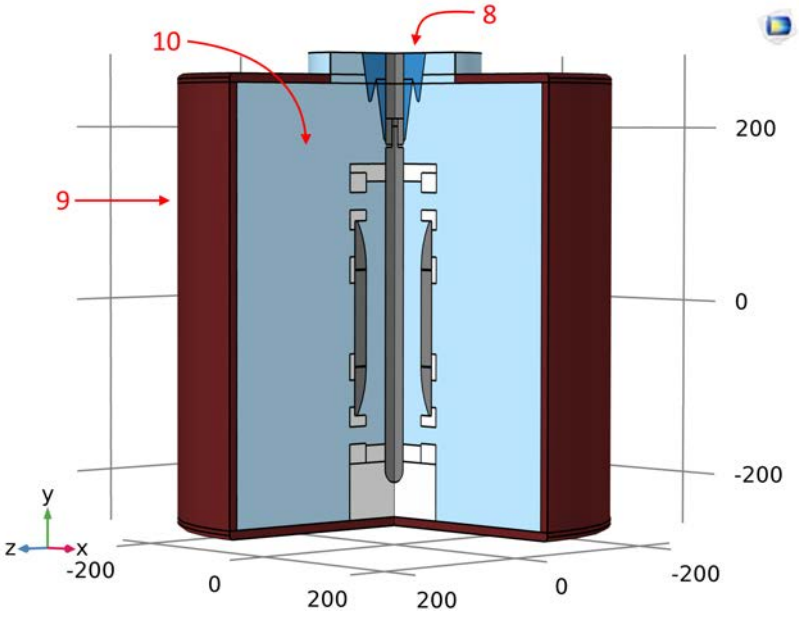

Figure 4.2: Half section of the complete model.

Then, since the vessel, the coaxial geometry and the bushing present in the model are symmetrical, it was decided to simplify the model by considering just one half of it. In this way, it was possible to save simulation time maintaining a high reliability of the results.

4.2.2 Materials

The next step in the model building is to define the materials for each domain. Conductors domains (such as pressure vessel, coaxial geometry electrodes and the bushing inner conductor) have been deleted from the model. The reason is basically that, in electrostatic conditions, free charges in a conductor reside only on the outer surfaces. The inner domain has a constant electric field equal to zero due to the sum of the external and the internal electric fields so, finally, it is not worthwhile to mesh and to solve the conductor domains.
Furthermore, for this type of study it is necessary to define in the material properties also its relative permittivity ϵ_r. The polypropylene relative permittivity was found in [1], and the silicone rubber ϵ_r in [9]. The relative permittivity of the gas domain was set at 1 because, except in high pressure conditions, the density of atoms or molecules is way smaller than liquids or solids [24]. Table 4.1 shows the materials and its relative permittivity ϵ_r assigned to the correspondent components.

Components	**Materials**	**Relative permittivity ϵ_r**
Polypropylene	2,2	Insulators
Silicone rubber	3,1	Bushing
Gas	1	Remaining domains

Table 4.1: Material properties assigned in the COMSOL model.

4.2.3 Boundary conditions

The boundary conditions that have to be defined for this model are only two:

- high voltage terminal;
- ground terminal.

During the HV tests, the voltage is applied through the bushing to the inner conductor of the coaxial geometry. Therefore, the high voltage terminal in the COMSOL model is assigned to both the inner conductors of bushing and coaxial geometry boundaries.
In the test setup, the pressure vessel and all the three enclosures are directly connected to the ground system of the lab. Hence, all the enclosures boundaries and all the gas boundaries that touch the pressure vessel are assigned to the ground terminal. Figure 4.3 shows the ground boundaries selected in blue.

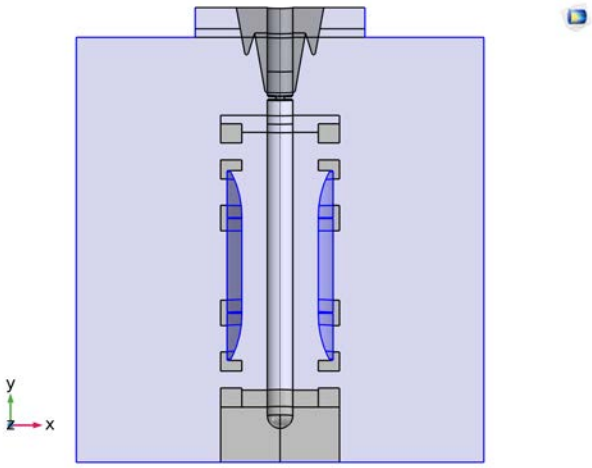

Figure 4.3: Ground boundaries set in the COMSOL model.

4.2.4 Mesh

During the mesh generation, a FEM solver divides the model into small elements of geometrically simple shapes. In the 3D models, the mesh elements are tetrahedrons [11].
In the geometry previously presented there are many small edges, small faces and little curvature radii. Therefore, in order to have an optimal and reliable solution, is very important to set properly the mesh settings near to critical boundaries or in high interest areas.
One solution could be to set an extremely fine mesh in all the model, but is not the one taken here because the model is big and complex thus, the computation would have required too much time and heavy hardware performances.

In this model, mesh optimization is performed. The first reason is to achieve reliable results thanks to a fine mesh near the interesting areas. The second one is to save simulation time by decreasing the mesh quality where is it possible. Thus, the model is divided in four areas with different mesh settings. These regions are:

1. GAS DOMAIN → where the mesh is coarse near the vessel boundaries but it becomes finer as it gets closer to the coaxial geometry. In this way, there is a low quality far from interesting areas (saving simulation time) and a good quality in the gas portion near or inside the geometry subject of study.

2. HV ELECTRODE BOUNDARY → where a high quality mesh has been set in order to obtain the most reliable results possible in the conductor surface.

3. BOTTOM INSULATOR → where a good quality mesh is set because is necessary to focus the region where is present the tip of the inner electrode.

4. REMAINING DOMAINS (bushing, other insulators) → where is not required high definition of the results hence, low quality mesh elements are built in order to decrease the computation time.

Figure 4.4 shows the mesh built in all the domains of the model. It is interesting to notice the four different mesh settings regions that allows the model to reach a good trade-off between the quality of the results and the processing time.

Figure 4.5 shows a zoomed view of the HV electrode boundary mesh. From this picture the high mesh quality and hence, the small tetrahedrons elements can be noted.

Figure 4.6 shows the focus view on the bottom insulator mesh. Here is possible to observe that the elements become smaller as they get closer to conductor tip boundary.

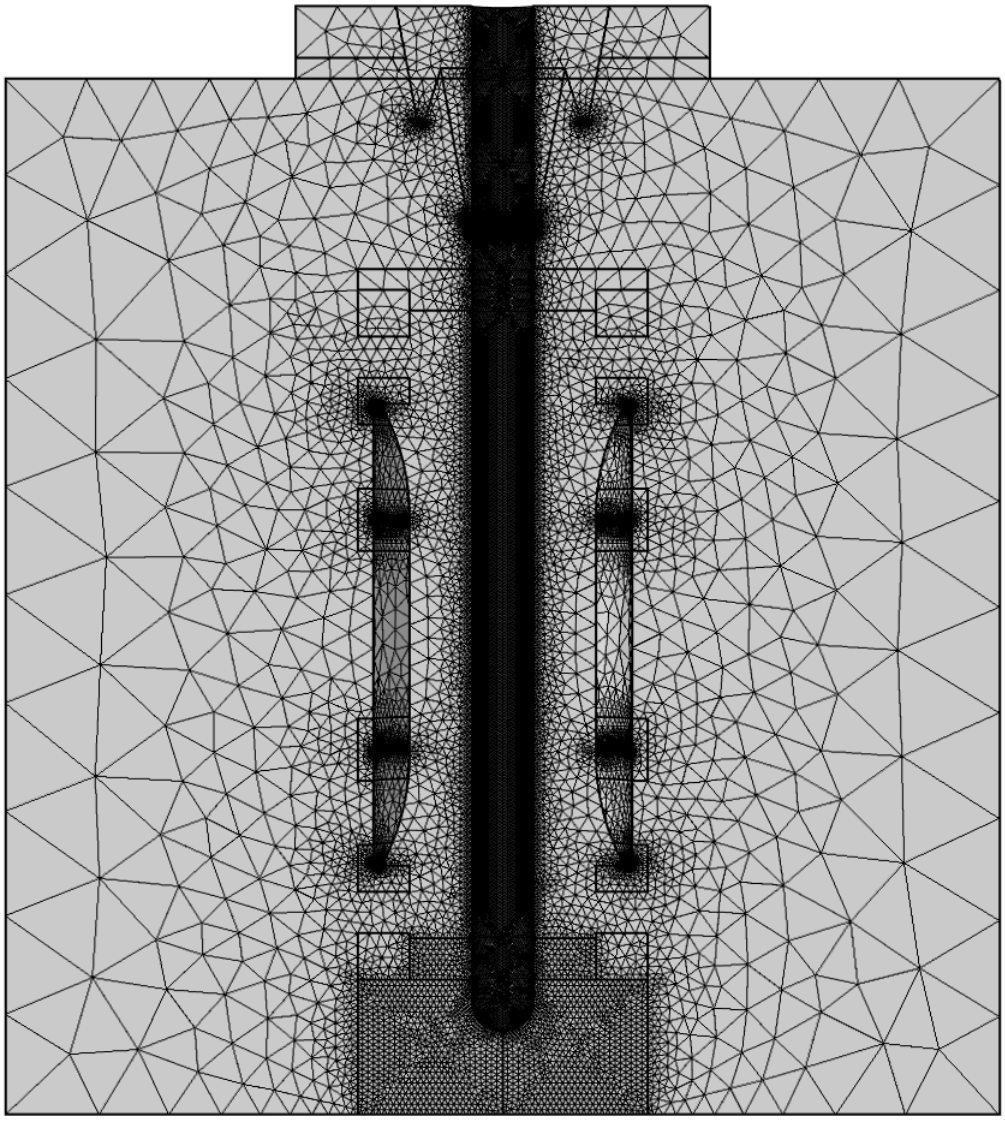

Figure 4.4: Mesh result of the whole COMSOL model.

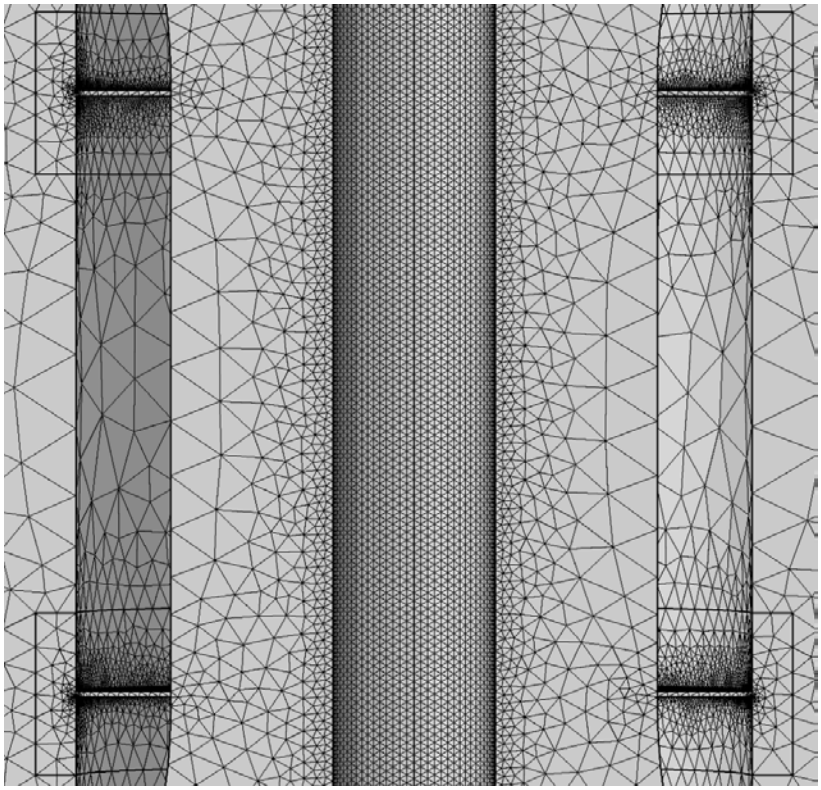

Figure 4.5: Mesh zoomed in the HV electrode region.

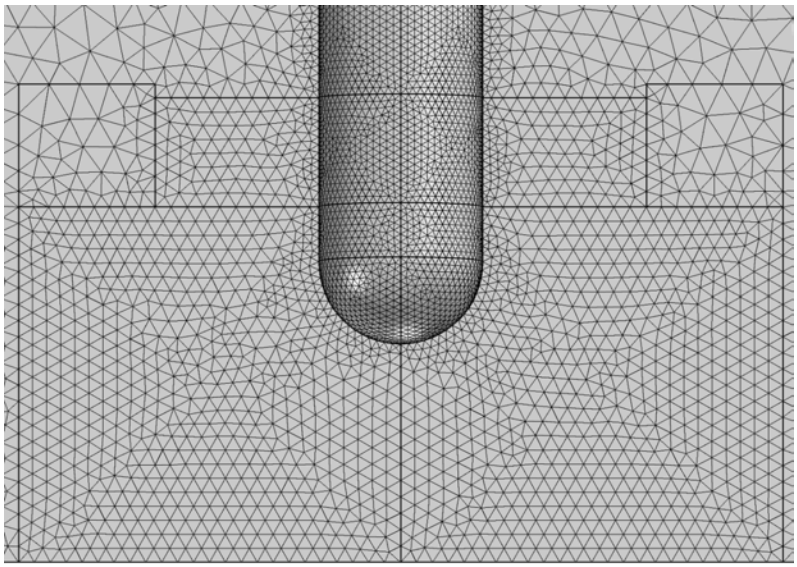

Figure 4.6: Mesh zoomed in the bottom insulator region.

4.2.5 Electrostatic analysis results

The model simulation is performed with the AC/DC module of COMSOL Multiphysics. Since this work is focused on AC discharge, the study type chosen for the simulation is the frequency domain at 50 Hz.
The electrostatic analysis is carried out by assigning to the high voltage terminal 1 kV peak value. This means that the results obtained are referred to that value but, since E and V are proportionally related, it is sufficient to multiply the results obtained at 1 kV for the new voltage value in order to evaluate the electric field under those conditions.
The results of the simulation are presented below.

Figure 4.7 shows the electric potential of the model when 1 kV is applied to the HV electrode.

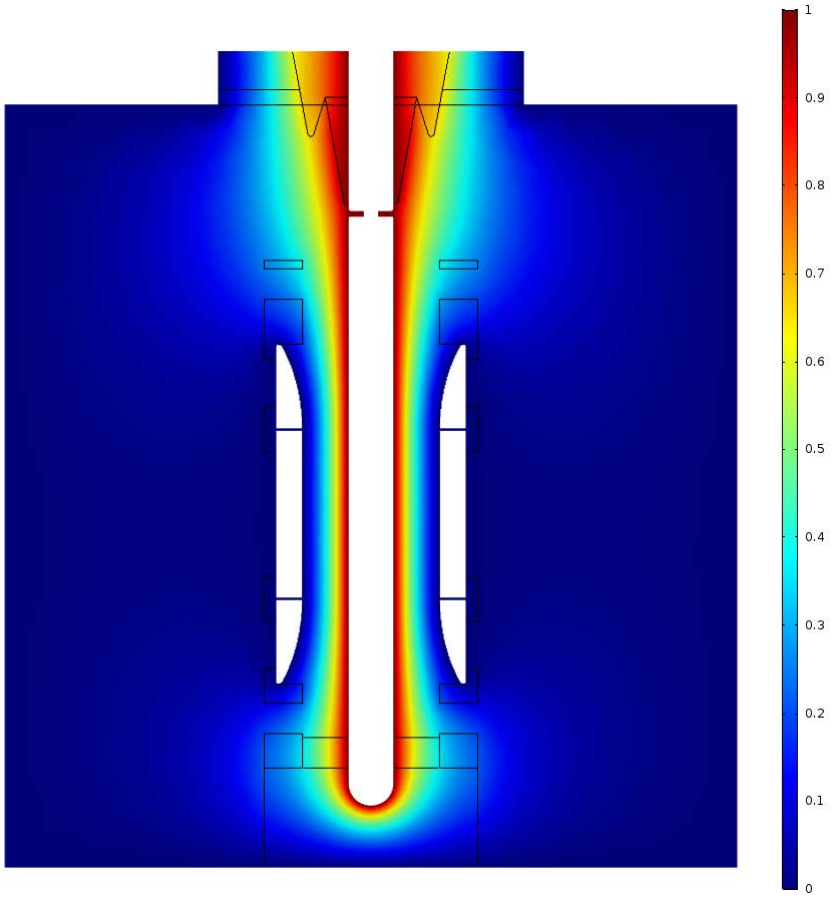

Figure 4.7: Electric potential at 1 kV.

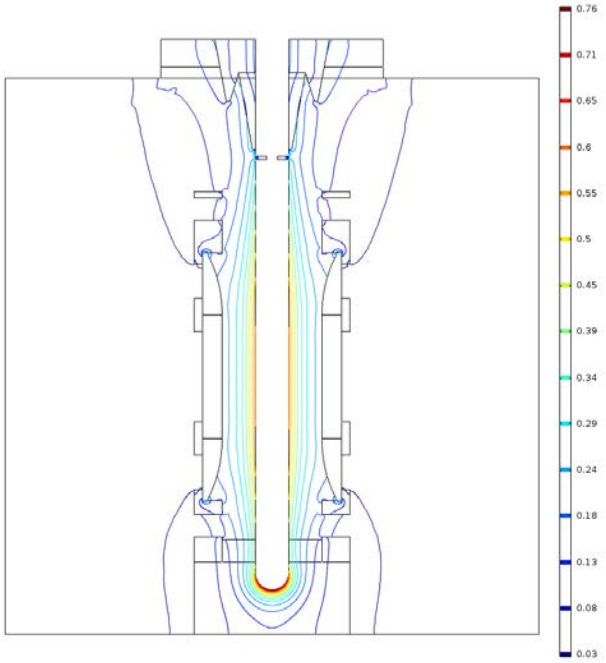

Figure 4.8: Electric field lines with equal magnitudes (kV/cm).

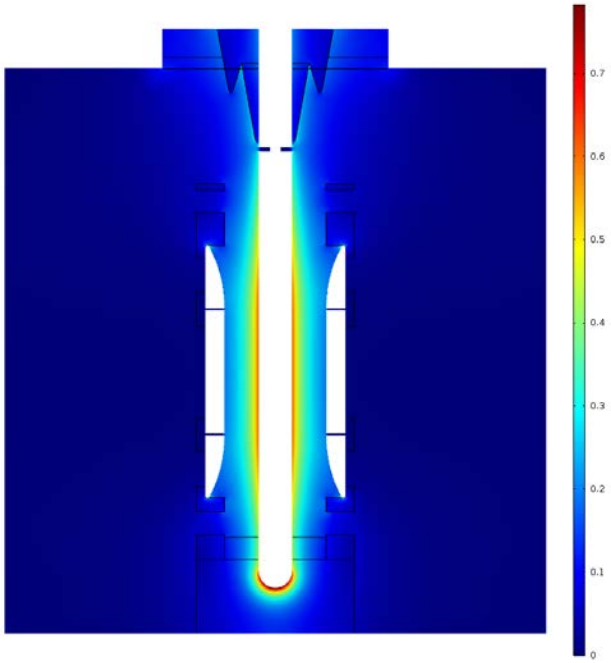

Figure 4.9: Electric field distribution (kV/cm).

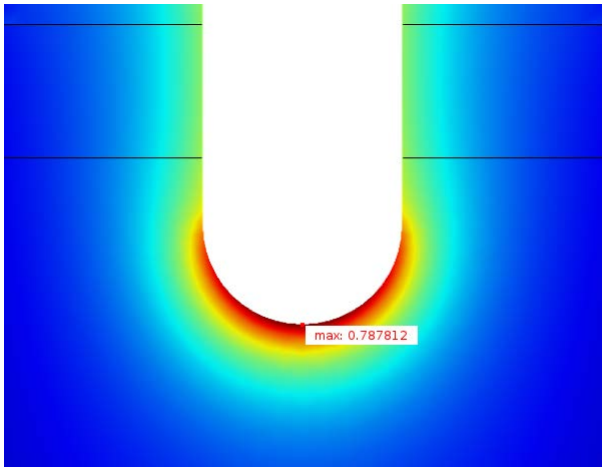

Figure 4.10: Zoom on the maximum of the electric field (kV/cm).

Figure 4.8 shows the electric field distribution using lines with equal magnitudes.
Figure 4.9 presents again the electric field distribution, but the electric field norm variation is shown gradually.
From both the figures, as expected, the electric field is high on the inner electrode surface. Considering the HV electrode, the tip and the surface in correspondence of the middle enclosure are the points where E is higher.

Figure 4.10 shows that the maximum value of the electric field is located on the inner electrode tip.
This result shows that the design of the model is not ideal because E_{max} is not localized in the region of interest for this project. A solution could be to use a thicker bottom insulator in order to obtain the E_{max} point in the center of the reduced scale GIL.

Nevertheless, considering that:

1. polypropylene does not have problems with the AC voltage limits present in this work;

2. the signal is collected just form the enclosure in the middle;

is possible to investigate what happen in the center of the reduced scale GIL when high voltage is applied.

Thus, the electric field along the HV conductor surface is calculated with COMSOL Multiphysics. Precisely, the length considered starts from the end of the top insulator to the beginning of the bottom one, neglecting the end of the electrode (as show in figure 4.11).

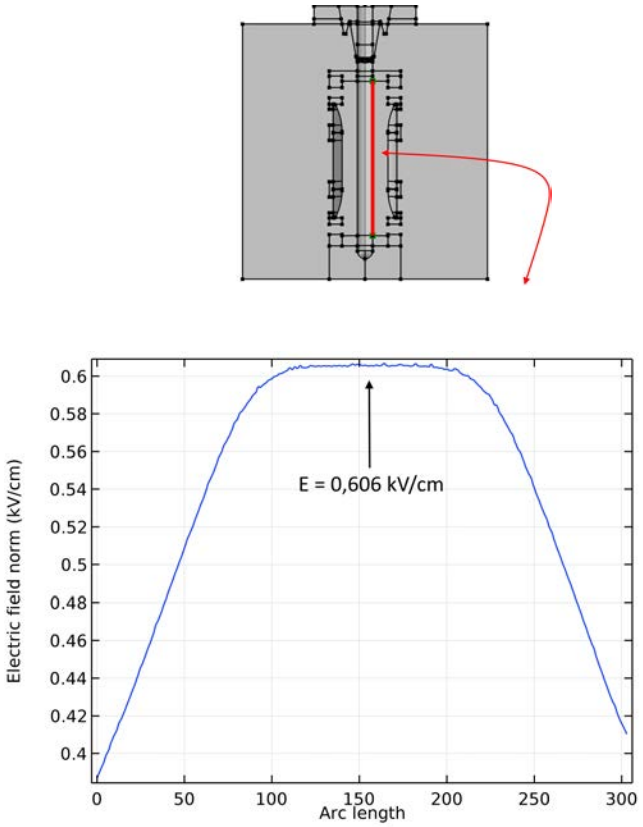

Figure 4.11: Electric field norm along the conductor surface.

E_{max} for coaxial cylinders can be calculated also in a theoretical way [31]. Applying the dimensions of the reduced scale GIL to the formula:

$$E_{max} = \frac{V}{R_{int} \cdot \ln(\frac{R_{ext}}{R_{int}})} = \frac{1}{15 \cdot \ln(\frac{45}{15})} = 0,607 \ \frac{kV}{cm}$$

Finally, it can be seen by comparing the results of E_{max} obtained with the COMSOL model and with the theoretical formula that they match very well.

Furthermore, using the E_{max} obtained from the model, it is interesting to evaluate the field utilization factor of the zone of interest in this work thus, the geometry formed by the HV electrode and the central enclosure.
Applying the definition:

$$\eta = \frac{E_{mean}}{E_{max}} = \frac{V}{d \cdot E_{max}} = \frac{1}{3 \cdot 0,607} = 0,55$$

it possible to notice that the electric field in the reduced scale GIL is non-uniform.

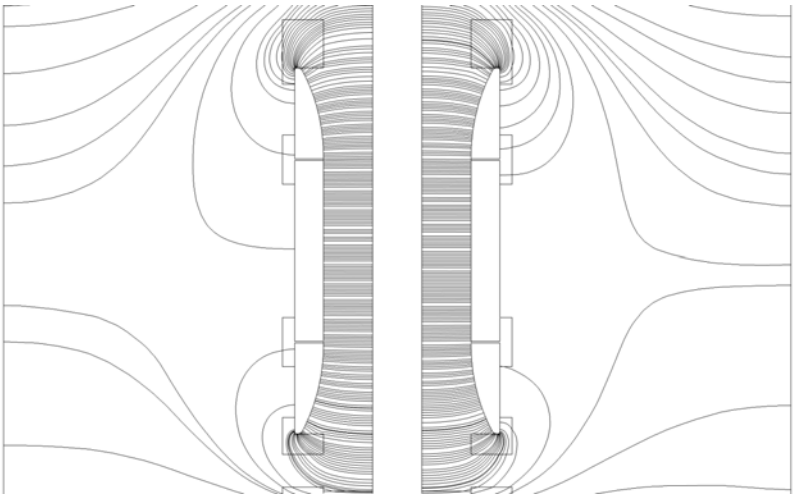

Figure 4.12: Electric field lines in the coaxial geometry.

In conclusion, it can be easily seen from figure 4.12 the main reason which led to the construction of three enclosures. The electric field lines in the middle are perfectly orthogonal to the electrodes, instead, where the inner diameter increases in the other two enclosures, they become more curved. Therefore, since the coaxial geometry subject of study in this work aims to reproduce the same condition of a GIL, the middle enclosure has been insulated from the other two.

Chapter 5

Capacitance evaluation

5.1 Introduction

In chapter 5 will be presented the central capacitance evaluation comparing different results obtained with:

- theoretical formula;
- the COMSOL model;
- the experimental evaluation.

This will be useful in order to recognise the reliability of the model built with COMSOL. The capacitance meant is the one between the high-voltage electrode and the central enclosure of the coaxial geometry, as is shown in figure 5.1.

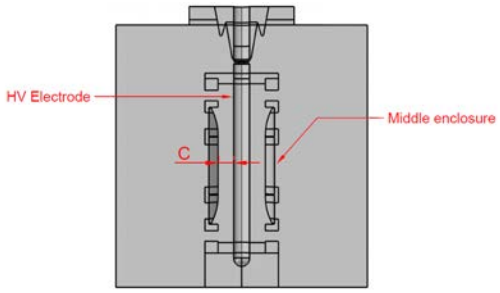

Figure 5.1: Capacitance C in the model.

5.2 Theoretical evaluation

C is basically the capacitance between two concentric cylinders, whose essential dimensions are shown in the figure below.

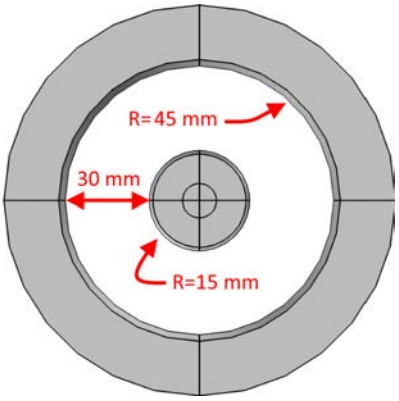

(a) Top view.

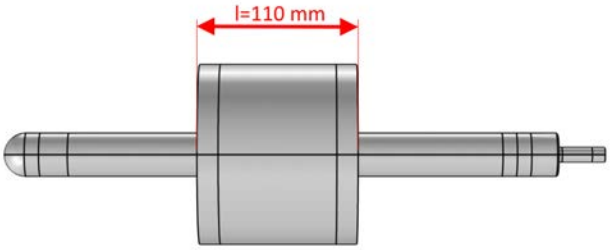

(b) Side view.

Figure 5.2: Capacitance geometry views.

Assuming $\varepsilon_r = 1$ for the insulating gas, that is true in the range of pressures we are interested in [24], it is possible to use the well known formula:

$$C = \frac{2\,\pi\,\varepsilon\,l}{ln(\,\frac{R_{ext}}{R_{int}})} \quad . \tag{5.1}$$

Applying the dimensions of the coaxial geometry in the formula above the capacitance founded is:

$$C \;=\; \frac{2\,\pi\,\varepsilon_0\,0,110}{ln\,(\,\frac{45}{15}\,)} \;\approx\; 5,57\,pF$$

5.3 COMSOL evaluation

The capacitance is evaluated in COMSOL Multiphysics by assigning two terminals, one to the HV electrode and the other one to the enclosure in the center. The ground is set to the others two enclosures and in all the gas boundaries that touch the vessel.

Considering the capacitances in the model, it is possible to evaluate from the Maxwell capacitance matrix:

$$\begin{bmatrix} Q_1 \\ Q_2 \end{bmatrix} = \begin{bmatrix} C_{11} & C_{12} \\ C_{21} & C_{22} \end{bmatrix} \begin{bmatrix} V_1 \\ V_2 \end{bmatrix}$$

the mutual capacitance matrix, that is:

$$\begin{bmatrix} C_{m,11} & C_{m,12} \\ C_{m,21} & C_{m,22} \end{bmatrix} = \begin{bmatrix} C_{11} + C_{12} & -C_{12} \\ -C_{21} & C_{22} + C_{21} \end{bmatrix}$$

Thus, using this conditions during a stationary study, the mutual capacitance matrix of the whole model has been evaluated.
The results are:

$$\begin{bmatrix} C_{m,11} & C_{m,12} \\ C_{m,21} & C_{m,22} \end{bmatrix} = \begin{bmatrix} 263,98 & 5,8314 \\ 5,8298 & 17,972 \end{bmatrix}$$

The capacitance between the HV conductor and the middle enclosure would be $C_{m,12}$ or $C_{m,21}$ indifferently. It can be seen that the mutual capacitances $C_{m,12}$ and $C_{m,21}$ are not exactly the same but in theory they should be.
This little difference between them is due to the fact that the simulation is built with finite mesh elements, so small dissimilarity can be accepted.

In conclusion, the capacitance C evaluated with the model is:

$$C = \frac{C_{m,12} + C_{m,21}}{2} = 5,8306\, pF$$

5.4 Experimental evaluation

5.4.1 Test setup

The principle used to evaluate the capacitance in the test cage is very simple. Basically, the AC high voltage is applied between the two electrodes in the coaxial geometry and the capacitance C is calculated from the capacitive current that flows through the gap. It is important to note that during the test, the two external enclosures were directly grounded and from the central one the current signal has been measured. The equivalent scheme to represent the circuit is:

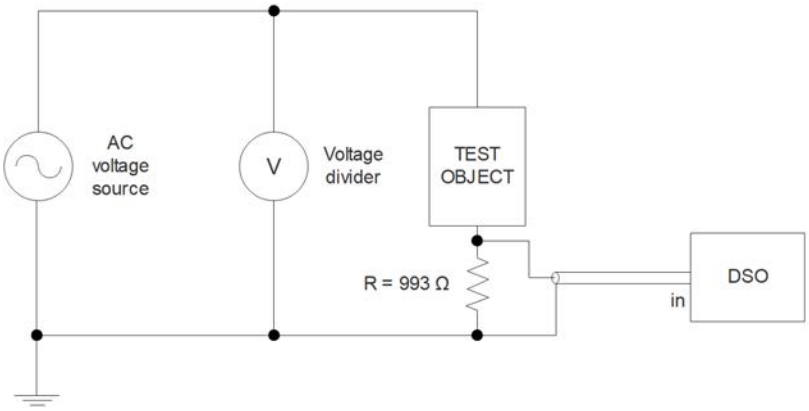

Figure 5.3: Equivalent circuit of the capacitance test.

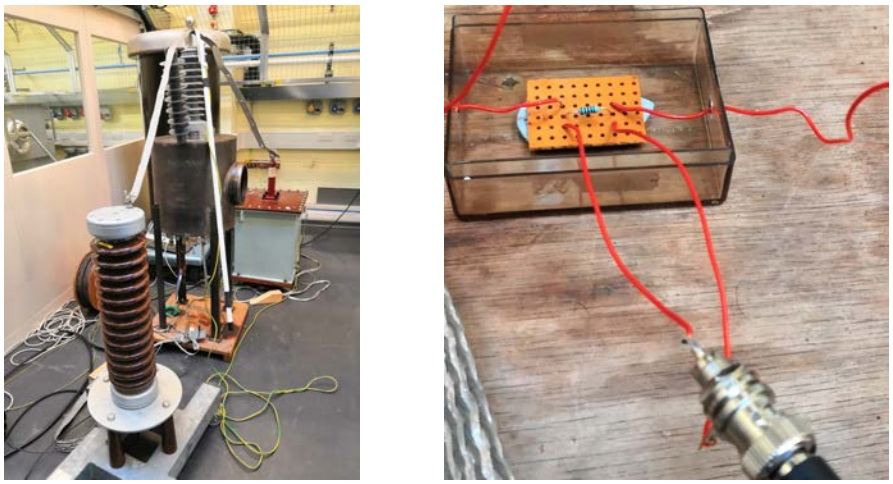

(a) Test arrangement.

(b) 993 Ω resistor.

Figure 5.4: Capacitive test setup in the laboratory.

The capacitive current is very small (some μA) therefore, in order to be able to see properly the current signal in the oscilloscope, a 993 Ω resistance was chosen to amplify it. The first measure that the oscilloscope presented was:

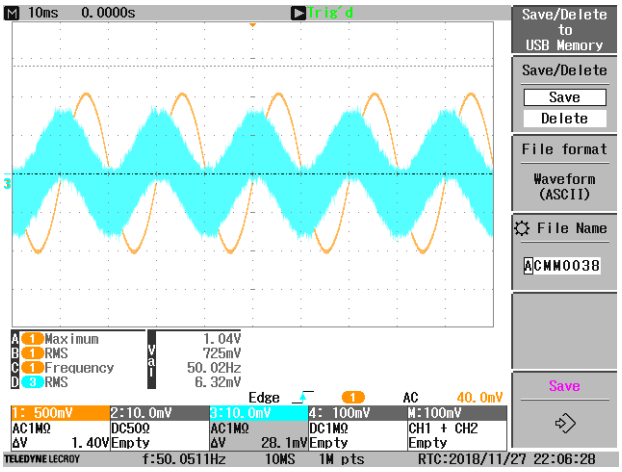

Figure 5.5: Oscilloscope initial conditions.

From figure 5.5 is possible to see that the voltage on the resistance V_R (light blue) is not clear and the are a lot of harmonics superimposed on the fundamental. Therefore, in order to get a clearer measure of the voltage across the resistance, hence of the current, it was necessary to add a low pass filter with a cut-off frequency of 200 kHz to clean the V_R signal.

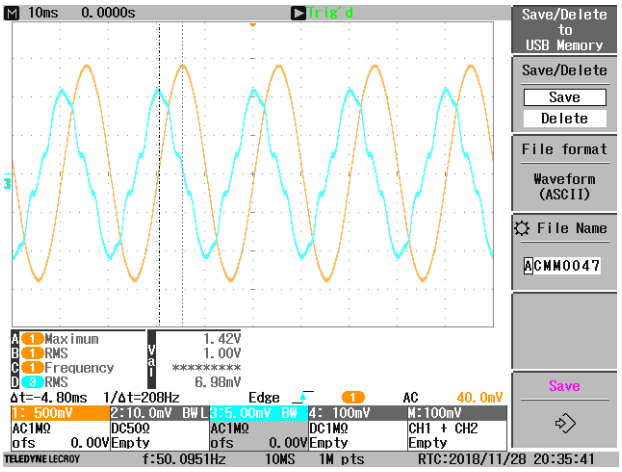

Figure 5.6: Oscilloscope filtered output.

Figure 5.6 shows, in addition, that the delay between the waves is ≈ 4,8 ms, which means that the current is prevalent capacitive.

5.4.2 Test results

The measurements carried out in the conditions illustrated above are five at different voltage values. The data of the measurements have been evaluated with MATLAB and the RMS results presented in the legend of each plot are:

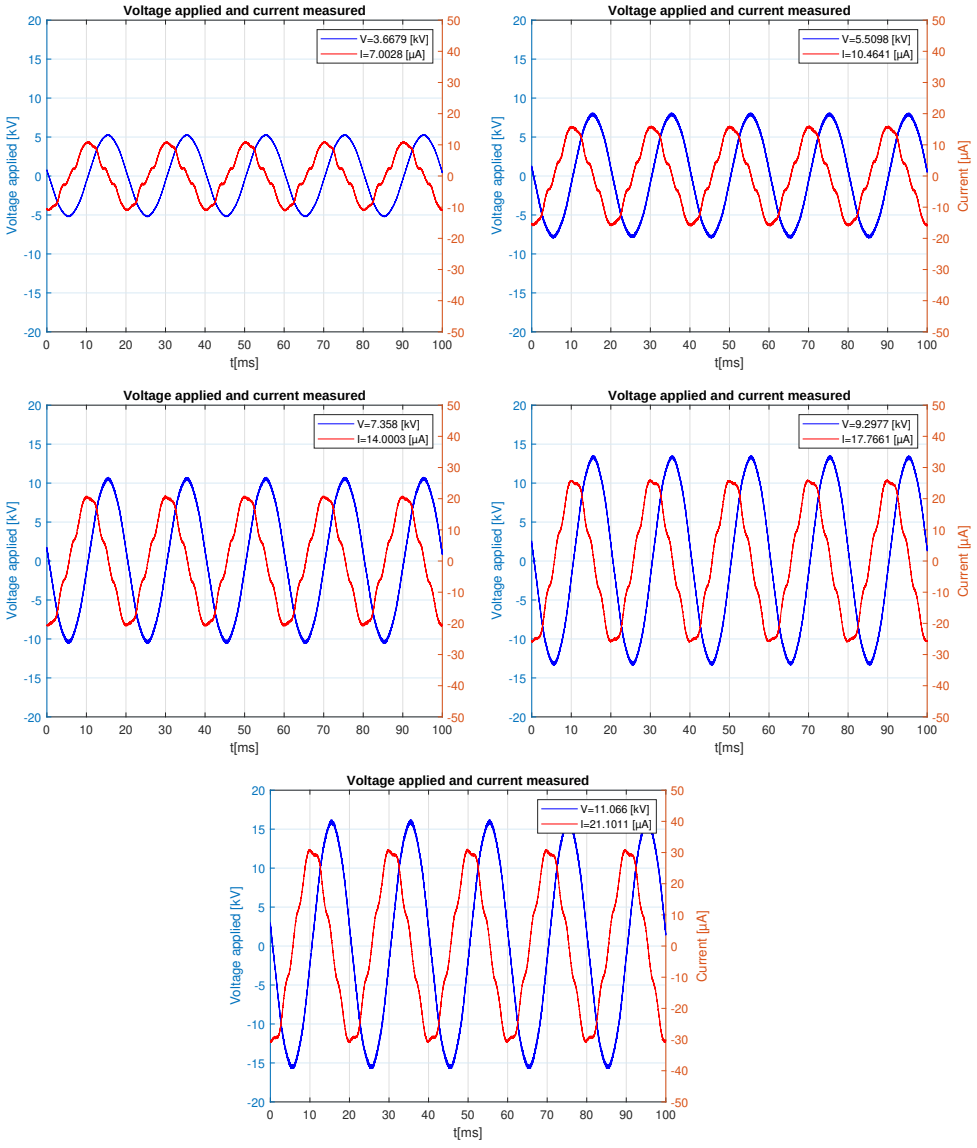

Figure 5.7: Measurements results.

The capacitances resulted from these five measures are:

$$C_1 = 6.0772\,pF$$

$$C_2 = 6.0453\,pF$$

$$C_3 = 6.0566\,pF$$

$$C_4 = 6.0823\,pF$$

$$C_5 = 6.0697\,pF$$

Thus, considering the mean between all of these results, the capacitance is:

$$C_{mean} = 6.0662\,pF \qquad standard\,deviation = 1,52\%$$

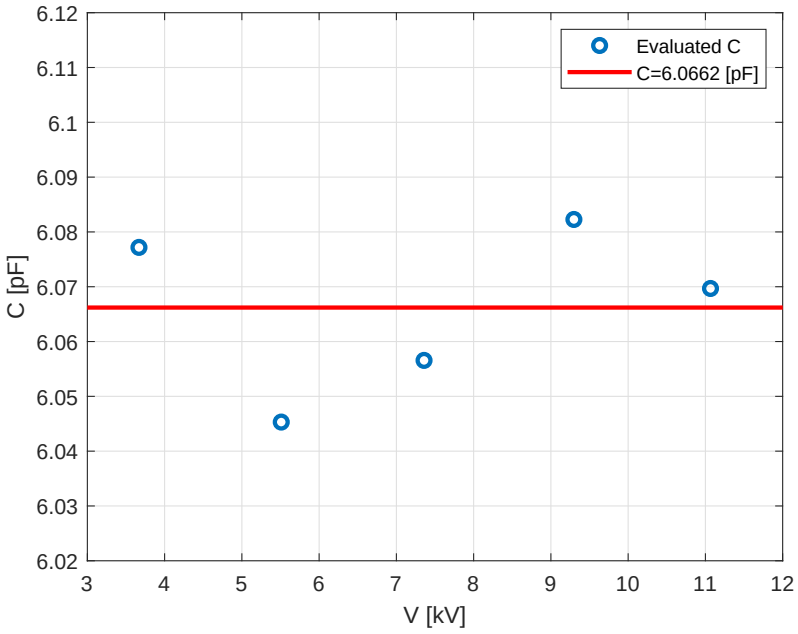

Figure 5.8: Capacitance test results.

5.5 Conclusion

The capacitance C has been evaluated in three different ways and it is clear that all the values found are close together. Figure 5.9 shows that the result obtained with the model is in the middle between the formula value and the tested one. Furthermore, taking as reference the theoretical formula, it is interesting to note that the COMSOL model result presents a difference of 4,67% and the experimental result of 8,91%.
In conclusion, this capacitance evaluation confirm that the model built with COMSOL Multiphysics is reliable.

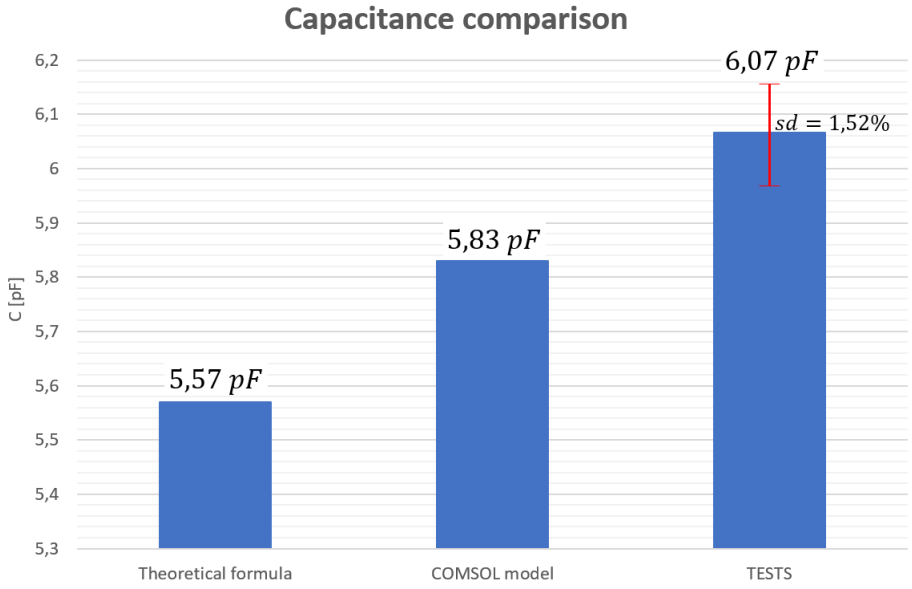

Figure 5.9: Capacitance results comparison.

Chapter 6

Breakdown tests with the coaxial geometry

6.1 Introduction

The aim of this chapter is to characterise the breakdown voltage behaviour of the reduced scale GIL. The coaxial geometry subject of study in this work has an electric field arrangement similar to that of a GIL system. Therefore, the results obtained in this chapter are representative for a possible future use of CF_3I/CO_2 mixture in gas insulated lines.
In this chapter, the breakdown voltage tests results with air and CF_3I/CO_2 (30%/70%) mixture will be presented. Furthermore, the effect of asperities attached on the HV electrode with either air or CF_3I/CO_2 mixture will be discussed below.
It is very interesting and important to understand how unwanted particles affect the breakdown voltage of a coaxial geometry, because having impurities in a GIL is one of the worst problems that can happen.
Normally, GIL are assembled in particular clean rooms in order to avoid the possibility to have impurities inside them. However, asperities can come also form the gas insulating medium when conductive by-products starts to appear.
Thus, for these reasons is important to understand how the coaxial geometry performs under AC high voltage environment and in presence of asperities.

6.2 Test setup

The breakdown voltage measurements basically consist in applying high voltage to the test object for a determined number of time. When the sparkover occurs between the electrodes in the geometry, the voltage value is recorded. Repeating this procedure for n times, it is possible to calculate the breakdown voltage mean and its standard deviation.
The equivalent circuit of the test equipment used in this project during breakdown voltage measurements is shown below:

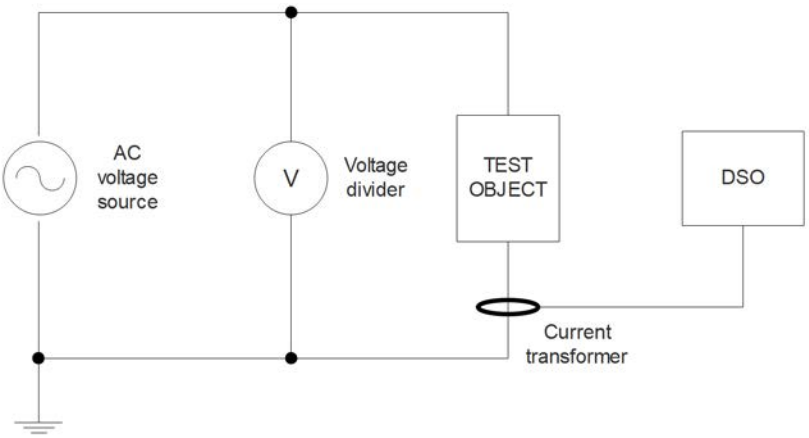

Figure 6.1: Equivalent circuit of breakdown voltage test.

The AC voltage source (step-up transformer) and the voltage divider were previously presented in section 3.2. The test object consists of the coaxial geometry which was placed inside the pressure vessel. The inner electrode was connected to the HV transformer output through the bushing. Each enclosure was directly grounded and from the central one the current signal was collected. The device chosen for the current measurement is a current transformer (CT) and the main reasons are:

1. CT can measure high currents providing an electrical insulation which is very important under high voltage environment;

2. the sparkover current is quite high thus, there is no need to amplify it with a resistor.

Figure 6.2 shows the CT used in the measurements and its output ratio 1:10 V/A.

Figure 6.2: Current transformer characteristics.

In conclusion, the current and voltage during the breakdown were recorded with an oscilloscope. The DSO used in these measurements was a Lecroy WaveJet Touch 354 with a bandwith of 500 MHz, 5 Mpts memory and a maximum sample rate of 2 GS/s.

6.3 Metal protrusions

Two custom-made metal protrusions were created in the Cardiff University HV laboratory. They are made with copper tape, solder and aluminium wire. Basically, a small piece of wire was cut and soldered above the copper tape, which provides the electrical continuity. In this way, the defects created were easily attachable to the HV electrode of the coaxial geometry.
Figure 6.3 shows the height of the two protrusions, instead figure 6.4 shows their diameters. These measurements have been evaluated with the optical microscope (Zeiss Axio Imager M2m) in Morgan-Botti lightning laboratory of Cardiff University.

(a) Small.

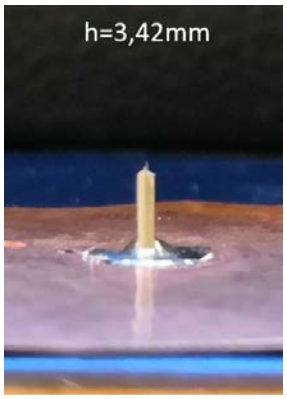

(b) Big.

Figure 6.3: Heights of the particles.

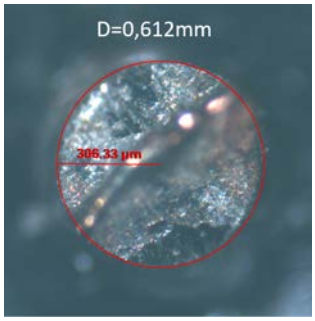

(a) Small.

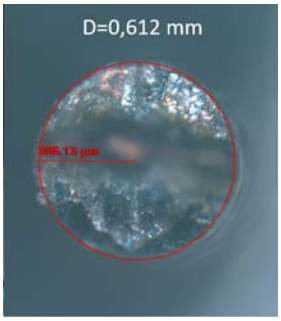

(b) Big.

Figure 6.4: Diameters of the particles.

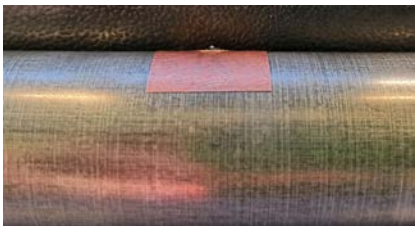

(a) Small.

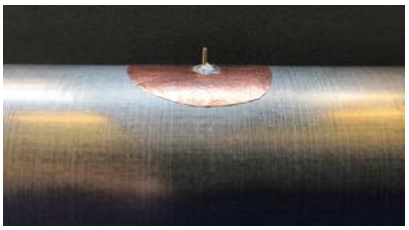

(b) Big.

Figure 6.5: Particles applied to the HV electrode.

6.4 Test procedure

The test procedure, in order to evaluate the breakdown voltage of the coaxial geometry, will be explained in this section. According to the BS EN 60060-1 [19], the voltage was increased around 2% of V per second, where with V it is intended as the final voltage of the test. This voltage slope, as explained in the standards, is a trade-off between:

- a slow rise to allow reading of the measuring system;
- a quick rise to not stress unnecessarily the test object.

In these tests, the RMS of last AC cycles recorded before the instant of the sparkover is the breakdown voltage. Figure 6.6 shows an example of a BV measure post-processed with Matlab in order to evaluate properly the RMS of the AC cycles.
The same procedure is repeated 15 times in order to have a set of measured voltages where it is possible to evaluate the mean with its standard deviation. Furthermore, it is important to note that between two consequent tests, two

minutes were waited to let the charges and the stress on the gas insulation medium return as at the initial condition thus, to not have influence between two close measures.
In conclusion, the tests were carried out with air at atmospheric pressure and with CF_3I/CO_2 (30%/70%) mixture at 0,1 MPa (abs).

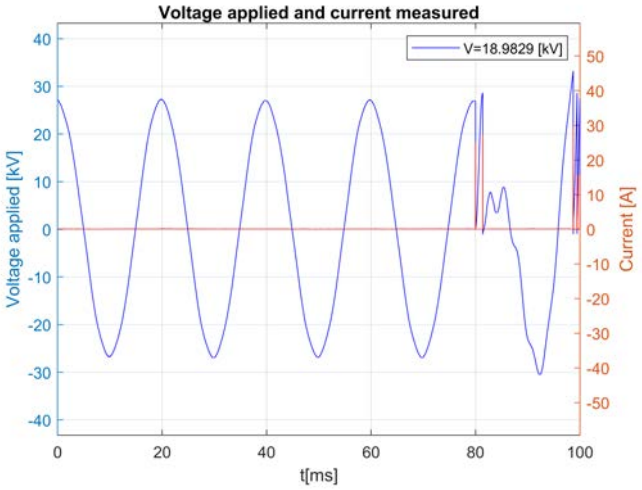

Figure 6.6: Example of a breakdown voltage measure obtained with the big asperity attached on the HV electrode in the coaxial geometry.

6.5 Atmospheric corrections

The breakdown voltage tests carried out in the Cardiff University HV laboratory were conducted under slightly different atmospheric conditions than the standard one. Therefore, in order to refer the V_b to the standard reference atmospheric conditions, the respective correction factors have been applied.

As reported in BS EN 60060-1 [19], the standard reference atmosphere is:

- $t_0 = 20$ °C;
- $p_0 = 1013$ hPa (1013 mbar);
- $h_0 = 11$ g/m^3.

It is well known that breakdown voltage V_b depends on the atmospheric conditions, as an example it is usually increased by an increase in either air

density or humidity. Nevertheless, when the relative humidity exceeds 80% the breakdown voltage becomes irregular.

The breakdown voltage is proportional to the atmospheric correction factor K_t:

$$K_t = k_1 \cdot k_2 \tag{6.1}$$

where k_1 is the air density correction factor and k_2 is the humidity correction factor.
Hence, the breakdown voltageV_b measured at different test conditions (p, t, h) can be referred to V_{b0} which would have been obtained under the standard reference atmospheric conditions (p_0, t_0, h_0) with:

$$V_{b0} = \frac{V_b}{K_t} \tag{6.2}$$

6.5.1 Air density correction factor k_1

The air density correction factor k_1 depends on the relative air density δ and can be generally expressed as:

$$k_1 = \delta^m \tag{6.3}$$

where m is an exponent treated in subsection 6.5.3.
Expressing t and t_0 in degrees Celsius and the atmospheric pressures p and p_0 with the same unit, the relative air density is:

$$\delta = \frac{p}{p_0} \cdot \frac{273 + t_0}{273 + t} \tag{6.4}$$

The above correction is considered reliable for $0{,}8 < k_1 < 1{,}05$.

6.5.2 Humidity correction factor k_2

The humidity correction factor k_2 is:

$$k_2 = k^w \tag{6.5}$$

where w is an exponent treated in subsection 6.5.3 and k is a parameter that depends on the type of test voltage (DC, AC or impulse) and it is a function of absolute humidity h and relative air density δ.

For AC test voltage the expression is:

$$k = 1 + 0,012(\frac{h}{\delta} - 11) \qquad \text{for } 1 \text{ g/m}^3 < h/\delta < 15 \text{ g/m}^3 \tag{6.6}$$

where the absolute humidity in g/m^3 can be calculated knowing the ambient temperature t and the relative humidity in percent k with the formula below:

$$h = \frac{6,11 \cdot R \cdot e^{\frac{17,6 \cdot t}{243+t}}}{0,4615 \cdot (273 + t)} \tag{6.7}$$

6.5.3 Exponents m and w

As the correction factors k_1 and k_2 depend on the type of pre-discharges, with the formula below this fact is taken into account.

$$g = \frac{U_{50}}{500 \cdot L \cdot \delta \cdot k} \tag{6.8}$$

where:

- U_{50} is the 50% disruptive-discharge voltage peak value at the actual atmospheric conditions [kV];
- L is the minimum discharge path [m];
- δ is the relative air density;
- k is the parameter defined with equation (6.6).

Figure 6.7 and figure 6.8 show as the exponents vary with the parameter g. In table 6.1 are shown the formulas used to calculate m and w in correspondence of the g value.

g	***m***	***w***
< 0.2	0	0
0.2 to 1.0	$g(g-0.2)/0.8$	$g(g-0.2)/0.8$
1.0 to 1.2	1.0	1.0
1.2 to 2.0	1.0	$(2.2-g)(2.0-g)/0.8$
> 2.0	1.0	0

Table 6.1: Values of exponents, m for air density correction and m for humidity correction, as a function of the parameter g [19].

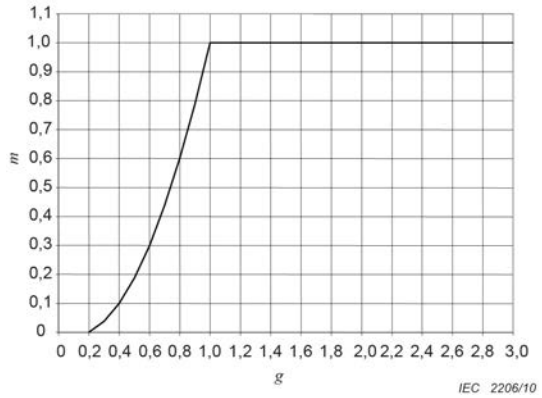

Figure 6.7: Exponent m for air density correction function of g [19].

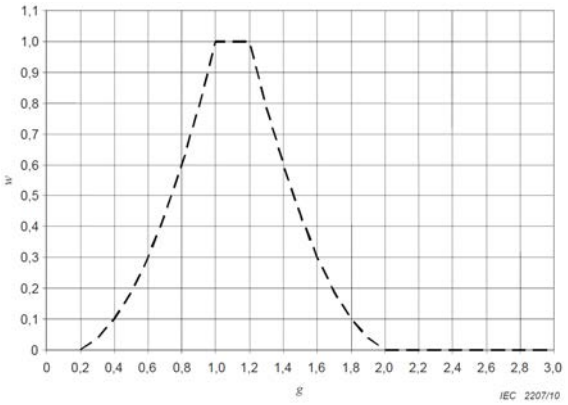

Figure 6.8: Exponent w for air density correction function of g [19].

6.6 Results

The breakdown voltage of the reduced scale GIL was investigated under different conditions. The BV tests were carried out with air at atmospheric pressure and then with CF_3I/CO_2 (30%/70%) mixture at 0,1 MPa (abs). The coaxial geometry has been tested, for each gas, in three different situations:

1. HV electrode in clean conditions;
2. HV electrode with a small metal protrusion attached;
3. HV electrode with a big metal protrusion attached.

The dimensions of the asperities used during these experiments have been previously presented in section 6.3.

At the beginning, the expected results from the breakdown voltage tests were to get a lower V_b when air was used as insulating medium compared to the V_b obtained with CF_3I/CO_2.
For what concern the introduction of the asperities in the coaxial geometry, the predicted behaviour of the gases was to obtain lower values of V_b when bigger disturbances were introduced.

HV electrode conditions	**Air**	**CF_3I/CO_2**
Clean	$V_b \geq 36$ kV	$V_b > 36$ kV
Small asperity	$V_b = 34{,}56$ kV sd = 3,6%	$V_b > 36$ kV
Big asperity	$V_b = 19{,}02$ kV sd = 2,1%	$V_b > 36$ kV

Table 6.2: Breakdown voltage comparison between air and CF_3I/CO_2 mixture in different conditions.

In the table above are shown the results of breakdown voltage tests, referred to standard atmospheric conditions.
Firstly, it is important to note that the maximum voltage applicable during the tests was 36 kV and, as explained in section 3.2.2, is due to the bushing. Regarding the results with air in clean conditions, it is interesting to note that the sparkover is occurred only sometimes around the voltage limit of the bushing. This means that its breakdown voltage is slightly higher or in correspondence of 36 kV, but unfortunately it could not be explored to not compromise the bushing insulation. Furthermore, it is worth to remember that in the COMSOL model the maximum electric field in the middle of the coaxial geometry was 0,606 kV/cm with 1 kV peak applied. Thus, considering an air dielectric strength $\approx$ 30 kV/cm, the model confirms that the breakdown voltage in clean conditions is around the value found with the tests.
The air BV results show, as was expected, a reduction of the breakdown voltage which is proportional to the dimension of the protrusions introduced.

The behaviour found is explainable considering the effect of the defects on the electric field. When the voltage is applied to the inner electrode with a protrusion on its surface, the electric field in correspondence of the disturbance is much higher because it is a very sharp point. Thus, it can be seen in the air column that the V_b decreases of 4% and 47% with the small and the big particle respectively.

For what concern the CF_3I/CO_2 mixture, the breakdown voltage never occurred, not even with the insertion of disturbances. This confirms a greater insulation capability compared to air, as was expected from the literature. In conclusion, it is interesting the BV comparison between air and CF_3I/CO_2 when a big disturbance is applied on the HV electrode. It can be seen from table 6.2 that the breakdown voltage value of CF_3I/CO_2 is greater than two times than the one found with air. Thus, this shows a good response of the gas even with a big disturbance inserted.

Chapter 7

PDIV tests with the coaxial geometry

7.1 Introduction

GIL are a very reliable electric system which uses a strong electronegative gas (SF_6) as insulating medium. Their benefits are many, as explained in section 1.3. Nevertheless, they need a high attention to details during the manufacturing, transferring and installing phases because internal defects may occur. The importance to have a clean GIL structure is necessary to have a long term reliability of the system. If some internal defects are present, they will induce partial discharge (PD) that cause premature ageing of the insulating gas which can lead to system failures. Some of the most common internal defects are metal protrusion, floating potential, insulator metal pollution, free metal particles and insulator gap [44].

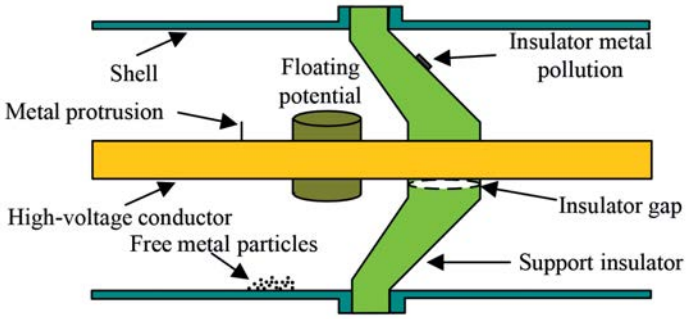

Figure 7.1: Example of the most common internal defects [44].

In this chapter will be presented the investigation of how metal protrusions affects partial discharge inception voltage in a reduced scale GIL insulated with air or with CF_3I/CO_2 (30%/70%) mixture.

Metal protrusion is very harmful for the insulation performance because its sharp tip creates a local increasing of the electric field. This strong electric field region generates undesired PD and a decreasing of the breakdown voltage (as seen in section 6.6).

PD characteristics are different if the metallic protrusion is attached on the HV conductor or on the enclosure. In the first case, the first discharges occur during the negative half-cycle of the AC voltage. On the other hand, if the protrusion is placed on the enclosure, the first– discharges occur during the positive half-cycle. The PD behaviour obtained when a metallic protrusion is on the HV electrode can be physically explained.

During the negative half-cycle, there is a high non-uniform electric field in correspondence of the protrusion(-) thus, in this region electrons are emitted by some mechanisms such as field emission or positive ion bombardment [6]. Electrons move quickly to the enclosure and leave behind them a positive space charge area. Since this positive space charge is near the protrusion, there is an intensification of the electric field in the region in between. Therefore, PD occur when the increased electric field in that precise region can reach the breakdown field intensity of the insulating gas.
On the other hand, during the positive half-cycle, in correspondence of the protrusion(+) there is the positive space charge previously created. This means that in the region between them the intensity of the electric field is decreased hence, the probability that PD occur is reduced [46].

Furthermore, it is important to note that negative PD have another advantageous condition. In correspondence of the protrusion there is an electron production thus, the avalanche can initiate as soon as the electric field in enough to have $\alpha - \eta > 0$. On the contrary, positive PD need to have free electrons passing through the volume where $\alpha - \eta > 0$. Thus, since at the onset the volume (where the effective ionization factor is positive) is very small, to have more probability to meet free electrons is necessary to increase the voltage in order to expand the volume where the onset condition is satisfied.

In conclusion, the charges generated by PD move under the effect of the electric field and this produce a pulse current but also optical, electrical, thermal and acoustic effects.

In this project, metal protrusions have been attached on the HV electrode surface in the coaxial geometry and the PD occurred in the insulating gas have been evaluated measuring the current pulses.

7.2 Preliminary tests

In this section, the first partial discharge inception voltage (PDIV) tests carried out with the coaxial geometry are presented. Further improvements on the test procedure will be presented in section 7.3.
Partial discharge standars BS EN 60270 [5] defines partial discharge inception voltage as:

applied voltage at which repetitive partial discharge are first observed in the test object, when the voltage applied to the object is gradually increased from a lower value at which no partial discharges are observed.

Therefore, this definition was the basis that guided the PDIV tests.

7.2.1 Test setup

The test setup used for this measurements is well synthesized by the equivalent scheme below:

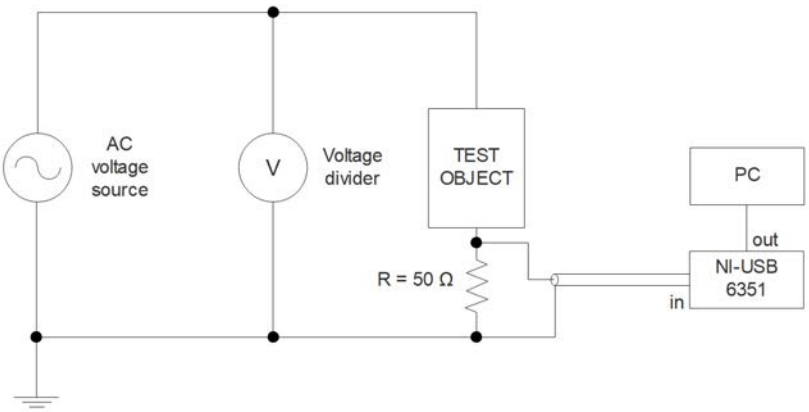

Figure 7.2: Equivalent circuit of first PDIV test.

As in the breakdown voltage tests, the AC voltage source (step-up transformer) and the voltage divider shown in figure 7.2 are the ones presented in section 3.2. The test object, thus the coaxial geometry, was placed into the pressure vessel in order to have the possibility to test at 0,1 MPa the CF_3I/CO_2 (30%/70%) mixture as insulating gas. The voltage was applied, through the bushing, to the inner electrode of the coaxial geometry where the metal protrusion was placed in the middle of it. The two external enclosures were connected directly to the ground and the enclosure in the middle to the resistor.

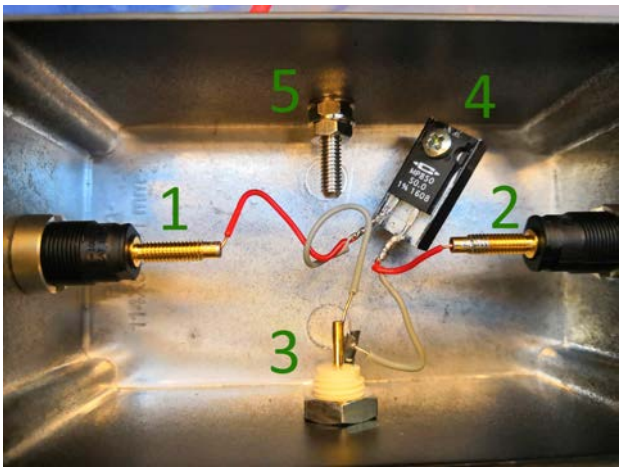

Figure 7.3: Low-inductance resistor box.

The figure above shows the resistor box used to measure PD pulses from the central enclosure of the coaxial geometry. Its main components are:

1. R INPUT, where the wire from the central enclosure is connected to the resistor;
2. R OUTPUT, where the pin of the resistor is connected to the ground;
3. COAXIAL OUTPUT, where the signal is collected from the resistor;
4. LOW INDUCTANCE RESISTOR, with R=50±1% Ω and L=10 nH;
5. BOX GROUND, where the box is connected to the ground potential.

The resistor value has been chosen both to amplify 50 times the PD pulses and to match with the coaxial-cable wave impedance, avoiding unwanted

reflections.
Multifunction I/O device (NI USB-6351) was used to constantly collect current and voltage signals during the tests and send all the data to the laptop through USB cable. In the meantime, PC was running Labview in order to save and analyse the data. The maximum sample rate of NI USB-6351 is 1,25 MS/s but, when n channels are used, the maximum sample rate per each channel is 1,25 MS/s divided for n.

(a) (b)

Figure 7.4: Metal protrusions used in the preliminary PDIV test.

(a) Small protrusion: h=0,8 mm and Ø=0,8 mm;

(b) Big protrusion: h=4,31 mm and Ø=0,8 mm.

In conclusion, it is important to note that the metal protrusions used in this preliminary test are different from the one presented in section 6.3. In this case they are slightly bigger, as shown above in the figure 7.4.

7.2.2 Test procedure

The test procedure, used in this preliminary test to evaluate the voltage threshold where the PD start to occur in the insulating gas of the coaxial geometry, will be presented below.
Partial discharge standars BS EN 60270 [5] says that, for the determination of the partial discharge inception voltage, a voltage (well below the PDIV expected) shall be applied to the test object and gradually increased.
Therefore, during the test, the voltage was increased for 50 s with a slope of 2% of V per second, where V is the final voltage value. Once reached V,

it was maintained constant for 10 s in order to see if the PD disappeared or not under constant stress.
For the whole duration of the test (60 s), current and voltage signals have been recorded using Labview with a sample rate of 500 kS/s per each channel. Furthermore, since the current signal collected from the resistor was the sum of alternating capacitive current and partial discharge pulses, an internal Labview high-pass filter (f_{cut} = 500 Hz) was utilized in the code. In this way, the evaluation of only PD pulses has been possible by rejecting the 50 Hz capacitive current signal. In addition, two minutes have been waited between consequent measurements for the same reasons explained in section 6.4.
Finally, this procedure was repeated 10 times for each gas and each condition (clean, small and big protrusion) in order to have a PDIV_{mean} with its standard deviation.

7.2.3 Results

The partial discharge inception voltage was investigated under different conditions. During the tests, air at atmospheric pressure or CF_3I/CO_2 (30%/70%) mixture at 0,1 MPa (abs) were used as gas insulation medium in the reduced scale GIL. As in the breakdown voltage tests, the coaxial geometry has been tested, for each gas, in three different situations:

1. HV electrode in clean conditions;

2. HV electrode with a small metal protrusion attached;

3. HV electrode with a big metal protrusion attached.

It is worth to remember that the metal protrusions used in this preliminary test are the ones presented in section 7.2.1.
Before to start doing the measurements, the expected results from the partial discharge inception voltage tests were to find generally $\text{PDIV}_{AIR} < \text{PDIV}_{CF_3I}$. Furthermore, when metal protrusions are inserted inside the geometry, the expected behaviour was that PDIV decreases as much as the disturbance is big.
The test results have been analysed with Matlab and one measure for each different test will be shown below.

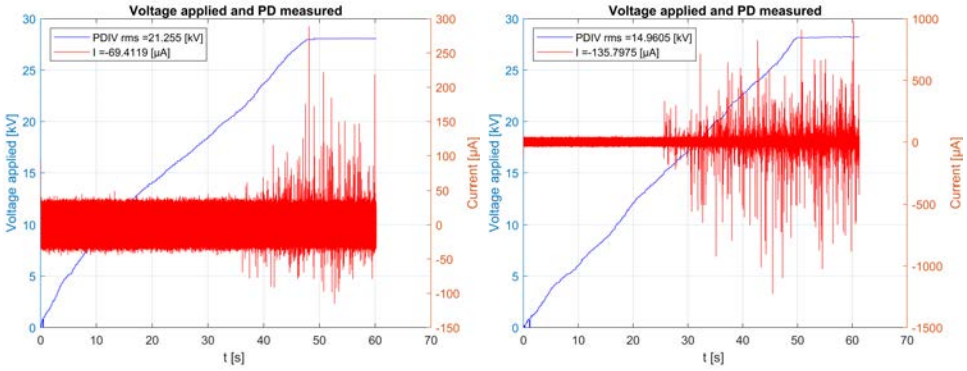

(a) Air (b) CF_3I/CO_2

Figure 7.5: PDIV test result with HV electrode in clean condition.

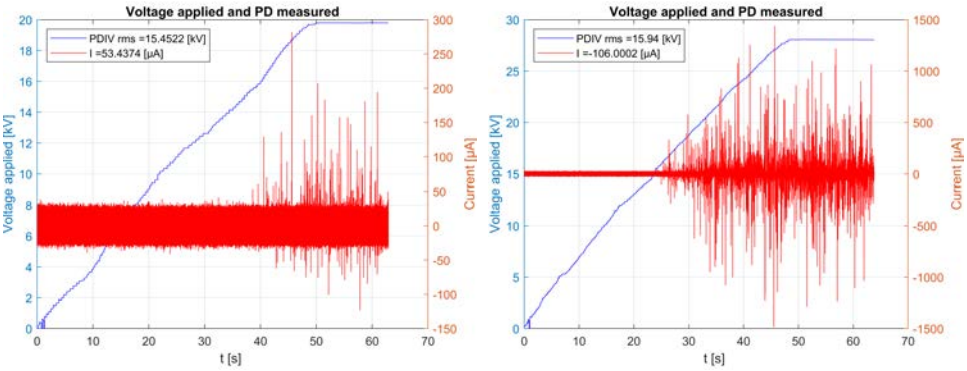

(a) Air (b) CF_3I/CO_2

Figure 7.6: PDIV test with small protrusion in the middle of HV electrode.

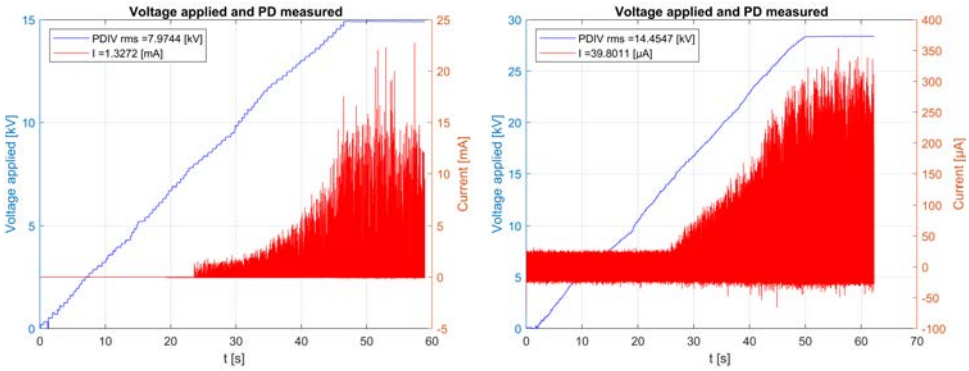

(a) Air (b) CF_3I/CO_2

Figure 7.7: PDIV test with a big protrusion in the middle of HV electrode.

The previous figures are some example of the measures obtained during the tests under different conditions. For every figure it can be seen the ramp of the RMS voltage (in blue), which has always a constant slope, and the filtered current signal (in red). In addition, in the upper left corner there are shown the values of the first current pulse chosen as PD inception and the correspondent RMS value of the voltage in that instant, hence the PDIV.
Looking at the behaviour of AIR, it can be seen from figure 7.5a and figure 7.6a that PD inceptions are not very clear and the amplitude of current pulses is in the order of magnitude of μA. On the other hand, in figure 7.7a the PD inception is well discernible and the order of magnitude has become mA.
For what concern the behaviour of CF_3I/CO_2, figure 7.5b and figure 7.6b show not clear PD inceptions and a higher amplitude of current pulses than what obtained with air. Figure 7.7b shows a clearer PD inception but the order of magnitude of the current pulses is decreased.
Furthermore, it is interesting to note that both the gases with the big protrusion show a clear PD inception and a gradual increase of the current pulse amplitude when the voltage increases.

In conclusion, it is also interesting to note that, when the V_{RMS} is maintained constant for 10 seconds, the current pulses do not decrease or stop to occur but they remain around the same amplitude.

HV electrode conditions	**Air**	**CF_3I/CO_2**
Clean	PDIV = 20,2 kV sd = 3,84%	PDIV = 14,95 kV sd = 3,15%
Small asperity	PDIV = 15,2 kV sd = 6,43%	PDIV = 15,84 kV sd = 3,23%
Big asperity	PDIV = 8,27 kV sd = 2,20%	PDIV = 14,99 kV sd = 3,81%

Table 7.1: PDIV comparison between air and CF_3I/CO_2 mixture in different conditions.

The results of 10 measures for each gas and for each HV electrode conditions are shown in the table 7.1.
Finally, the PDIV results show:

- AIR
    1. PDIV decrease as much as the metal protrusion is big;
    2. PD inception is well discernible only with the big protrusion attached on the HV electrode;
- CF_3I/CO_2
    1. PDIV does not change either with small nor with big protrusion;
    2. PD pulses density is higher with the big protrusion.

The air behaviour corresponds to what was expected, but the results obtained with CF_3I/CO_2 are difficult to understand. In conclusion, for what concern the situation when the HV electrode is free from protrusions, the results show $\text{PDIV}_{AIR} > \text{PDIV}_{CF_3I}$, which is in stark contrast to the literature.

7.3 Definitive PDIV test

Preliminary tests presented in the previous section require some progress in order to achieve a higher quality of the measurements and thus, to better understand the results obtained.
The improvements presented in this section are related to:

1. HV ELECTRODE SURFACE ROUGHNESS;
2. METHODS TO EVALUATE PD INCEPTION.

For what concern the surface roughness of the HV electrode, it is important to note that its conditions were not ideal. The electrode surface presented some high roughness points and figure 7.8 shows the worst one.
The roughness profile of the surface was measured with the instrument MarSurf PS 10 (Mahr) using the probe PHT 350. The result is show by figure 7.9. According to DIN EN ISO 4287:1998 (Roughness parameters), the total height of the roughness profile (R_t) is 66,09 μm. Therefore, the damage just seen can create a local intensification of the electric field and be

source of partial discharge at a lower voltage than the expected one. Thus, it was necessary to polish the HV electrode surface.

Figure 7.8: Worst damage point in the HV electrode.

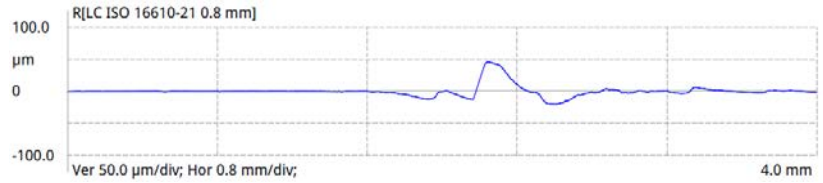

Figure 7.9: Roughness profile in correspondence of the worst damage.

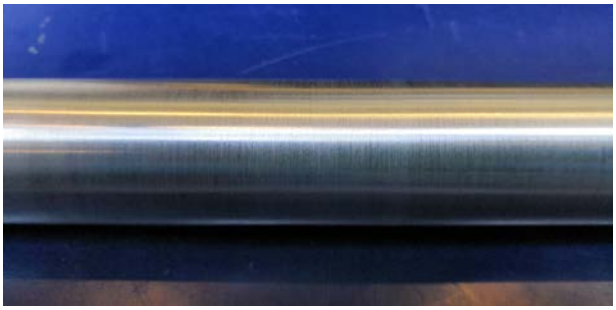

Figure 7.10: HV electrode surface after polishing treatment.

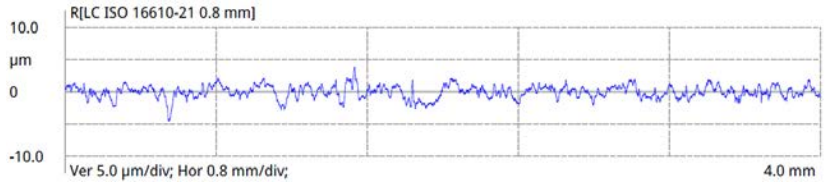

Figure 7.11: Roughness profile after polishing treatment.

The conditions of the HV electrode surface after the polishing treatment can be seen in figure 7.10.
Figure 7.11 shows the roughness profile of the HV electrode surface after the polishing treatment. As can be seen, now the roughness is much lower than the previous situation and there are no points above 10 μm, which is representative of the roughness of real inner conductor used in GIL (as presented in section 1.2).

7.3.1 Test setup

The test setup used for these new measurements was almost the same for what concern the high-voltage circuit such us step-up transformer, pressure vessel and divider. The two external enclosures of the coaxial geometry are still connected directly to the ground and the central one is connected to the low-inductance resistor.
The improvements made to this new test are related to the measuring system because it was the weak point of the precedent tests. As explained in the section 7.3.2, National Instrument USB-6351 was used to collect constantly current and voltage signals. Looking at the PD characteristics with the HV electrode in clean conditions, it has been found that the rise time was around some nanoseconds and the whole duration of the pulse was around hundreds of nanoseconds (due to the oscillations). Now, if the current signal is sampled with 500 kS/s, it means that there is one point every 2 μs. Thus, it is evident that with that sample rate there are no enough number of points to cover sufficiently a PD pulse. This means that in the previous test no sample points or, if lucky, only one was randomly placed in the current pulse, so most likely the very first PD was not detected.
For this reason, two new measurements methods have been developed:

1. PERSISTENCE;
2. OSCILLOSCOPE AUXILIARY OUTPUT.

Figure 7.12 shows the persistence method setup where the DSO is the Teledyne Lecroy HDO 6104 which has a bandwidth of 1 GHz, 25 Mpts memory and a maximum sample rate of 2,5 GS/s. This oscilloscope has a persistence acquisition mode which accumulates on-screen points from many acquisitions in order to see how the input signals change over the time. In

this way, it has been possible to record for two minutes at fixed voltage the presence or absence of PD pulses. In addiction, using the persistence mode it is possible to see at which point of the voltage AC cycle the PD occurs and also after how long from the voltage application.
The sample rate choice has been a trade-off between:

- SHORT DELAY TIME Δt between two triggers. In the persistence acquisition mode, after that the oscilloscope triggers, it needs time to add the data on the screen and then returning available to trigger again. Obviously, Δt is proportional to the number of points taken. Therefore, since the time window is fixed, Δt is proportional to the sample rate;
- ENOUGH POINTS TO COVER PD PULSE.

After this considerations, the sample rate chosen is 250 MS/s. In this way, Δt is not very big so not many data are lost and every 4 ns a sample is taken, which allows to have some points positioned on a PD pulse.

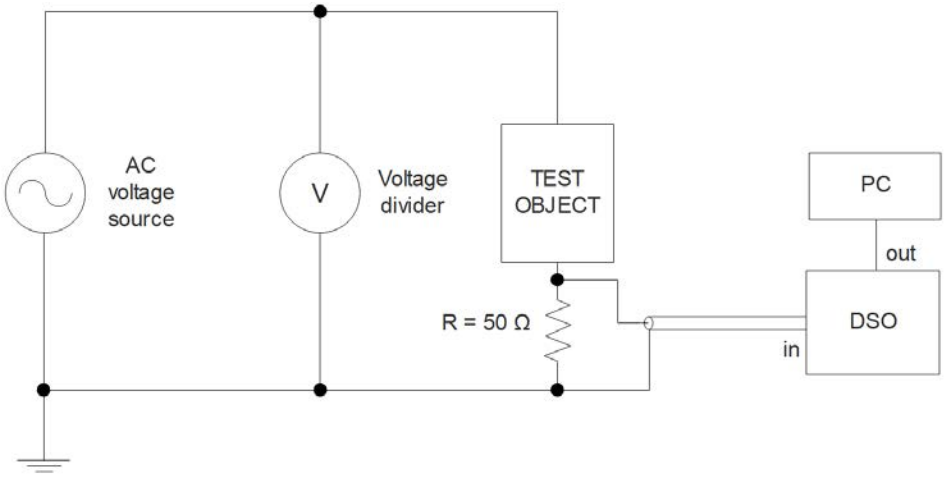

Figure 7.12: Equivalent circuit of the test setup for persistence method.

The setup used with the oscilloscope auxiliary output method is presented by figure 7.13. In this setup, the DSO used is the Lecroy WaveJet Touch 354 already presented in section 6.2.
During the test, this oscilloscope has been used with its maximum sample rate 2 GS/s in order to have enough point to represent properly the PD

pulses collected from the low-inductance resistor. This method is based on the auxiliary output pulse that is generated by the oscilloscope. Basically, when it triggers, it also produces an output pulse with an amplitude around 3 V in a very short time ($\approx 1{,}5\mu s$). Therefore, since the oscilloscope can detect the very first PD pulse (with 2 GS/s), the trigger has been set in order to catch PD pulses and, when it happen, a 3 V pulse is generated from its output. In conclusion, recording the output pulses from the trigger and the voltage with National Instrument USB-6351, it is possible to measure the PDIV avoiding low sample rate problem had in the preliminary test.

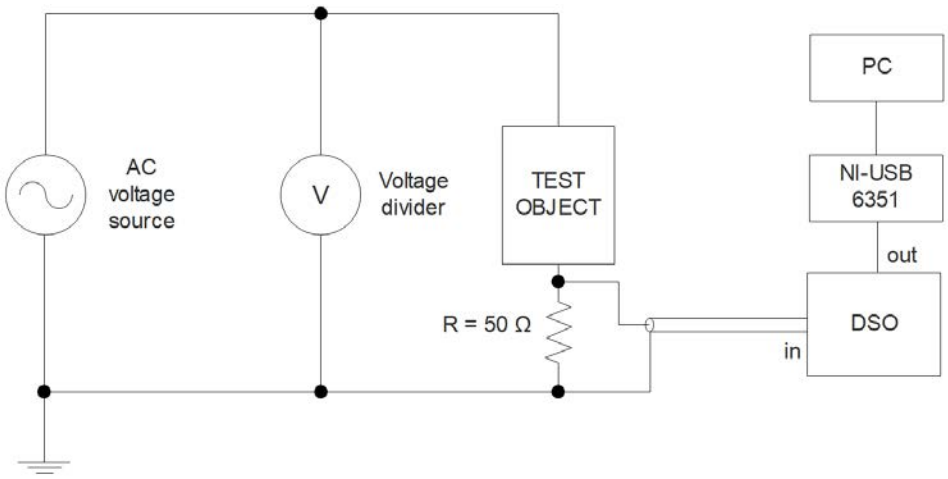

Figure 7.13: Equivalent circuit of the test setup for oscilloscope auxiliary output method.

7.3.2 Test procedure

During the persistence measurements the oscilloscope Teledyne Lecroy HDO 6104 has been set with:

- sample rate = 250 MS/s;
- horizontal axis (time) = 2 ms/div;
- vertical axis (voltage) = 5 V/div;
- vertical axis (voltage) = 200 mV/div;
- trigger settings: level = 0 V, slope = positive, source = voltage;

The procedure is to record for two minutes, with the persistence mode, voltage and current signals starting from a low voltage where no PD are detected. Then, this measure is repeated for voltage steps of 1 kV which, close to the PDIV, become 0,5 kV.

For what concern the oscilloscope auxiliary output method, the oscilloscope Lecroy WaveJet Touch 354 has been set with:

- sample rate = 2 GS/s;
- horizontal axis (time) = 200 ns/div;
- vertical axis (current) = variable according to the pulses;
- trigger settings: level = 36 mV, slope = positive, source = current;

It is important to note that the trigger level has been chosen 36 mV because, from precedent persistence measures, that value is referred to the smallest PD that can be distinguished from the AC current. Thus, in this measurements all the current pulses with a peak greater than 720 μA are detected by the oscilloscope, which produces an output pulse that is collected by the National Instrument USB-6351 (sampling at 500 kS/s for each channel) and recorded by Labview.
Finally, the procedure consists to apply a voltage ramp with a 0,55 kV/s slope until PD occur and, setting the oscilloscope trigger in normal mode, NI USB-6351 device will collect the auxiliary pulses referred to PD detected. PDIV is easily obtainable by observing, from the Labview results, V_{RMS} value in correspondence of the first pulse. In conclusion, this procedure has been repeated 10 times in order to have a $PDIV_{mean}$ with its standard deviation and two minutes have been waited between consequent measurements.

7.3.3 Results

The partial discharge inception voltage and their characteristics have been investigated under different conditions. As in the previous tests, the two insulating medium used in the reduced scale GIL are air at atmospheric pressure and CF_3I/CO_2 (30%/70%) mixture at 0,1 MPa (abs). Each gas has been tested with three different conditions of the HV electrode, such as clean, with a small and with a big protrusion which are intended to represent possible defects present in GIL structure. It is important to note that the

metal protrusion utilized in these tests are the ones presented in section 6.3.

AIR in clean conditions

Figure 7.36 shows that some activity starts at V_{RMS}=23 kV and, from the video of the recorded measure, the first PD is occurred after 20s from the voltage application. Figure 7.15 shows that the PD activity is completely started at V_{RMS}= 24 kV. It is interesting to note that the two pulses (figure 7.37 and figure 7.17) have a similar pattern and the peak is greater when the voltage applied is higher. Finally, figure 7.18 present an example of the PDIV obtained under a voltage ramp.

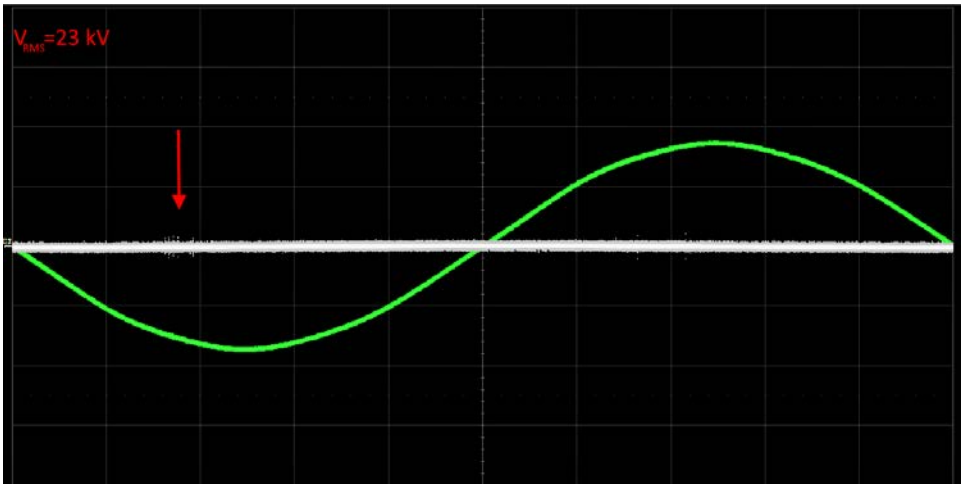

Figure 7.14: Persistence result after 2 minutes at V_{RMS}= 23 kV.

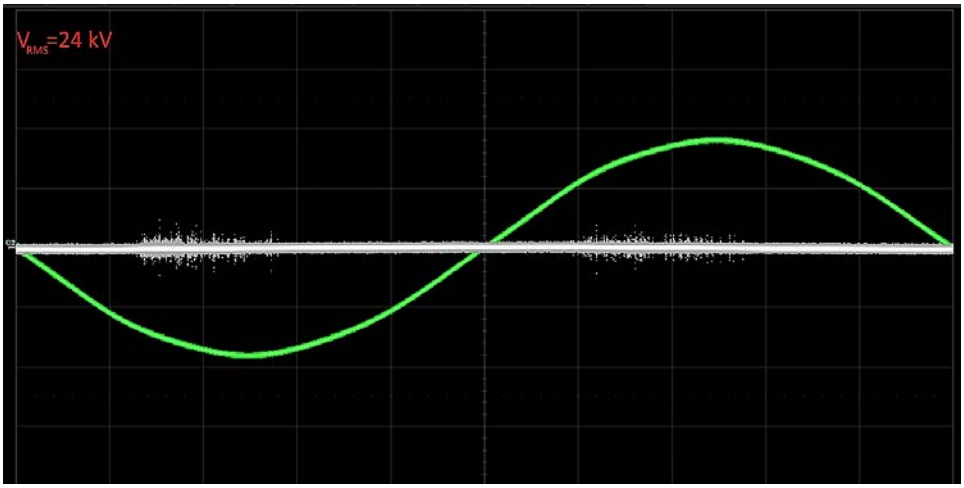

Figure 7.15: Persistence result after 2 minutes at V_{RMS}= 24 kV.

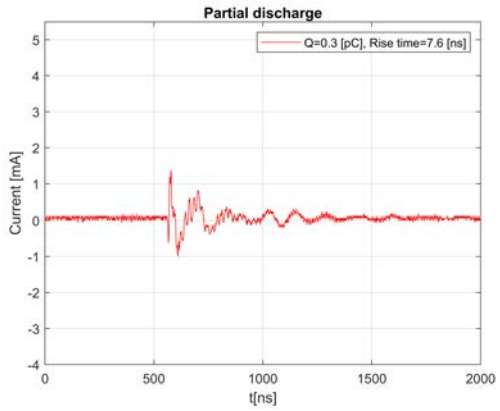

Figure 7.16: Current pulse detected at V_{RMS}= 23 kV.

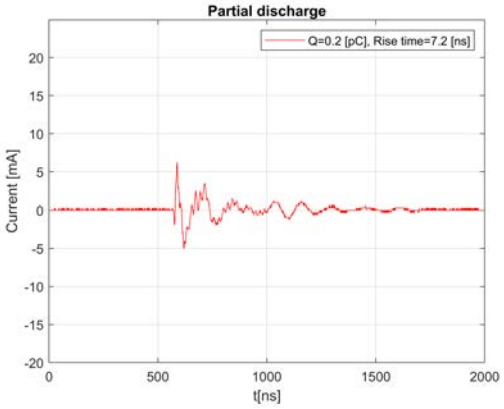

Figure 7.17: Current pulse detected at V_{RMS}= 24 kV.

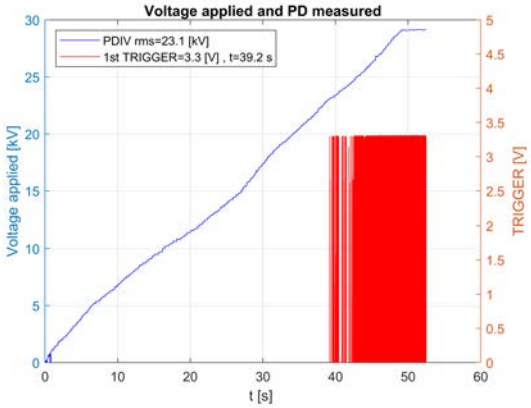

Figure 7.18: Example of a PDIV measure with the oscilloscope output pulse.

In conclusion, the 10 measures carried out with the oscilloscope auxiliary output method show that $PDIV_{mean}$ = 22,9 kV with a standard deviation = 1,6%. This result is in accordance with the result of the persistence method because the first PD appearances are between 23 and 24 kV.

AIR with small metal protrusion

Figure 7.19 shows that no PD occurred for two minutes under V_{RMS}=22 kV. When the voltage was increased at V_{RMS}=22,5 kV, the first PD appeared in the negative half-cycle after few seconds and, after around 10 s, PD started to occur also in the positive half-cycle.

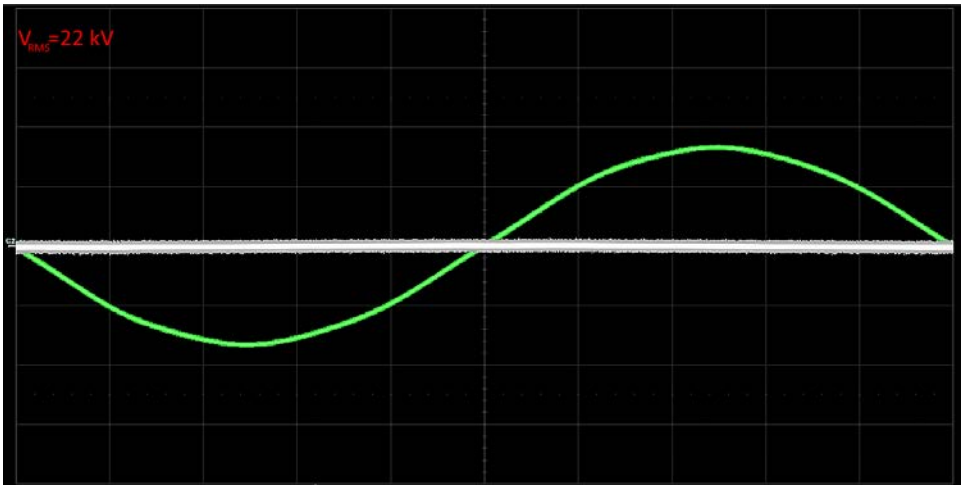

Figure 7.19: Persistence result after 2 minutes at V_{RMS}= 22 kV.

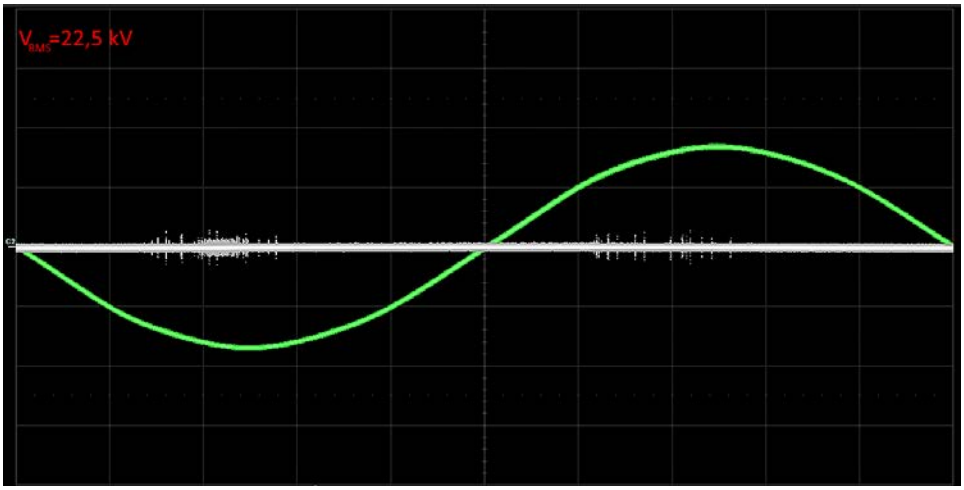

Figure 7.20: Persistence result after 2 minutes at V_{RMS}= 22,5 kV.

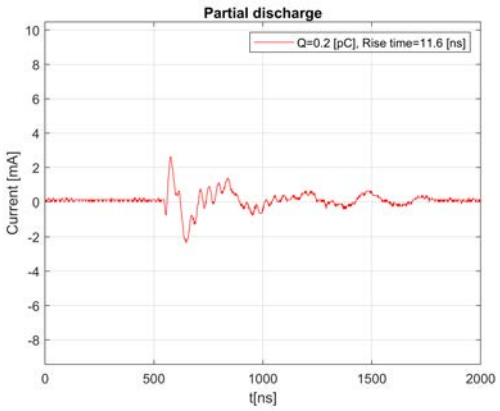

Figure 7.21: Current pulse detected at V_{RMS}= 22,5 kV.

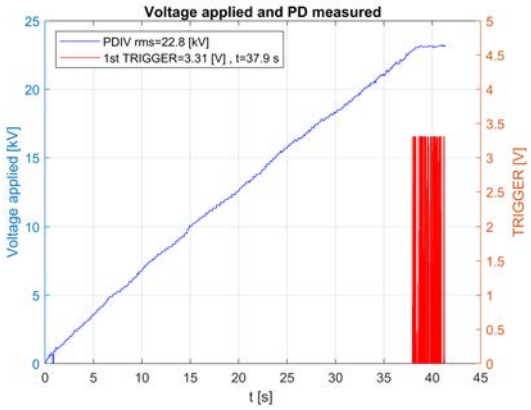

Figure 7.22: Example of a PDIV measure with the oscilloscope output pulse.

The figure 7.21 shows a current pulse collected when the voltage applied was 22,5 kV. It can be seen that the pulse pattern is more ore less the same of what had with air in clean conditions.
Furthermore, an example of the behaviour under a ramp voltage of 0,55 kV/s is shown by figure 7.38.
Finally, the result obtained measuring 10 times with the oscilloscope auxiliary output method says that $PDIV_{mean}$ = 22,5 kV with a standard deviation = 3,4%.
The persistence result shows PD activity between 22 and 22,5 kV, so the two results achieved with different methods agree.

AIR with big metal protrusion

Figure 7.23 shows that the pulses occur only in the negative half-cycle and, from the video of the recorded measure, the first PD appeared as soon as the voltage reached 11 kV. Figure 7.24 shows that with a little voltage increment, very high PD pulses starts to appear also under the positive half-cycle.
In addition, it is important to note that these persistence results agree to what said in the introduction of the current chapter. Here it can easily be seen that, with a metal protrusion attached in the HV electrode, the PD start to occur during the negative half-cycle.

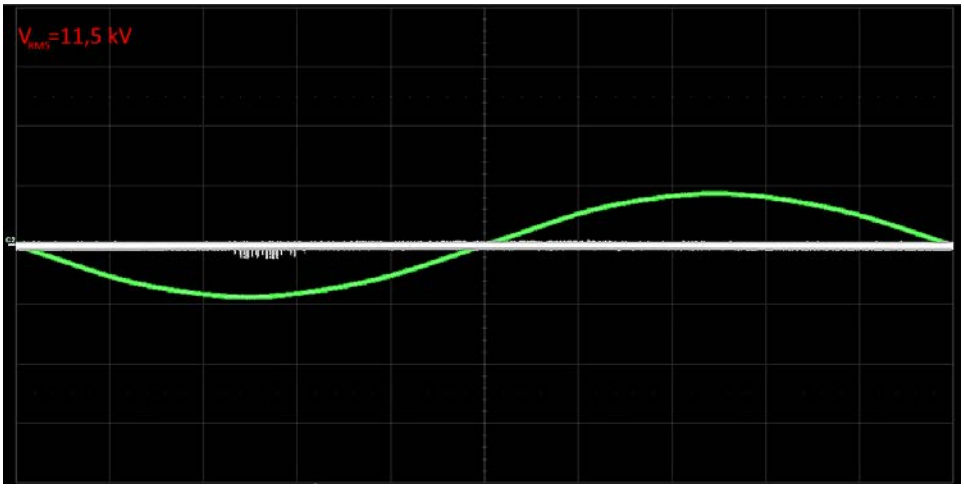

Figure 7.23: Persistence result after 2 minutes at V_{RMS}= 11,5 kV.

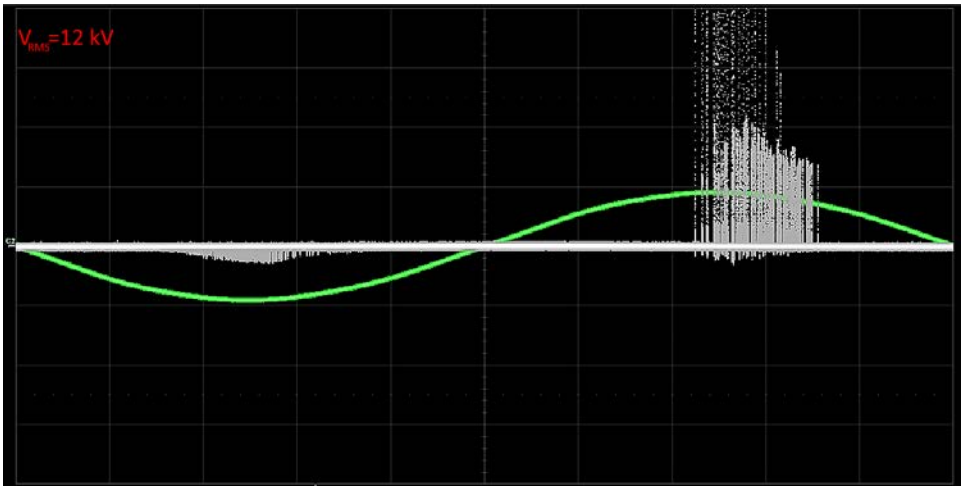

Figure 7.24: Persistence result after 2 minutes at V_{RMS}= 12 kV.

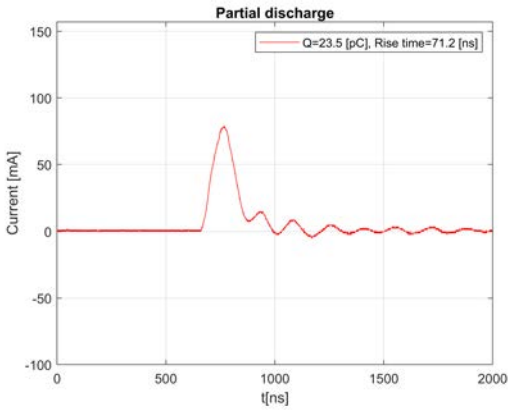

Figure 7.25: Current pulse detected at V_{RMS}= 12 kV.

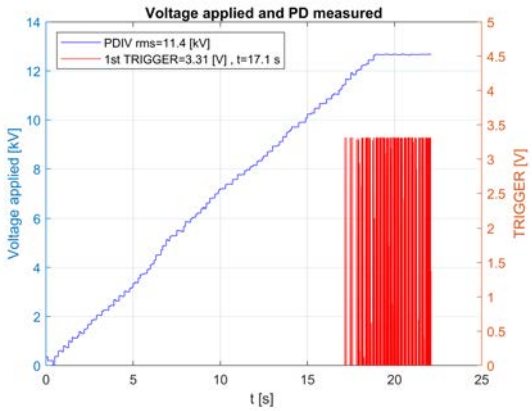

Figure 7.26: Example of a PDIV measure with the oscilloscope output pulse.

From figure 7.23 is interesting to note that the PD shown should be Trichel pulses because they have a lower inception voltage and because their density increase proportionally with the voltage (figure 7.24). The figure 7.25 shows a PD pulse collected with the oscilloscope under 12 kV. For what concern streamer discharges, it is well known that they create pulse charges between 10 pC and some hundreds of pC [2]. Therefore, looking at the charge value, which is evaluated integrating the current pulse, it is possible to affirm that the current pulses collected in this situation are from streamer discharges in air. In conclusion, the 10 measures carried out with the oscilloscope auxiliary output method say that $PDIV_{mean}$ = 11,7 kV with a standard deviation = 6%. Once again, these results perfectly agree with the range individuated by persistence method which is 11,5 ÷ 12 kV.

CF_3I/CO_2 in clean conditions

Figure 7.27 shows only three PD occurred in two minutes at V_{RMS}= 20 kV. During the measure, it has been seen that the first appeared after 40 s and it is the one at the maximum of the positive half-cycle.
The situation changes when 21 kV are applied because, as can be seen in figure 7.28, PD density is much higher and they started to occur as soon as the voltage was increased.

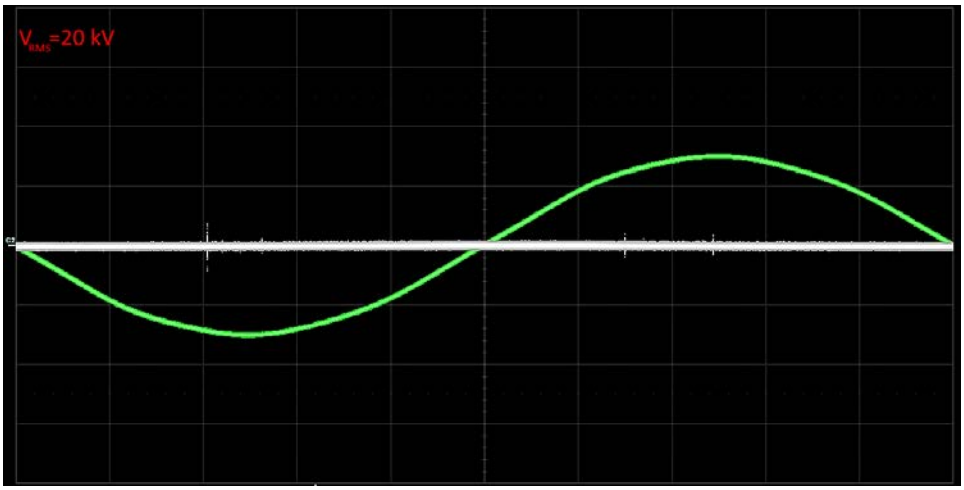

Figure 7.27: Persistence result after 2 minutes at V_{RMS}= 20 kV.

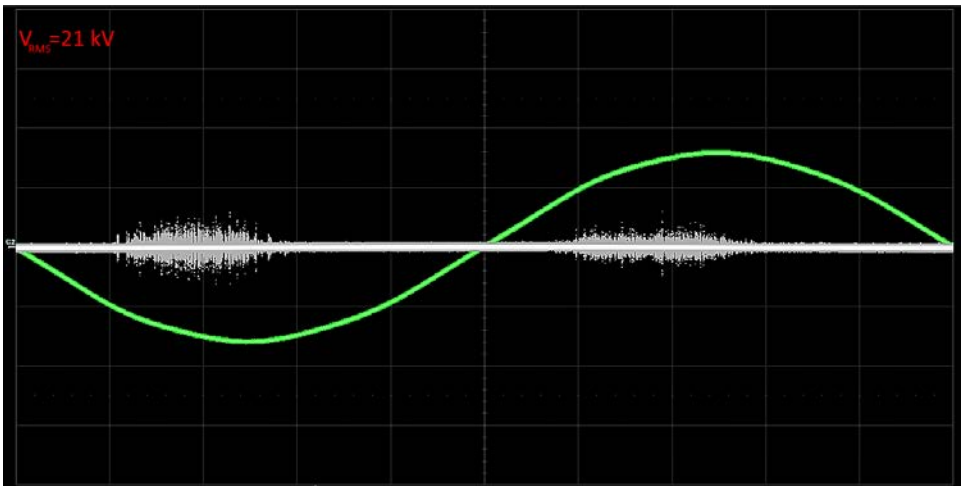

Figure 7.28: Persistence result after 2 minutes at V_{RMS}= 21 kV.

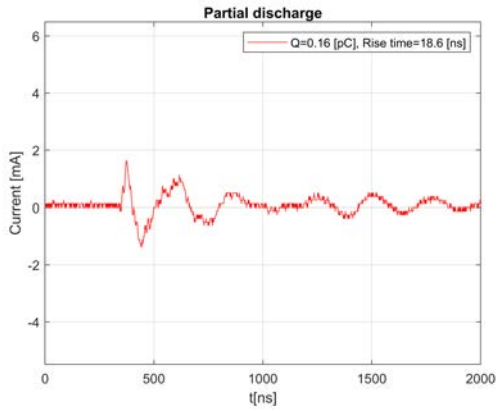

Figure 7.29: Current pulse detected at V_{RMS}= 21 kV.

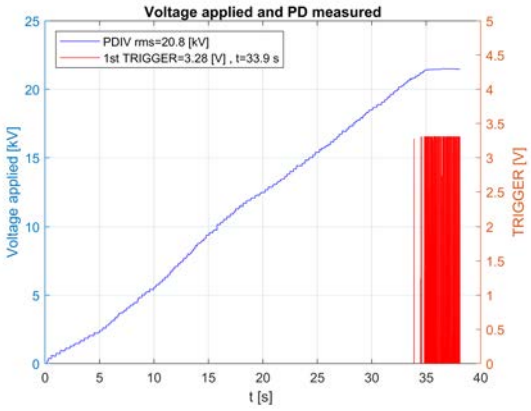

Figure 7.30: Example of a PDIV measure with the oscilloscope output pulse.

In figure 7.29, a current pulse obtained under 21 kV is shown. It is interesting to note that the pattern is very similar to the current pulses obtained with air both in clean conditions and with the small metal protrusion.
An example of the PDIV measurements during a 0,55 kV/s voltage ramp is shown by figure 7.30.
Finally, the results after 10 measures with the oscilloscope auxiliary output method are $PDIV_{mean}$ = 20,9 kV with a standard deviation = 1,5%. Thus, the result match with the persistence observations where PD have been found in the range 20 ÷ 21 kV.

CF_3I/CO_2 with small metal protrusion

Figure 7.31 shows that no PD occurred for two minutes under V_{RMS}= 15 kV. In figure 7.32, it can be clearly seen that PD activity is started in both the half-cycles when the voltage has been increased to V_{RMS}= 15,5 kV.
From the video recording of the measurements, the first PD pulse is appeared under the negative half-cycle after 10 s.
For what concerns the first PD under the positive half-cycle, it is appeared after 18 s.

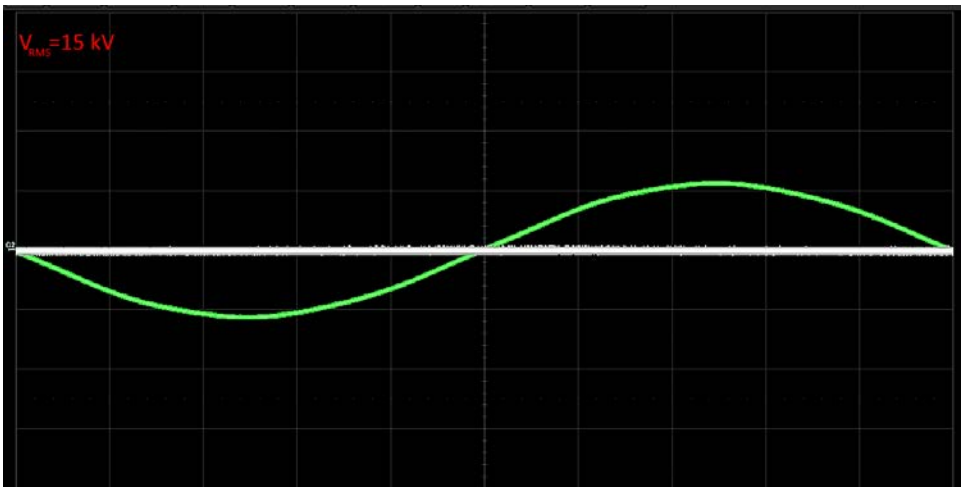

Figure 7.31: Persistence result after 2 minutes at V_{RMS}= 15 kV.

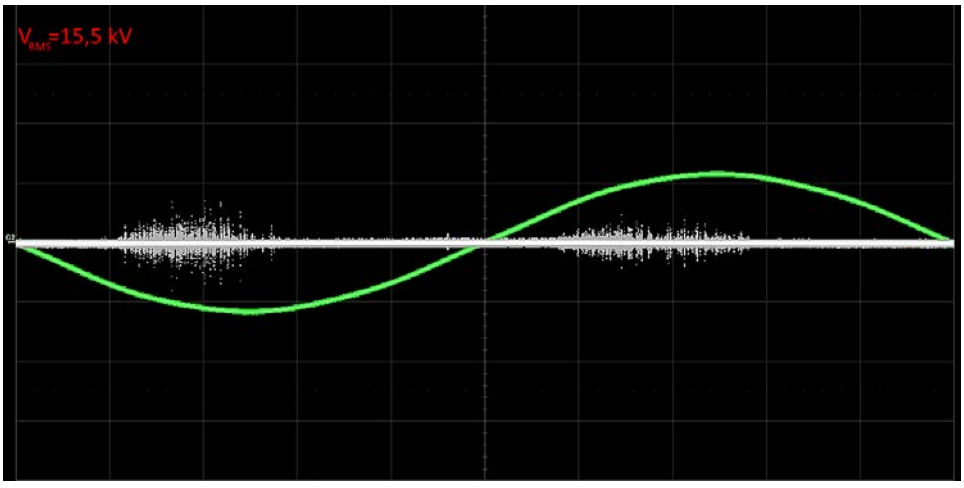

Figure 7.32: Persistence result after 2 minutes at V_{RMS}= 15,5 kV.

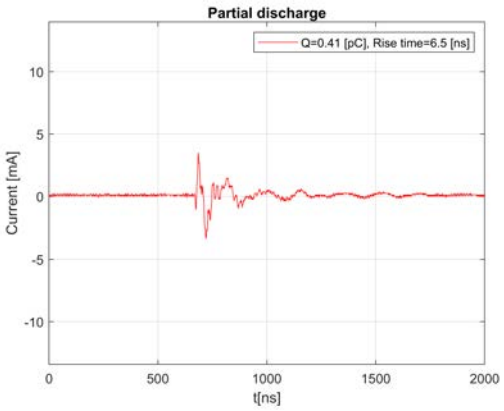

Figure 7.33: Current pulse detected at V_{RMS}= 15,5 kV.

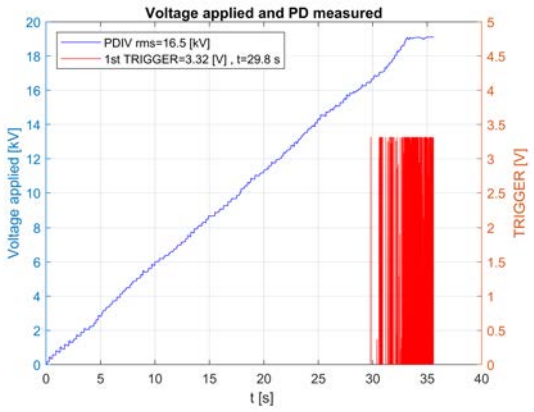

Figure 7.34: Example of a PDIV measure with the oscilloscope output pulse.

From figure 7.33 the current pulse that occurred at V_{RMS}= 15 kV can be seen. Once again, its shape shows a similar pattern with all the pulses seen so far, except in the case of air with big metal particle.
For what concern the partial discharge inception voltage measurements carried out with the oscilloscope output method, the $PDIV_{mean}$ found is 15,4 kV with a standard deviation = 2,0%. Comparing this result with the persistence range where PD activity started (15 ÷ 15,5 kV), a perfect match is found.

CF_3I/CO_2 with big metal protrusion

Figure 7.35 shows that some small activity starts at V_{RMS}= 22 kV in correspondence of the red arrow, but it is not repetitive. When the voltage is increased to V_{RMS}= 23 kV some clear and higher activity starts under both negative and positive half-cycle. In addiction, from the video recording of the measurements it has been possible to see that PD started as soon as the voltage was applied.

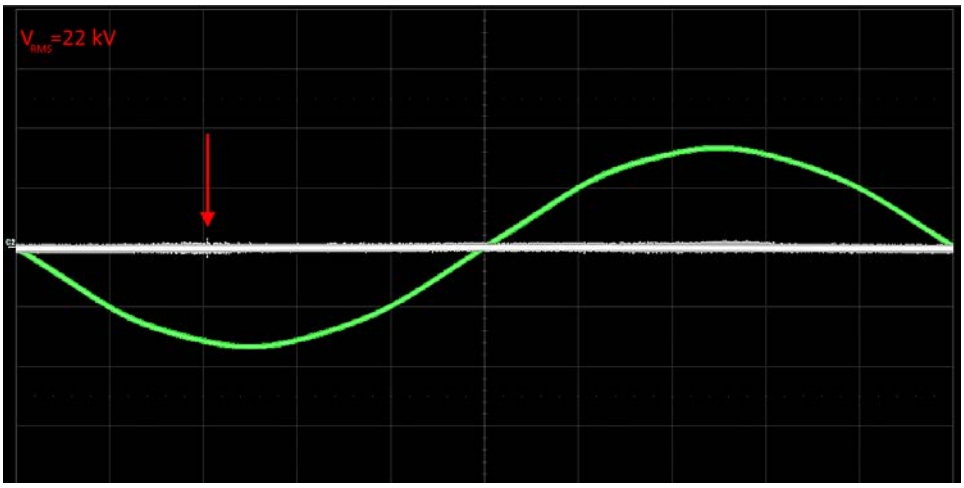

Figure 7.35: Persistence result after 2 minutes at V_{RMS}= 22 kV.

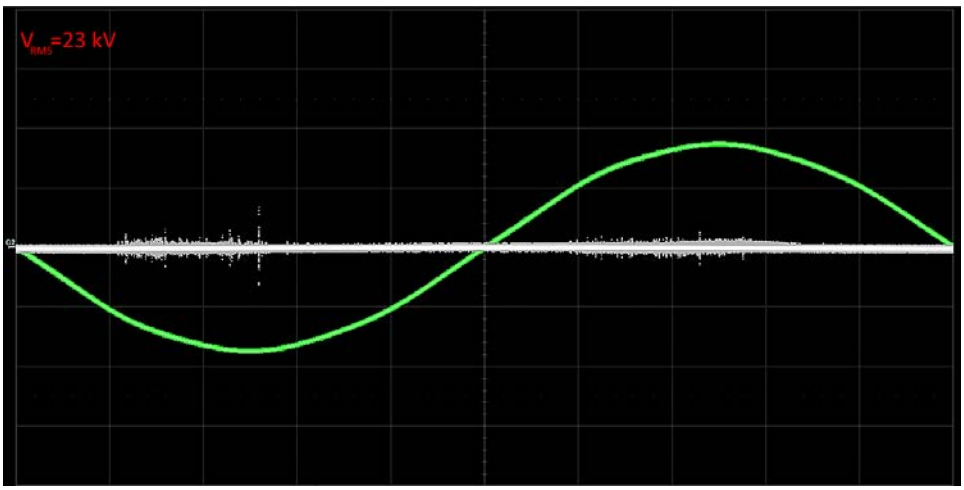

Figure 7.36: Persistence result after 2 minutes at V_{RMS}= 23 kV.

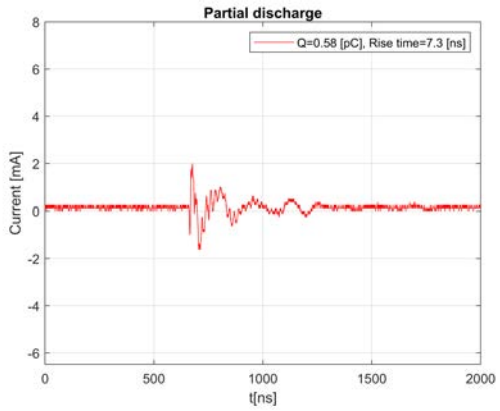

Figure 7.37: Current pulse detected at V_{RMS}= 23 kV.

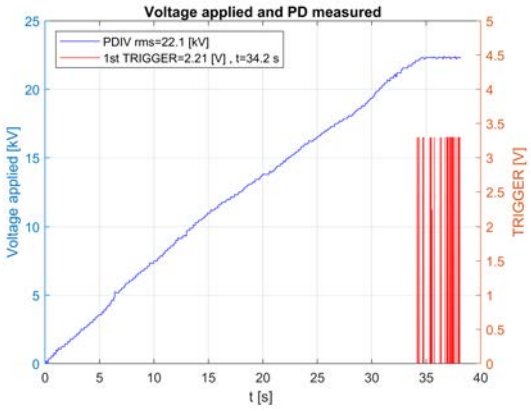

Figure 7.38: Example of a PDIV measure with the oscilloscope output pulse.

In figure 7.37 is presented one of the current pulses appeared at V_{RMS}= 23 kV. Here as well, it is possible to recognize the same pattern that have characterized all the measurements so far, with the exception of big protrusion in air.
In conclusion, after 10 measures the result of the oscilloscope auxiliary output method is a $PDIV_{mean}$ = 21,4 kV with a standard deviation = 1,4%.

HV electrode conditions	**Metohd**	**Air**	**CF_3I/CO_2**
Clean	Persistence	PDIV = 23 ÷ 24 kV	PDIV = 20 ÷ 21 kV
	Scope pulse	PDIV = 22,9 kV sd = 1,6%	PDIV = 20,9 kV sd = 1,5%
Small protrusion	Persistence	PDIV = 22 ÷ 22,5 kV	PDIV = 15 ÷ 15,5 kV
	Scope pulse	PDIV = 22,5 kV sd = 3,4%	PDIV = 15,4 kV sd = 2,0%
Big protrusion	Persistence	PDIV = 11,5 ÷ 12 kV	PDIV = 22 ÷ 23 kV
	Scope pulse	PDIV = 11,7 kV sd = 6,3%	PDIV = 21,4 kV sd = 1,4%

Table 7.2: PDIV definitive results with air or CF_3I/CO_2 mixture in different conditions.

The table above summarize the partial discharge inception voltage results obtained with air at atmospheric pressure and CF_3I/CO_2 (30%/70%) mixture at 0,1 MPa (abs).
Looking at table 7.2, final conclusion are:

1. the results from the two different methods developed in order to measure PDIV are in agreement;
2. air PDIV behaviour under different HV electrode conditions shows a decrease proportional to the defect inserted, as was expected;
3. CF_3I/CO_2 PDIV behaviour is very different from what was expected based on the literature;

Furthermore, it is important to note that the current pulses collected during the tests show two different patterns. All the tests, except the one done using air with the big metal protrusion, have the same pattern characterized by few nanoseconds of rise time and a very small associated charge (< 1 pC).

On the other hand, the current pulses obtained with air and the big metal protrusion show a well known pattern in the air PD field [15]. All the current pulses detected by the oscilloscope in this condition show a defined shape and precise characteristics, such as an associated charge slightly greater than 10 pC (which increases with the increasing of the voltage applied) and a rise time that is around 70 ns, which accords with what found in [15].

In conclusion, considering that CF_3I/CO_2 mixture tested with the coaxial geometry presented:

- PDIV results that do not change with protrusions insertion;
- PDIV results in disagreement with the literature and with the dielectric strength of the mixture;
- PD activity which has been detected at voltage much lower than the theoretical breakdown voltage;

it cannot be said that the results obtained are representative of the mixture behaviour under high voltage thus, more investigation are necessary to understand the problems had during the tests.

7.4 Plane-plane test

In this section there will be presented the tests carried out using CF_3I/CO_2 (30%/70%) mixture at 0,1 MPa (abs) as insulating gas, but with a plane-plane geometry.
Considering that:

1. PD measured with the coaxial geometry most likely did not occur in the CF_3I/CO_2 mixture;
2. current pulses have the same pattern, which means that the partial discharges are localized somewhere;
3. COMSOL model shows the maximum of the electric field on the tip of the HV electrode;

the bottom polypropylene insulator was the main suspect source of PD. The aim of the test presented in this section was to understand if the partial discharges measured were due to some defects in the bottom insulator.

In order to understand if the PD source was in the bottom insulator and to recreate similar electric field conditions as in the coaxial geometry, a plane-plane geometry was tested. The electrodes dimensions have been already presented in section 3.4.1. The chosen gap is 3 cm to have the same distance as in the reduced scale GIL geometry.

7.4.1 Test setup

The test setup is exactly the same used in the previous tests thus, the transformer HV output is connected to the bushing on the pressure vessel and to the divider for the voltage measurements.
The plane-plane geometry was placed into the pressure vessel as can be seen from figure 7.39. The HV electrode was connected directly to the conductor of the bushing. The other plane was connected, using the insulated copper wire present in the figure, to the input of the low-inductance resistor outside the vessel.
Furthermore, it is important to note that the ground electrode was supported with a structure composed by an insulator in order to prevent a direct contact with the ground.

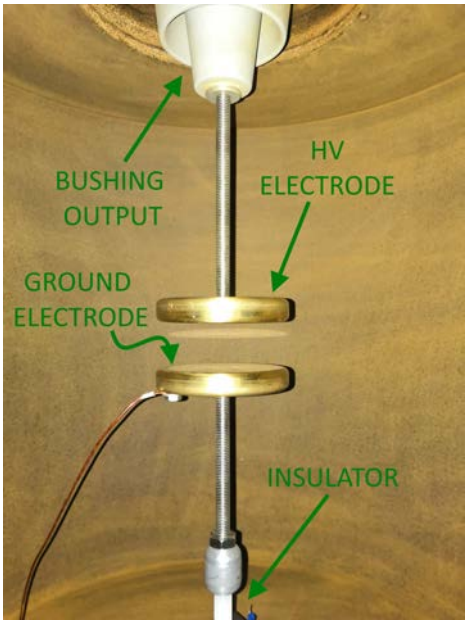

Figure 7.39: Plane-plane geometry inside the pressure vessel.

7.4.2 Results

The partial discharge inception voltage results presented in this section were obtained using the same test procedure of the previous test (explained in section 7.3.2). In addiction, it is important to note that the metal protrusion utilized in this test are the ones introduced in section 6.3 (the same used in the previous test).

HV electrode conditions	**Metohd**	**CF_3I/CO_2**
Clean	Persistence	PDIV = 19 ÷ 22 kV
	Scope pulse	PDIV = 21,7 kV sd = 1,4%
Small protrusion	Persistence	PDIV = 19 ÷ 20 kV
	Scope pulse	PDIV = 19,3 kV sd = 2,2%
Big protrusion	Persistence	PDIV = 20,5 ÷ 21 kV
	Scope pulse	PDIV = 21,8 kV sd = 3,5%

Table 7.3: PDIV results with CF_3I/CO_2 mixture in a plane-plane geometry under different conditions.

The results presented in the table above show again that PDIV:

- do not change with the protrusions insertion;
- is still in disagreement with the literature and with the dielectric strength of the mixture.

Therefore, this behaviour can be attributed to an external PD source and more investigations need to be done in order to identify it.
In conclusion, this test can affirm that the insulators of the coaxial geometry are not the PD source that affects the results.

Chapter 8

Conclusions

In this thesis, the performance of a reduced scaled GIL insulated using a CF_3I/CO_2 mixture were investigated under high alternating voltage.
Firstly, the geometry subject of study was simulated using a commercial FEM software (COMSOL Multiphysics 5.3a) in order to understand the electric field distribution on it.
Secondly, as presented in section 5.4, the capacitance between the HV electrode and the central enclosure has been evaluated in three different methods to confirm the reliability of the model built. The results of the capacitance evaluation show that the model is trustable thus, the electric field distribution obtained from the simulations can be used for final considerations in the tests conclusions.
Breakdown voltage and partial discharge inception voltage tests were carried out under AC voltage in order to characterize the behaviour of CF_3I/CO_2 for a possible future use in gas insulated lines. Furthermore, two different metal protrusions, representative of real defects in gas insulated systems, were introduced into the geometry to understand their effects on the insulation capability of the gas.
Here, final conclusions of the research work done in this project are presented with some suggestions for future works.

8.1 Breakdown voltage tests conclusions

In chapter 6, breakdown voltage investigation has been carried out the on the coaxial geometry presented in section 3.3. The insulating mediums

tested in the pressure vessel were air at atmospheric pressure and CF_3I/CO_2 (30%/70%) at 0,1 MPa (abs). It is worth noting that air was tested to become familiar with the test procedure and the devices present in the laboratory, but also because its behaviour under high voltage environment it is well known since it is widely used. The breakdown voltage tests were carried out in clean condition, but also with different metal protrusions on the HV electrode in order to understand how the insulation capability decreases in presence of defects.
The performances of the reduced scaled GIL, for what concern the breakdown voltage, are:

- with AIR, it has been found that the effect of the metal protrusions attached on the inner electrode is clear and very strong because V_b with the big defects is almost one half of the V_b in clean conditions.
- with CF_3I/CO_2 mixture, no breakdown occurred under any condition. These results, form a certain point of view, do not allow to determine which is its dielectric strength with the coaxial geometry in clean conditions or with the insertion of defects. From another point of view, the results obtained confirm the high insulation capability of the mixture found in the literature. Furthermore, since no breakdown is occurred with the big protrusion, it can be said that CF_3I/CO_2 mixture provides an insulation performance that is certainly greater than two times than the one found with air. Thus, this confirms a good behaviour even with a big defect in the coaxial geometry.

8.1.1 BV future works

Future investigations on the CF_3I/CO_2 breakdown voltage can be carried out in the Cardiff University laboratory in two ways, which are:

1. building a smaller coaxial geometry in order to reach the sparkover between the electrodes at lower voltage, according with the bushing limitations. In addition, if this is possible, the design of the new geometry should focus to have the maximum of electric field in the middle of the inner electrode, being the region subject of study;
2. if the same coaxial geometry want to be used, the theoretical breakdown voltage in clean conditions with CF_3I/CO_2 mixture should be

around 80 kV. Thus, since the transformer can reach 100 kV, it is necessary to change bushing with another one that has higher rated voltage.

8.2 PDIV tests conclusions

In chapter 7, partial discharge inception voltage (PDIV) investigation have been presented. The tests were carried out with air at atmospheric pressure and then with CF_3I/CO_2 (30%/70%) mixture at 0,1 MPa (abs).

After a preliminary tests, a new test procedure has been developed in order to collect PD pulses with an appropriate sample rate and therefore, to be confident of the results obtained. An overview of the PDIV results is:

- with air, it has been found that as bigger is the metal protrusion as PDIV decreases;
- with CF_3I/CO_2 mixture, PDIV results seem to be around at a certain specific range of voltage;
- PDIV does not change when a big metal protrusion is inserted.

This results, which are not in according with the literature, suggest that the PD pulses detected are from somewhere and thus, the source needs to be found.

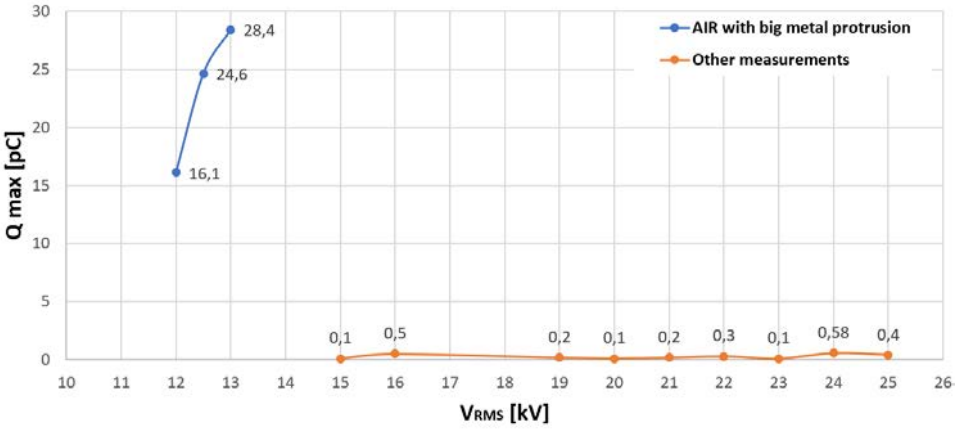

Figure 8.1: Q_{max} comparison of the pulse detected in the tests.

Analysing the maximum associated charge Q_{max} for every current pulse detected at different voltage, figure 8.1 is obtained.
Thus, considering that in streamer discharges the associated charge of current pulses is between 10 pC and 100 pC, figure 8.1 can affirm that PD between the electrodes occurred and have been measured just with air and the big protrusion.
Furthermore, it is important to note that CF_3I decomposition products can be formed by partial discharge activity [9]. Thus, a by-products analysis of the metal protrusions after the CF_3I/CO_2 tests was carried out with the scanning electrode microscope (SEM) Hitachi TM3030 and the EDX system. The results are shown in figure 8.2 and figure 8.3.

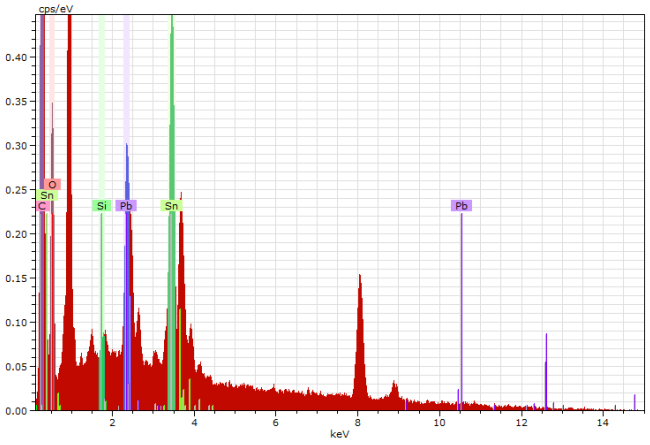

Figure 8.2: Spectrum analysis of the small metal protrusion.

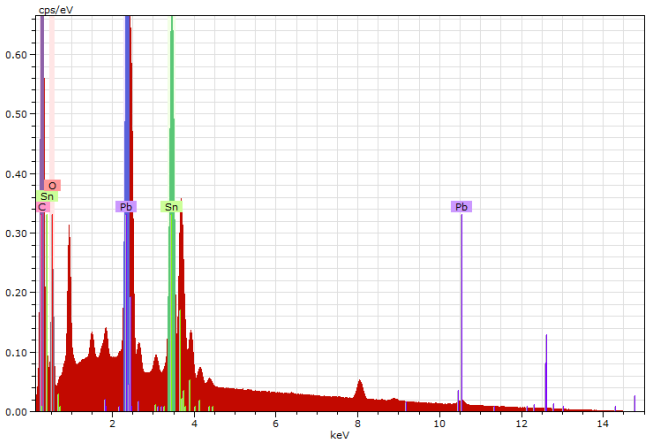

Figure 8.3: Spectrum analysis of the big metal protrusion.

In the found elements there are no traces of Iodine and therefore, this represents another proof that PD did not occur in the CF_3I/CO_2 at the voltages found in the tests.

After the PDIV tests with the reduced scaled GIL, a plane-plane geometry was tried in order to verify if the PD problem could be inside the polypropylene insulators of the coaxial geometry. The plane-plane test results show PDIV still around the same range of voltage found in the previous tests. Thus, changing the geometry, the problem was not solved and this means that the insulators of the coaxial geometry were not the PD source.
Considering that PD activity starts at the same range of voltage and that they have a repetitive pattern, some hypothesis are:

1. RUST PARTICLES → since the inner surface of the pressure vessel is covered by a rust layer, when the pressure vessel is filled with CF_3I/CO_2 mixture, it may be that some micro-particles of rust start to float. These particles, under a certain AC voltage value, could start to move under the effect of the electric field from an electrode to the other one. Finally, when a charged particle reaches the opposite electrode a micro-discharge can happen between them and hence, it creates a partial discharge. This can be happened inside the vessel when the voltage applied reached the value found in the tests.

2. EXTERNAL PD SOURCE → if in the high voltage circuit there are elements or devices in which PD occur when the voltage is higher than a certain value, the test results can be compromised. Thus, it is possible that one of the elements used in the HV circuit was the source of PD and that, during the PDIV tests, these current pulses were detected.

8.2.1 Future works

In conclusion, in order to carry out future investigations on the PDIV of CF_3I/CO_2 mixture using a coaxial geometry it is necessary to:

1. test the reduced scale GIL geometry in the new stainless steel pressure vessel which will be available in the Cardiff University laboratory in the next few months. This will allow to avoid floating micro-particles of rust that can affect such delicate measurements.

2. investigate the probable external PD source in the high voltage circuit. In this way clean measurements will be possible to get and thus, a clear PD characterisation of the CF_3I/CO_2 mixture.

Bibliography

[1] Ahmad, Z. (2012). Polymer dielectric materials. In *Dielectric material*. IntechOpen.

[2] Batalovic, M., Sokolija, K., Hadzialic, M., and Batalovic, N. (2016). Partial discharges and iec standards 60840 and 62067: simulation support to encourage changes/parcijalna praznjenja i iec standardi 60840 i 62067: simulacijska podrska za poticanje promjena. *Tehnicki Vjesnik-Technical Gazette*, 23(2):589–599.

[3] Benato, R. (2017). Gas insulated lines slides. Sistemi elettrici per l'energia, Università di Padova.

[4] Benato, R., Di Mario, C., and Koch, H. (2007). High-capability applications of long gas-insulated lines in structures. *IEEE transactions on power delivery*, 22(1):619–626.

[5] BS EN 60270 (2001). High-voltage test techniques - Partial discharge measurements. Technical report, British Standard Istitutions.

[6] Černák, M., Hosokawa, T., Kobayashi, S., and Kaneda, T. (1998). Streamer mechanism for negative corona current pulses. *Journal of applied physics*, 83(11):5678–5690.

[7] Change, C. (2013). The physical science basis. intergovernmental panel on climate change.

[8] Change, I. P. O. C. (2007). Climate change 2007: The physical science basis. *Agenda*, 6(07):333.

[9] Chen, L. (2015). *Investigation on the feasibility of trifluoroiodomethane (CF3I) for application in gas-insulated lines*. PhD thesis, Cardiff University.

[10] Chen, L., Widger, P., Kamarudin, M. S., Griffiths, H., and Haddad, A. (2017). Cf3i gas mixtures: breakdown characteristics and potential for electrical insulation. *IEEE Transactions on power delivery*, 32(2):1089–1097.

[11] Comsol, A. (2018). Comsol multiphysics version 5.3, introduction to comsol multiphysics.

[12] De Urquijo, J., Juárez, A., Basurto, E., and Hernández-Ávila, J. (2007). Electron impact ionization and attachment, drift velocities and longitudinal diffusion in cf3i and cf3i–n2 mixtures. *Journal of Physics D: Applied Physics*, 40(7):2205.

[13] Emel, Ö. (2004). Breakdown characteristics of gases in non-uniform fields. *IU-Journal of Electrical & Electronics Engineering*, 4(2):1177–1182.

[14] Gas enciclopedia by air liquid (2019). Trifluoroiodomethane. `https://encyclopedia.airliquide.com/trifluoroiodomethane`, [Online; accessed February 14, 2019].

[15] Ghaffarian Niasar, M. (2012). *Partial discharge signatures of defects in insulation systems consisting of oil and oil-impregnated paper*. PhD thesis, KTH Royal Institute of Technology.

[16] Gillespie, L. J. (1930). The gibbs-dalton law of partial pressures. *Physical Review*, 36(1):121.

[17] Haddad, A. and Warne, D. (2004). *Advances in high voltage engineering*, volume 40. IET.

[18] Hasegawa, H., Date, H., Shimozuma, M., and Itoh, H. (2009). Properties of electron swarms in cf 3 i. *Applied Physics Letters*, 95(10):101504.

[19] IEC/BS EN 60060-1 (2010). High-voltage test techniques - Part 1: General definitions and test requirements. Technical report, British Standard Istitutions.

[20] Jacob, D. (1999). *Introduction to atmospheric chemistry*. Princeton University Press.

[21] Jamil, M. K. M., Ohtsuka, S., Hikita, M., Saitoh, H., and Sakaki, M. (2011). Gas by-products of cf3i under ac partial discharge. *Journal of Electrostatics*, 69(6):611–617.

[22] Kamarol, M. (2008). Partial discharge properties and gas decomposition analysis of environmental friendly gas insulation media as a basis of diagnostic technique development. *Kyushu Institute of Technology*.

[23] Kamarudin, M. (2013). *Experimental investigation of CF3I-CO2 gas mixtures on the breakdown characteristics in uniform and nonuniform field configurations*. PhD thesis, Cardiff University.

[24] Kamarudin, M., Radzi, N., Ponniran, A., and Abd-Rahman, R. (2016). Simulation of electric field properties for air breakdown using comsol multiphysics. In *4th IET Clean Energy and Technology Conference (CEAT 2016)*, pages 1–5. IET.

[25] Kasuya, H., Kawamura, Y., Mizoguchi, H., Nakamura, Y., Yanabu, S., and Nagasaki, N. (2010a). Interruption capability and decomposed gas density of cf 3 i as a substitute for sf 6 gas. *IEEE Transactions on Dielectrics and Electrical Insulation*, 17(4):1196–1203.

[26] Kasuya, H., Kawamura, Y., Mizoguchi, H., Nakamura, Y., Yanabu, S., and Nagasaki, N. (2010b). Interruption capability and decomposed gas density of cf 3 i as a substitute for sf 6 gas. *IEEE Transactions on Dielectrics and Electrical Insulation*, 17(4):1196–1203.

[27] Katagiri, H., Kasuya, H., Mizoguchi, H., and Yanabu, S. (2008). Investigation of the performance of cf 3 i gas as a possible substitute for sf 6. *IEEE Transactions on Dielectrics and Electrical Insulation*, 15(5):1424–1429.

[28] Kimura, M. and Nakamura, Y. (2010). Electron swarm parameters in cf3i and a set of electron collision cross sections for the cf3i molecule. *Journal of Physics D: Applied Physics*, 43(14):145202.

[29] Koch, H. (2012). *Gas insulated transmission lines (GIL)*. IEEE Press, Chichester, West Sussex, United Kingdom ; [Piscataway, NJ].

[30] Koch, H., Benato, R., Laußegger, M., Köhler, M., Leung, K., Mirebeau, P., Kindersberger, J., Kunze, D., Di Mario, C., Renaud, F., et al. (2008).

Application of long high capacity gas-insulated lines in structures. *CIGRE Technical Brochure*, (351).

[31] Kuffel, J. and Kuffel, P. (2000). *High voltage engineering fundamentals*. Elsevier.

[32] Lauzon, D. and Koch, H. (2006). Sulfur hexafluoride sf 6. In *Power Engineering Society General Meeting, 2006. IEEE*, pages 1–3. IEEE.

[33] Piputvat, V., Rochanapithyakorn, W., Hillers, T., Koch, H., Pöhler, S., and Schoeffner, G. (2004). 550kv gas-insulated transmission line for high power rating in thailand. *B1-107, CIGRE Session*.

[34] Rabie, M. (2017). *A systematic approach to identify and quantify gases for electrical insulation*. PhD thesis, ETH Zurich.

[35] Rabie, M. and Franck, C. M. (2018). Assessment of eco-friendly gases for electrical insulation to replace the most potent industrial greenhouse gas sf6. *Environmental science & technology*, 52(2):369–380.

[36] Rycroft, M. (2015). Gas-insulated transmission lines: the next generation of power transmission.

[37] Solomon, S., Mills, M., Heidt, L., Pollock, W., and Tuck, A. (1992). On the evaluation of ozone depletion potentials. *Journal of Geophysical Research: Atmospheres*, 97(D1):825–842.

[38] Takeda, T., Matsuoka, S., Kumada, A., and Hidaka, K. (2007). "by-products of cf3i produced by spark discharge. *10th Japan-Korea Joint Symposium on Electrical Discharge and High Voltage Engineering*, pages 157–160.

[39] WG, C. et al. (2010). *Cable systems in multi-purpose or shared structures*. .

[40] Widger, P. (2014). *Investigation into CF3I-CO2 gas mixtures for insulation of gas-insulated distribution equipment*. PhD thesis, Cardiff University.

[41] Widger, P., Haddad, A., and Griffiths, H. (2016). Breakdown performance of vacuum circuit breakers using alternative cf 3 i-co 2 insulation

gas mixture. *IEEE Transactions on Dielectrics and Electrical Insulation*, 23(1):14–21.

[42] Xiao, S., Zhang, X., Tang, J., and Liu, S. (2018). A review on sf6 substitute gases and research status of cf3i gases. *Energy Reports*, 4:486–496.

[43] Yun-Kun, D. and Deng-Ming, X. (2013). The effective ionization coefficients and electron drift velocities in gas mixtures of cf3i with n2 and co2 obtained from boltzmann equation analysis. *Chinese Physics B*, 22(3):035101.

[44] Zeng, F., Tang, J., Zhang, X., Zhou, S., and Pan, C. (2018). Typical internal defects of gas-insulated switchgear and partial discharge characteristics. In *Simulation and Modelling of Electrical Insulation Weaknesses in Electrical Equipment*. IntechOpen.

[45] Zhang, X., Tian, S., Xiao, S., Li, Y., Deng, Z., and Tang, J. (2017). Experimental studies on the power–frequency breakdown voltage of cf3i/n2/co2 gas mixture. *Journal of Applied Physics*, 121(10):103303.

[46] Zhang, X., Xiao, S., Han, Y., and Dai, Q. (2015). Analysis of the feasibility of cf 3 i/co 2 used in c-gis by partial discharge inception voltages in positive half cycle and breakdown voltages. *IEEE Transactions on Dielectrics and Electrical Insulation*, 22(6):3234–3243.

[47] Zhang, X., Xiao, S., Zhou, J., and Tang, J. (2014). Experimental analysis of the feasibility of cf 3 i/co 2 substituting sf 6 as insulation medium using needle-plate electrodes. *IEEE Transactions on Dielectrics and Electrical Insulation*, 21(4):1895–1900.